Chair of Ferrous Metallurgy

# Doctoral Thesis

# Structural Improvement of Cast Ingots for Highly Alloyed Steel Grades

## Dipl.-Ing. Kerstin Baumgartner, BSc

March 2020

# AFFIDAVIT

I declare on oath that I wrote this thesis independently, did not use other than the specified sources and aids, and did not otherwise use any unauthorized aids.

I declare that I have read, understood, and complied with the guidelines of the senate of the Montanuniversität Leoben for "Good Scientific Practice".

Furthermore, I declare that the electronic and printed version of the submitted thesis are identical, both, formally and with regard to content.

Date  25.02.2020

Signature Author
Kerstin, Baumgartner

# Kurzfassung

voestalpine Böhler Edelstahl ist ein Hersteller von hochlegierten Stählen, neben korrosionsbeständigen Stählen finden sich auch viele Werkzeugstähle im Portfolio. Das Vergießen in großen Gussblöcken ist nach wie vor das Mittel der Wahl für solche Spezialstähle. Um die Erstarrung solcher Blöcke positiv zu beeinflussen, kann es sinnvoll sein die Erstarrung einerseits früher in eine ungerichtete Form zu leiten und andererseits die Primärkorngröße zu optimieren. Dadurch können Seigerungen, Porositäten oder Lunker reduziert werden.

Die vorliegende Arbeit beschäftigt sich mit der Erstarrung des korrosionsbeständigen super-austenitischen Stahls X1CrNiMoCuN20-18-7 und des Schnellarbeitsstahl HS2-9-1-8. Während beim korrosionsbeständigen Stahl der Fokus auf der Verbesserung der Gussstruktur von gerichtet zu ungerichtet und feinkörnig liegt, steht beim Schnellarbeitsstahl eine Feinung der eutektischen Karbidstruktur im Vordergrund.

Das Literaturstudium beleuchtet die notwendigen Grundlagen, um die chemisch-physikalischen Vorgänge, die sich hinter Erstarrungsstrukturen verbergen, richtig zu bewerten. Außerdem werden die Möglichkeiten, endogene Partikel als heterogene Keimstellen heranzuziehen, im Detail diskutiert. Der Einsatz solcher Einschlüsse als Kristallisationskeime für die Primärstruktur stellt den Fokus dieser Arbeit dar. Besonders $AlCeO_3$ ist ein vielversprechendes Partikel für die Kornfeinung von Austeniten. Einfluss auf die eutektischen Karbide haben vordergründig die jeweilige chemische Zusammensetzung der Stahlsorte und die Erstarrungsbedingungen.

Um die $AlCeO_3$ Bildung vorhersagen zu können, wurde die Verlässlichkeit der in FactSage inkludierten thermodynamischen Datenbank FToxid mit Kleinstexperimenten überprüft und bestätigt. Die Simulation stellt ein nützliches Hilfsmittel zur Vorhersage vielversprechender Einschlusslandschaften dar. Kornfeinungsexperimente mit dem superautenitschen Stahl zeigten, dass bei Summensauerstoffgehalten von 140 ppm und 40 $AlCeO_3$ Partikel pro mm$^2$ die ungerichtete Erstarrung von 23 auf 64 % des Blockquerschnittes und die Anzahl der Körner von 1.7 auf 41 pro cm$^2$ gesteigert werden kann. Umform- und Rekristallisationsexperimente ergaben, dass der Vorteil des gefeinten Gusszustandes auch danach erhalten werden kann, da sich ein langsameres Kornwachstum des gefeinten Materials im Vergleich zu industriell hergestellten ergab.

Am Schnellarbeitsstahl wurde sowohl die Auswirkung von Kornfeinung auf die eutekische Karbidstruktur, als auch jene von unterschiedlichen Erstarrungs- und Gießbedingungen untersucht. Die durch den Einsatz von Titan erreichte Verbesserung der Primärstruktur führte zu keiner Veränderung am Anteil der groben Karbide. Die Erstarrungs- und Gießbedingungen zeigten hingegen eine deutliche Auswirkung auf die eutektische Karbidstruktur. Sowohl größere Kühlraten, als auch niedrige Gießtemperaturen sind vorteilhaft, um den Anteil der groben Karbide zu verkleinern. Der Gesamtkarbidgehalt bleibt dabei unbeeinflusst.

# Abstract

voestalpine Böhler special steel is a manufacturer of highly alloyed steel grades, besides corrosion-resistant steels also many tool steels are available in their portfolio. The casting of large ingots is still state of the art for special steels. The solidification of such steel grades can be improved by promoting an earlier columnar to equiaxed transition and a fine primary grain structure. Segregation, porosities, and shrinkage are able to be minimized through such measures.

This thesis examines the solidification of the corrosion resistant super-austenitic steel X1CrNiMoCuN20-18-7 and the high-speed steel HS2-9-1-8. The change from columnar to equiaxed and fine-grained solidification is the main objective for the super-austenitic steel, while for the high-speed steel the refinement of the eutectic carbide structure is most important.

The literature review engages in the necessary basics to discuss the physicochemical processes during solidification. In addition, the possibilities to apply endogenous particles as heterogeneous nucleation sites are described in detail. To utilize such inclusions as the nucleus for the primary grain structure is the main objective of this thesis. Especially $AlCeO_3$ is a very promising agent for grain refinement of austenitic steels. The most considerable influence on the eutectic carbides is exerted by the chemical composition of the particular high-speed steel grade and the cooling conditions.

For the simulation of the $AlCeO_3$ formation, the reliability of the database FToxid, which is included in FactSage, is tried and approved. The calculation represents a useful tool to forecast the inclusion population. Grain refinement experiments with the super-austenitic steel show that at a total oxygen content of 140 ppm and with 40 $AlCeO_3$ particles per $mm^2$, the ratio of equiaxed solidification is increased from 23 to 64 %. Additionally, the number of grains rises from 1.7 to 41 per $cm^2$. Deformation and recrystallization tests result in slower grain growth of the refined steel in comparison to industrial material. This means that the advantage of the fine cast structure prevails even after the experiment.

The influence of grain refinement and solidification and casting conditions on the eutectic carbide structure is investigated for the high-speed steel. The application of titanium leads to an improvement of the primary structure, but the ratio of coarse carbides is not altered. The casting and solidification conditions showed a distinct impact on the eutectic carbide structure. High cooling rates and low superheating temperatures pose an advantage to decrease the ratio of coarse carbides. The total carbide content stays unaffected.

# Acknowledgment

Firstly, I would like to thank voestalpine Böhler Edelstahl GmbH & Co KG for providing me with this fascinating topic.

My sincere gratitude goes to my advisor, Ao. Univ.-Prof. DI Dr. Christian Bernhard for guiding and challenging me in the course of this thesis.

Besides my advisor, I would like to thank Dr. Martin Hafok for being a reliable partner and supporter of this thesis at Böhler Edelstahl.

I thank all my colleagues for providing me with metallurgical insights, encouraging words and invaluable friendships.

Special thanks go to my parents for your unshakeable beliefs in my capabilities through all these years of education.

Last but not least I would like to thank you, Stefan, for being the best partner and I love you!

# Contents

# Nomenclature

| | |
|---|---|
| a | lattice constant |
| $A_{Eq}$ | average area of equiaxed solidification |
| $A_{Gr}$ | average area per grain |
| $\alpha$, $\delta$ | ferrite |
| AOD | argon oxygen decarburization |
| approx. | approximately |
| $A_{sl}$ | surface of particles per mole |
| at.-% | atomic-percent |
| c | concentration, composition |
| CET | columnar to equiaxed transition |
| CT | casting temperature |
| d | interatomic spacing |
| $d_A$ | mean equivalent area diameter |
| $\delta$ | lattice disregistry |
| $\delta_C$ | diffusion boundary layer |
| $D_L$ | diffusivity |
| E2EM | edge-to-edge matching model |
| EAF | electric arc furnace |
| EBSD | electron backscatter diffraction |
| EDS | energy dispersive spectroscopy |
| $f_d$ | interplanar spacing misfit |
| $f_r$ | interatomic spacing misfit |
| $\Delta G$, $\Delta g$ | Gibbs free energy |
| $\Delta G_0$ | activation energy for nucleation |
| $\Delta G_{het}$ | activation energy for heterogeneous nucleation |
| G | temperature gradient |
| $\gamma$ | austenite |
| $\gamma_{sl}$ | solid/liquid interfacial free energy |
| HSS | high-speed steel |
| ICP-OES | inductively coupled plasma optical emission spectrometry |
| IF | induction furnace |
| k | distribution coefficient |
| $\lambda_1$, $\lambda_2$ | primary/secondary arm spacing |

| | |
|---|---|
| $l_m$ | mean intercept length |
| M(C,N) | Metal-Carbonitride |
| MC, M2C, M6C | Metal-Carbide |
| $N_0$ | total number of heterogeneous nucleation sites |
| $N_{Gr}$ | number of grains |
| NMI | non-metallic inclusion |
| N° | number |
| $\dot{N}$ | nucleation rate |
| OPS | oxide polishing suspension |
| OR | orientation relationship |
| P2PM | plane-to-plane matching model |
| ppm | parts per million |
| r | radius |
| R | universal gas constant |
| $r_0$ | critical radius |
| REM | rare earth metals |
| $R_{Eq}$ | ratio of equiaxed solidification |
| $\Delta s_f$ | entropy of fusion |
| SASS | super-austenitic stainless steel |
| SEM | scanning electron microscope |
| $\Delta T$ | super/undercooling |
| T | temperature |
| $\dot{T}$ | cooling rate |
| $t_f$ | local solidification time |
| θ | wetting angle, angle general |
| $T_L$ | liquidus temperature |
| TO | Tammann-type furnace (vertical tube furnace) |
| $T_S$ | solidus temperature |
| UTS | ultimate tensile strength |
| vBEG | voestalpine Böhler Edelstahl GmbH & Co KG |
| $v_{crit}$ | critical growth velocity |
| $v_s$ | volume of particles per mole |
| wt.-% | weight-percent |
| YS | yield strength |

# 1  Introduction

This thesis is performed in cooperation with voestalpine Böhler Edelstahl GmbH & Co KG (vBEG), a steel producer specialized in the production of highly alloyed special steel grades. Typically for such a plant, the process route implements an EAF for the melting operations, secondary metallurgical equipment like an AOD converter and ingot casting [1,2]. This casting process holds veritable challenges for the solidification of steel, e.g. severe segregation in macro and micro scale, porosities through shrinkage, long solidification times, and insufficient feeding [3]. Some of these challenges could be overcome by promoting an early columnar to equiaxed (CET) transition and a higher number of equiaxed primary grains in the ingot center.

This thesis aims to investigate the possibility of grain refinement through inoculation for super-austenitic stainless steel (SASS) as well as for high-speed steel (HSS), whereas for the HSS the influence on the microstructure is of equal importance as the development of the macrostructure. The solidification of these two special steel grades will be discussed.

First of them is the SASS X1CrNiMoCuN20-18-7 (=Böhler A965), which typically has a solidification structure that is mostly columnar with only a small center of equiaxed solidification. Here the main objective is to investigate chemical inoculation methods that lead to an enlarged equiaxed zone and additionally also to a small primary grain size. Based on the results of a previous master thesis [4] and the promising findings published by various authors [5–8] the main focus is the inoculation with cerium-containing inclusions. At the moment, the application of cerium holds the challenge of blind spots in the thermodynamic data for the inclusion formation. Small scale experiments are performed to study if thermodynamic modeling with FactSage can be applied to help forecast if the particle population can act as an inoculant. For the evaluation of the nucleation potential on the ingot structure, a series of medium-scale tests are conducted. Ingots with a mass of 12 kg are cast, and afterwards, their macrostructure and inclusion population are investigated.

The second examined steel grade is the HSS HS2-9-1-8 (=Böhler S500). The solidification of high-speed steel holds special features of its own. This can be attributed to their alloying levels. Basically, it is a hypo-eutectic system, which precipitates an eutectic consisting of austenite and different types of carbides [9]. The carbides make up 12 vol.-% of these materials and are mainly responsible for the abrasion resistance and hardness and are liable for HSS to be applied as cutting tools [10,11]. The main objective is to refine these primary carbides. Smaller carbides are beneficial for tool life due to harder crack propagation. They lead to improved ductility, hardness, and toughness. Also, the necessary hot deformation to homogenize the material can be reduced, and the manufacturing of tools is simplified [11–14]. For a better understanding of the carbide formation, small scale tests with constant cooling rates and thermodynamic calculations are

performed. The influence of casting temperature and inoculation on the macrostructure and the carbide morphology in 12 kg ingots, are investigated.

The following literature review shall give an overview of solidification, primarily focusing on the processes that are the basis for the experimental part. Additionally, it contains a chapter about the resent knowledge on grain refinement due to the promotion of heterogeneous nucleation.

# 2  Basics of Solidification

This is the first part of the literature review. It gives an introduction to the processes during solidification and on the formation of solidification structures. These basics are needed to argue the experimental part of this thesis. This review does not claim completeness on the very complex topic of solidification, for a broader overview, books like "Fundamentals of solidification" by W. Kurz and D.J. Fisher [15] or "Solidification" by J.A. Dantzig and M. Rappaz [3] are recommended. Discussed are the basics of nucleation, dendritic growth, macrostructures of large ingots, and the special features of solidification of SASS and HSS.

## 2.1  The Concept of Nucleation

The formation of clusters of atoms with a crystalline structure always marks the start of solidification. They form due to random thermal fluctuation. Clusters that are too small to survive in the melt are called embryos, when they are large enough to be stable and grow, they are named nuclei. The classical theory of homogeneous nucleation assumes a spontaneous formation of these nuclei in a melt without any impurities. But this approach leads to nucleation rates much different from those observed in reality. Thus the concept of heterogeneous nucleation is proposed. Here the cluster formation is promoted on impurities like nonmetallic inclusions (NMI) or interfaces like the mold surface [3].

**Homogeneous Nucleation**

At a given temperature, the state with the smallest Gibbs free energy is stable. If the temperature $T$ is lower than the melting temperature $T_L$ ($T < T_L$), the solid-state is favored. When $T > T_L$ the liquid state holds the minimum free energy. At the melting point, the Gibbs free energy for melt and solid must be the same because the two phases are in equilibrium. From this, it follows, that if the temperature of the melt becomes smaller than $T_L$, the temperature difference provides a driving force for solidification. This process is also referred to as undercooling $\Delta T$ or supercooling of the melt. But undercooling of the melt does not lead to spontaneous solidification, because as mentioned above the nuclei form through random thermal fluctuation. Under the assumption that a nucleus has a spherical form with radius $r$ and that the solid/liquid interfacial free energy is set as $\gamma_{SL}$, the total free energy for the nucleation of 1 mole can be given by equation (1) as the addition of volume free energy and surface free energy. $\Delta g$ is the Gibbs free energy

difference between liquid and solid per volume and depends on the undercooling as well as on $\Delta s_f$, the entropy of fusion per unit volume (equation (2)) [15,16].

$$\Delta G = \Delta g v_s + \gamma_{sl} A_{sl} = \frac{\Delta g 4 \pi r^3}{3} + \gamma_{sl} 4 \pi r^2 \tag{1}$$

$$\Delta g = - \Delta s_f \Delta T \tag{2}$$

If ΔT is negative, every cluster dissolves with the recovery of energy. Only when the melt is undercooled, ΔT is positive, and subsequently, Δg is negative, and equation (1) can become negative, and solidification is thermodynamically possible. But it is visible in **Figure 2-1** that also then the Gibbs free energy is only decreasing if a critical radius $r_0$ is surpassed. The first deviation $\frac{d(\Delta G)}{dr} = 0$ leads to equation (3) for $r_0$. When equation (3) is used in equation (1) the activation energy for nucleation $\Delta G_0$ can be calculated, this leads to equation (4) [15,16].

$$r_0 = \frac{2 \gamma_{sl}}{\Delta g} \tag{3}$$

$$\Delta G_0 = \Delta G(r_0) = \frac{16}{3} \pi \frac{\gamma_{sl}^3}{\Delta g^2} \tag{4}$$
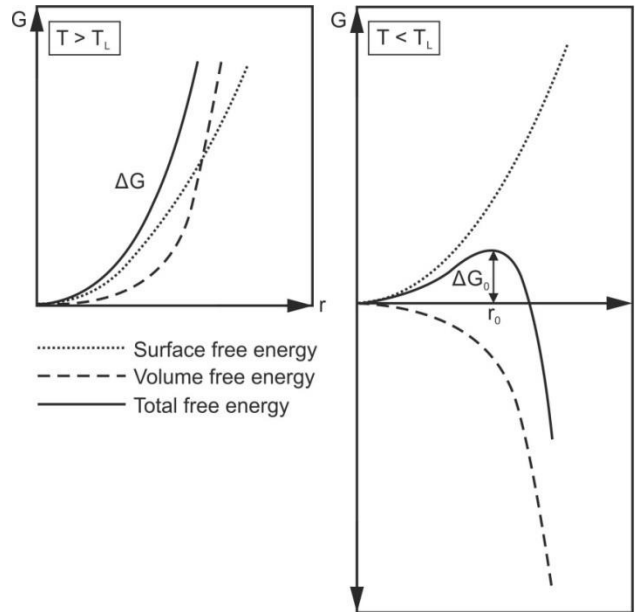


**Figure 2-1:** Gibbs free energy of a spherical nuclei depending on its radius r, adapted from [16]

Because nucleation happens through thermal fluctuations, the rate of nucleus formation can be approximated through equation (5).

$$\dot{N} \sim exp \left( - \frac{\Delta G_0}{RT} \right) \tag{5}$$

Due to $\Delta G_0$ depending on the undercooling of the melt, small changes of ΔT lead to drastic changes of $\dot{N}$. But nucleation rates calculated according to equation (5) are much lower than observed in reality because in real melts nucleation does not start through a thermal fluctuation, but heterogeneously on available free surfaces [16].

**Heterogeneous Nucleation**

Solid particles or a crystalline crucible can facilitate nucleation if the activation energy that is required is decreased. The activation energy for heterogeneous nucleation can be calculated according to equation (6) and (7). Equation (7) is only applicable for a level surface and merely depends on the wetting angle θ between a growing spherical cap and a solid substrate. Because of the exponential relationship between nucleation rate and activation energy, the former can be increased significantly by heterogeneous nucleation [15,16]. The topic of heterogeneous nucleation and the requirements solid particles have to fulfill to act as active nucleation sites are discussed more detailed in section 3.

$$\Delta G_{het} = f \cdot \Delta G_0 \tag{6}$$

$$f = \frac{1}{4}(2 + cos\theta)(1 - cos\theta)^2 \tag{7}$$

## 2.2 Dendritic Growth

Most technical alloys solidify through the formation of dendrites. Ahead of the solidification front, a diffusion layer is present. The varying solubility of alloying elements in the solid- and liquid phase leads to segregation. This can be described with the equilibrium partition coefficient k given in equation (8), where $c_S^*$ and $c_L^*$ are the composition of the solid and liquid at the interface at a certain temperature $T^*$. In binary systems Fe-X, k is usually smaller than 1, this means the alloying elements are rejected into the melt. **Figure 2-2** shows the upper left corner of a typical phase diagram. At $T_S$ the solid has the composition $c_0$, while $c_0/k$ is the composition of the liquid. The lower graph displays the structure over distance (x). Assuming the transport of the rejected solute element by diffusion in the liquid, a diffusion boundary layer $\delta_C$ and a solute pile-up exist. This leads to a local equilibrium liquidus temperature for every point ahead of the solidification front. **Figure 2-2** also shows the case of constitutional undercooling, where the temperature gradient G imposed by the cooling conditions leads to a temperature lower than the equilibrium liquidus temperature [17,18].

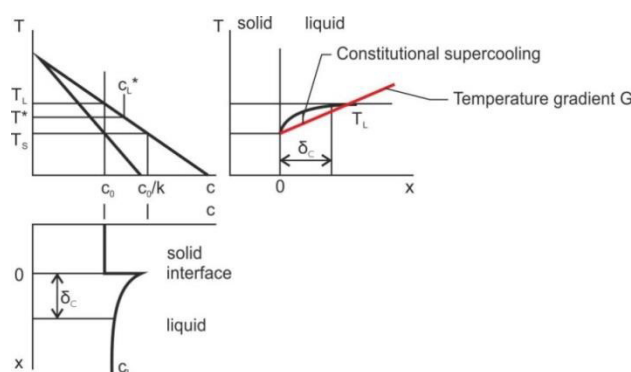$$k = \frac{c_S^*}{c_L^*} \tag{8}$$



**Figure 2-2:** The thermal and solutal field in front of the solid/liquid interface plus constitutional supercooling adapted from [17,18]

When G is assumed to be constant, a critical growth velocity $v_{crit}$ can be defined by equation (9), where $D_L$ is the diffusivity in the liquid and $T_L$ and $T_S$ are liquidus and solidus temperature. As can be seen in **Figure 2-3** beyond $v_{crit}$, no planar solidification front is possible, but cellular or dendritic growth appears [18].
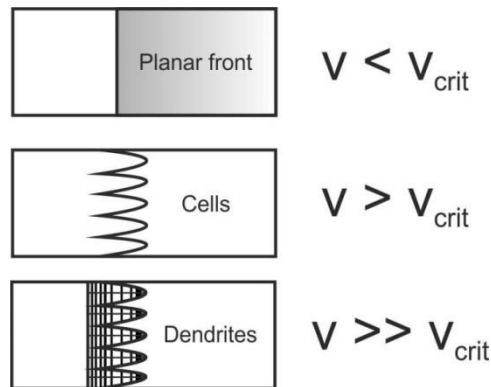
$$v_{crit} = \frac{D_L \cdot G}{T_L - T_S}$$

(9)



**Figure 2-3:** Solid-liquid interface as a function of growth velocity at a constant temperature gradient, adapted from [18]

Constitutional undercooling leads to the formation of an unstable solidification front. For high degrees of constitutional undercooling, the amount of local undercooling increases very fast and the spike-like formations are growing into the melt. They become sharper and can even develop secondary and tertiary arms. These types of structures are known as dendrites [18].

The periodicity in which these spikes occur is called the primary dendrite arm spacing $\lambda_1$. The secondary dendrite arms start as lateral disturbances on the primary arms. The spacing between the secondary arms is denoted as $\lambda_2$. It can be measured between arms that are clearly attached to a primary arm. The secondary dendrite spacing can be detected in columnar and equiaxed grains, while $\lambda_1$ is only visible in columnar areas. For evaluating the fineness of a cast structure in equiaxed zones, the number of grains substitutes $\lambda_1$. The number of grains is controlled by nucleation, while $\lambda_2$ represents the thermal conditions during solidification. Therefore it is possible, to have coarse grains with fine secondary arm spacings. Values for $\lambda_2$ show good correspondence to the local solidification time $t_f$, $t_f$ being the time spent between the liquidus and the solidus temperature. Equation (10) gives a typical power law that connects $\lambda_2$, $t_f$ and cooling rate $\dot{T}$. k is a constant and the exponent n varies from 0.2 to 0.45 [17,18].

$$\lambda_2 = k t_f^n = k \left( \frac{T_L - T_S}{\dot{T}} \right)^n$$

(10)

## 2.3 Cast Structures

Generally, in a standard ingot or casting, it is possible to differentiate between three structural zones. **Figure 2-4** shows the outer equiaxed, the columnar, and the inner equiaxed area. At the mold surface cooling rates are typically at their highest values. This is the reason for the nucleation of a large number of fine equiaxed grains. Shortly afterwards, the grains become dendritic, and those arms growing along preferred crystallographic directions can eliminate the dendrite arms that do not follow a favorable direction. This leads to the formation of the columnar zone. Often but not always an inner equiaxed zone can be observed as well. This area is the result of detached dendrite arms being able to grow in the slightly-undercooled melt. While columnar grains always grow against the direction of heat flow as a result of the heat being removed into the mold, the equiaxed grains grow in the direction of heat flow, because the heat flows to the undercooled melt. So the equiaxed crystal is the hottest part during equiaxed solidification. Therefore the melt has to be colder than the liquidus temperature to allow equiaxed growth [15]. The length of the columnar zone depends on numerous factors. Some examples are the difference between solidus and liquidus temperature, the degree of superheating, and the cooling efficiency. Higher superheating leads to a larger ratio of columnar solidification [18]. Under the assumption that equiaxed grains are formed by heterogeneous nucleation and do not move, a criterion (Equation (11)) proposed by Hunt can be applied to define the critical temperature gradient that leads to fully equiaxed growth. It is further assumed that if the volume fraction of equiaxed grains ahead of the columnar solidification front is large enough, the columnar solidification can be stopped [3,17,19].

$$G < 0.617 \cdot N_0^{1/3} \left(1 - \frac{\Delta T_N^3}{\Delta T_c^3}\right) \cdot \Delta T_c \qquad (11)$$

Where G is the temperature gradient, $N_0$ the total number of heterogeneous nucleation sites per unit volume, $\Delta T_N$ the undercooling at the heterogeneous nucleation temperature and $\Delta T_c$ the undercooling at the columnar front [19].

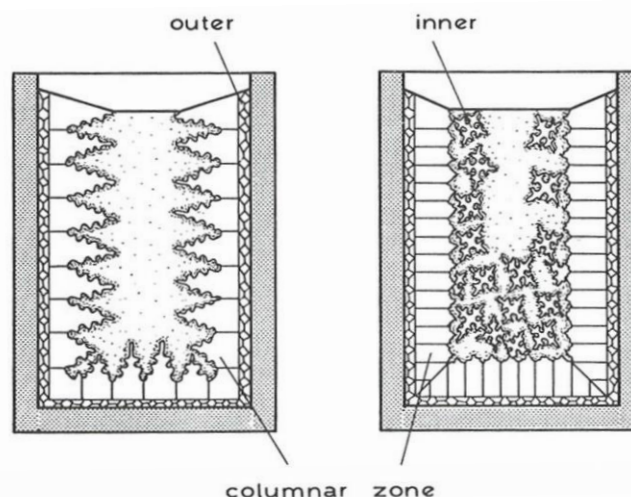For more information on the solidification of large ingots, please refer to Chapter 15-3 in [18].



**Figure 2-4:** Structural zones in castings [15]

## 2.4 Foundations for Special Steel Grades

The steel grades worked with throughout this thesis are both special steels. The first falls in the category of stainless steels, and the second belongs to the group of tool steels. Both are heavily alloyed but completely different materials. The chemical analysis is available in **Table 2-1**. This section shall give an overview of the special features of both steel grades.

**Table 2-1:** Chemical analysis of investigated steel grades in wt.-%

| Trade-mark | Standard designation | Name in thesis | C | Si | Mn | S | Cr | Mo | Ni | Cu | N |
|---|---|---|---|---|---|---|---|---|---|---|---|
| Böhler A965 | X1CrNiMoCuN 20-18-7 | SASS | 0.015 | 0.2 | 0.6 | 0.0004 | 19.8 | 6.3 | 18.1 | 0.65 | 0.193 |
| | | | C | Si | Mn | S | Cr | Mo | V | W | Co |
| Böhler S500 | HS2-9-1-8 | HSS | 1.1 | 0.5 | 0.2 | <0.0003 | 3.7 | 9.2 | 1.0 | 1.4 | 7.8 |

**Super Austenitic Stainless Steels**

All stainless steels are united by their exceptional corrosion resistance. The deciding factor for the resistance against corrosion is the chromium content. A minimum of 10.5 wt.-% has to be included to ensure it. Cr forms a passivation layer on the surface due to its high affinity towards oxygen [20].

Within the group of stainless steels, the austenitic stainless steels are the largest group. Due to the high contents of Cr and Ni, they are very costly, but they show better behavior considering formability and weldability. The alloying materials of super austenitic stainless steels are even more expensive, as they additionally contain Mo and N. This leads to better resistance against stress corrosion cracking and pitting corrosion [21].

As can be seen in **Figure 2-5** fully austenitic steels like the X1CrNiMoCuN20-18-7 show no phase transformation at all, thus, the primary grain size is even more important for the final grain size [6]. Smaller grains are the only parameter that can improve tensile strength and ductility at the same time. Therefore the optimization in the as-cast state is very interesting for SASS [16,22]. For more details regarding grain refinement, please refer to chapter 3.
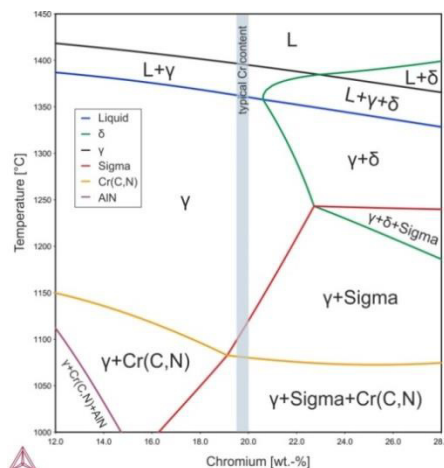


**Figure 2-5:** Phase diagram of SASS calculated with Thermocalc database TCFE8.1

## High-Speed Steels

High-speed steels are highly alloyed tool steels, mostly used for machining applications. In contrast to normal tool steels, they distinguish themselves through outstanding high-temperature strength, tempering resistance up to 600 °C and high hardness at fast cutting speeds. To achieve these properties, the interaction between chemical composition, solidification structure, heat treatment, and hot deformation has to be considered carefully. The typical carbon content ranges from 0.8 to 1.4 wt.-%. Besides C, the most important alloying elements are Cr, W, Mo, V, and Co [9,23]. As discussed above, the first step of solidification is the formation of either δ-ferrite or γ-austenite dendrites [23]. But HSS are hypo-eutectic alloys, this means when the melt reaches the eutectic composition, the dendritic growth is stopped, and the remaining liquid solidifies as an eutectic structure in the interdendritic regions [24]. **Figure 2-6** shows the equilibrium phase diagram for HS2-9-1-8: Solidification starts with the formation of γ, then alloying elements are rejected to the liquid until MC and then also $M_6C$ are precipitating simultaneously with γ as an eutectic. The final microstructure consists of a martensitic matrix and the hard carbides.
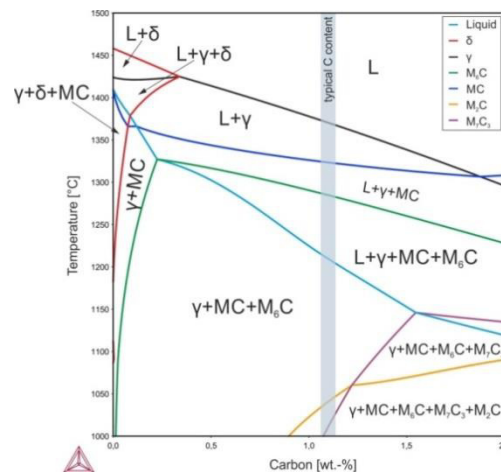


**Figure 2-6:** Equilibrium phase diagram of HS2-9-1-8 calculated with Thermocalc database TCFE8.1 [25]

Thus it is useful to recapitulate the basics of eutectic solidification when discussing HSS. A eutectic reaction is the direct transformation of a liquid into two solid phases. An example of a hypo-eutectic alloy is given in **Figure 2-7**. The dendrite tip is growing ahead into the liquid with a temperature $T < T_L$. At the same time, the interdendritic regions become more and more enriched, and the eutectic starts to grow at an undercooling $\Delta T$ below $T_{eut}$ and a composition near $c_{eut}$. In a hypo-eutectic alloy with a composition $c_0 < c_{eut}$ it is most likely that α is the first eutectic phase to precipitate. While α is growing, the remaining liquid is enriched with B until the melt composition on the liquid-α interface $c_l^{*\alpha}$ becomes larger than $c_{eut}$. **Figure 2-7** shows that the liquid is undercooled $\Delta T^\beta$ in respect to the liquidus temperature for the β-phase for this certain composition. When a critical value of $\Delta T^\beta$ is reached, β-phase precipitates somewhere on the liquid-**α** interface [3].
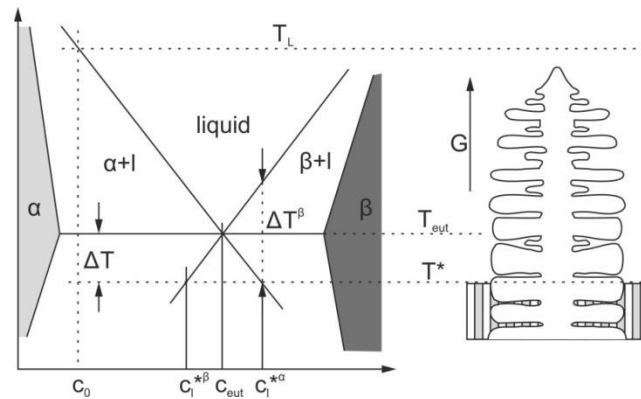
**Figure 2-7:** Typical eutectic phase diagram with associated hypo-eutectic microstructure, adapted from [3]

For HSS the precipitation of complex irregular eutectics is common, they are typical for metal/non-metal eutectics. One of the two phases is faceted and is only able to grow along defined planes and directions. The faceted phase leads the solidification and is surrounded by the non-faceted phase. **Figure 2-8** shows a schematic idealized irregular eutectic growth. When the spacing between two faceted β-lamellae becomes lower than $\lambda_{min}$, one of them is overgrown by the other. On the other hand, if the space between the lamellae gets too wide, the center of the non-faceted phase builds up solute. This leads to a decreasing of the local liquidus temperature, and the interface retracts. When a spacing $\lambda_{br}$ is reached, the driving force for the growth of β into this region is large enough to lead to the branching of the lamellae [3,26].
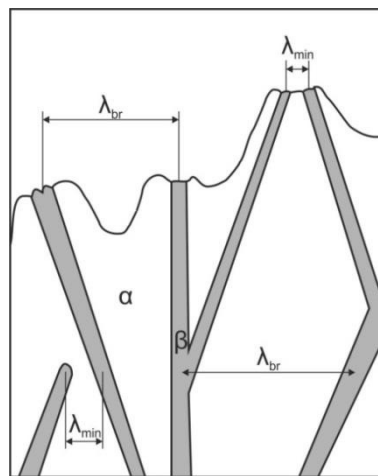


**Figure 2-8:** Schematic idealized irregular eutectic growth, adapted from [26]

Typically the precipitating eutectic in HSS consists of carbides and austenite. The most important ones are MC, $M_2C$, and $M_6C$, not so common are $M_7C_3$ and $M_{23}C_6$. M always represents a mixture of carbide forming elements. The carbides are responsible for the hardness and abrasion resistance of HSS. Which type of carbide forms, depends on the chemical composition of the exact steel grade and also on the cooling conditions during solidification [23]. Typically three groups of high-speed steels can be distinguished regarding their chemical composition: The tungsten-, the molybdenum- and the tungsten/molybdenum-group. **Figure 2-9** shows how the ratio of W/Mo influences the carbide types in the as-cast solidification structure. HS2-9-1-8 and HS2-9-2 are examples for the molybdenum-group and in contradiction to the equilibrium phase-diagram of HS2-9-1-8 shown above the major carbide type in the as-cast state typically is the metastable $M_2C$ instead of the stable $M_6C$. When Mo and W are more evenly distributed, like in HS6-5-2, a

mixture of $M_2C$ and $M_6C$ occurs and the tungsten-grades precipitate mostly $M_6C$ as eutectic carbide. In all of these grades eutectic MC forms as well, but because of its much lower phase content, it is of less importance [27,28].
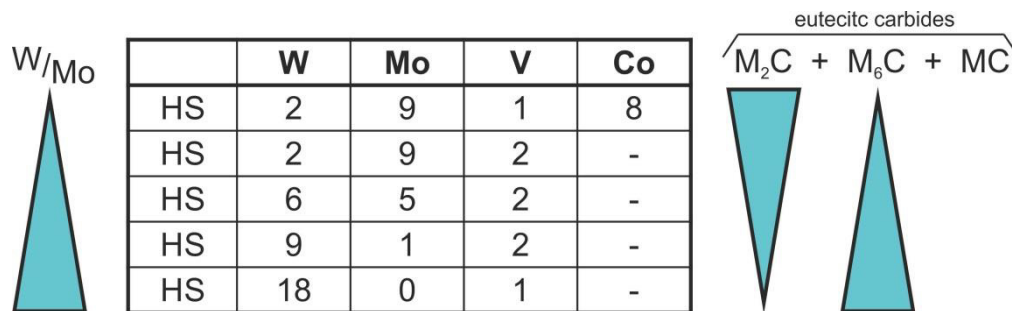


**Figure 2-9:** Effect of W/Mo ratio on the eutectic carbide formation, adapted from [27]

Figure 2-10 pictures how different cooling rates and steel grades influence the eutectic carbide types. High tungsten contents, together with low carbon and vanadium, mostly lead to stable $M_6C$ independent from the cooling conditions. The $M_2C$ formation is favored with increasing carbon and vanadium because the solubility of these elements is higher in the $M_2C$ than in the $M_6C$. Other factors promoting $M_2C$ formation are higher cooling rates and higher Mo contents. When looking at the steel group with 6 wt.-% of W and 5 wt.-% of Mo in **Figure 2-10**, it is interesting to notice that in the absence of vanadium $M_6C$ formation is favored and as soon as vanadium is contained either a mixture of $M_2C$ and $M_6C$ or only $M_2C$ is formed, also depending on the cooling rate [27].
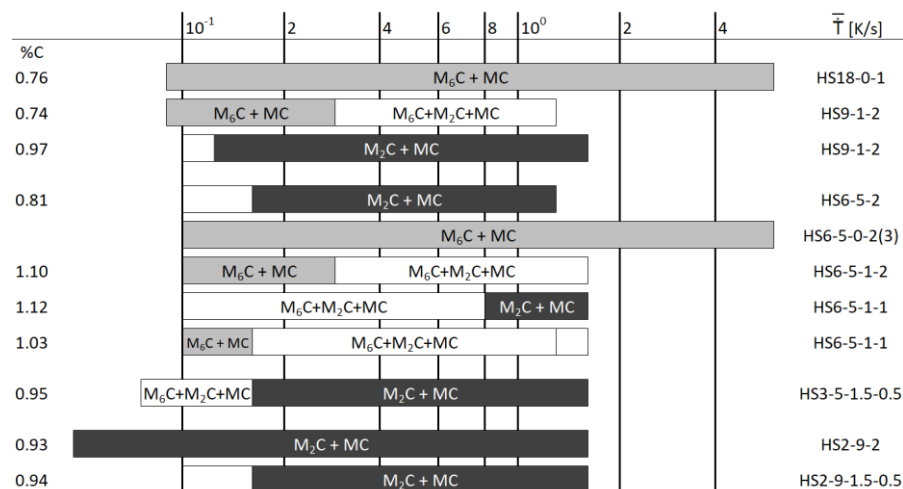


**Figure 2-10:** Effect of cooling rate on the as-cast carbides in different high-speed steels, adapted from [27]

The carbide contents of HSS can amount up to 12 vol.-%. Carbides are responsible for the abrasion resistance and hardness of the material, and without carbides that are precipitated directly from the liquid HSS would not have the necessary properties to be applied as cutting tools [10,11]. Besides the necessary volume content, the carbides must be evenly distributed in the material, favorable are small carbides, because they lead to improved tool live due to harder crack propagation, better ductility, hardness, and toughness. Under conventional manufacturing conditions, this is reached through severe hot deformation and heat treatment. An improvement of the as-cast carbide distribution and size should either reduce these process steps or it should allow larger ingot sizes [11–14].

The following paragraphs give details on the carbide structure and chemical composition of MC, $M_6C$, and $M_2C$.

**MC-carbide**

The most stable of the carbides is the MC, with 3000 HV it is also the hardest. It is known for its face-centered-cubic lattice structure and can be formed with Ti, Nb and V. In the cast structure MC can be detected either in a rough, blocky form if it was precipitated above $T_L$, or in a lamellar eutectic structure [9,29]. **Figure 2-11** shows an example of eutectic MC in a HSS material with 6 wt.-% of V for applications in rolling mills [30]. High-speed steels for cutting tools normally do not exceed a V content of 4 wt.-%, because then the amount of MC carbides is in a range where a failure-free hot deformation becomes impossible [9,29].
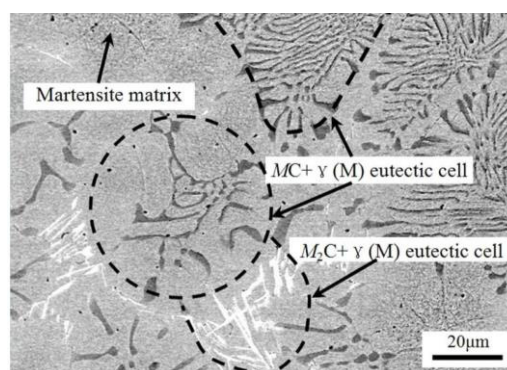


**Figure 2-11:** Eutectic MC in Fe-1.8 wt.-% C-4.2 wt.-% Cr-5.8 wt.-% Mo-6 wt.-% V [30]

**$M_6C$-carbide**

Typical for the solidification of steels with high tungsten content is the formation of $M_6C$ with its complicated face-centered-cubic lattice structure. In the as-cast state, the eutectic carbide is characterized by lamellae periodically starting to grow from a central lamella. This is referred to as a typical fishbone-like structure, which can be seen in **Figure 2-12**. Other elements promoting the $M_6C$ formation are Si, N, and Nb. Typical chemical formulas can be $A_4B_2C$ or $A_3B_3C$, where A=Fe, Cr, Co, Mn, Ni and B=W, Mo, Nb, V [9,29].
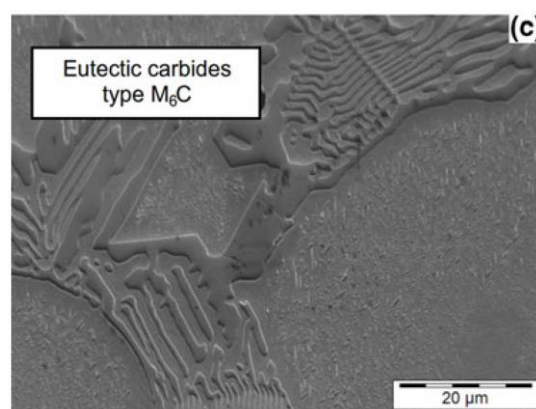


**Figure 2-12:** Typical $M_6C$ in fishbone like shape with central lamella [31]

**$M_2C$-carbide**

$M_2C$ has a hexagonal lattice structure and is typical for steels with a low ratio of W/Mo. Depending on the chemical composition, the appearance of the carbides may differ significantly.

They can be thick and plate-like, lamellar, or rod-shaped (**Figure 2-13**). With higher carbon contents the formation of $M_2C$ gets more likely, this is because the $M_6C$ can only dissolve 14 at.-% C and $M_2C$ up to 33 at.-%. Another element promoting $M_2C$ is vanadium [9,29].

$M_2C$ is thermodynamically unstable and decomposes into fine MC and $M_6C$ during heat treatment, according to equation (12). This is an advantage compared to HSS with only eutectic $M_6C$ because $M_6C$ is only crushed by hot deformation but does not decompose, leading to a larger final size of the carbides. Additionally, the release of carbide forming elements for the secondary carbides is considerably lower [9,29].

$$M_2C + \gamma \leftrightarrow MC + M_6C \qquad (12)$$
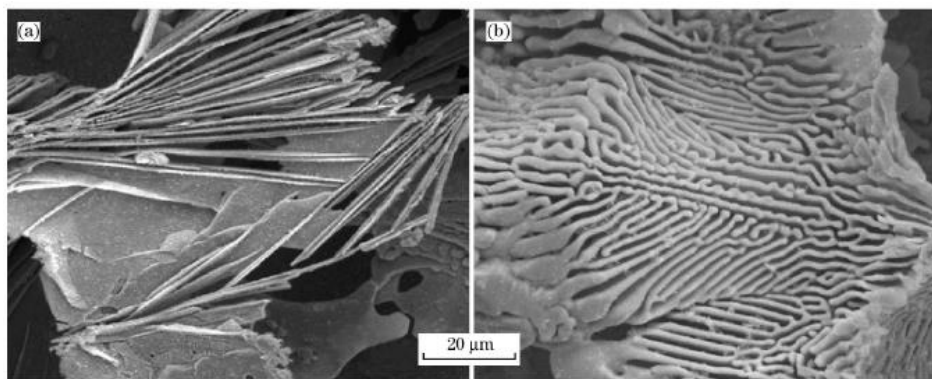


**Figure 2-13:** Three-dimensional morphology of a) plate-like and b) lamellar $M_2C$ carbides [32]

The shape of the $M_2C$ is influenced by the chemical composition and the cooling conditions. Typical for higher tungsten contents is the plate-like morphology. In HS6-5-2, a critical V content of 21 at.-% was found. $M_2C$ carbides with V contents surpassing this threshold exhibit a rough plate-like structure, while $M_2C$ with less V shows a fine, lamellar morphology [9]. Higher cooling rates can transform the plate-like structures into a lamellar or rod-shaped condition [32]. In HS2-9-1-8 an increase of the cooling rate from 3.0 to 16.1 °C/s lead to a morphology change from lamella to curved-rod (**Figure 2-14**). The latter shape possesses advanced properties regarding decomposition during heat treatment [33].
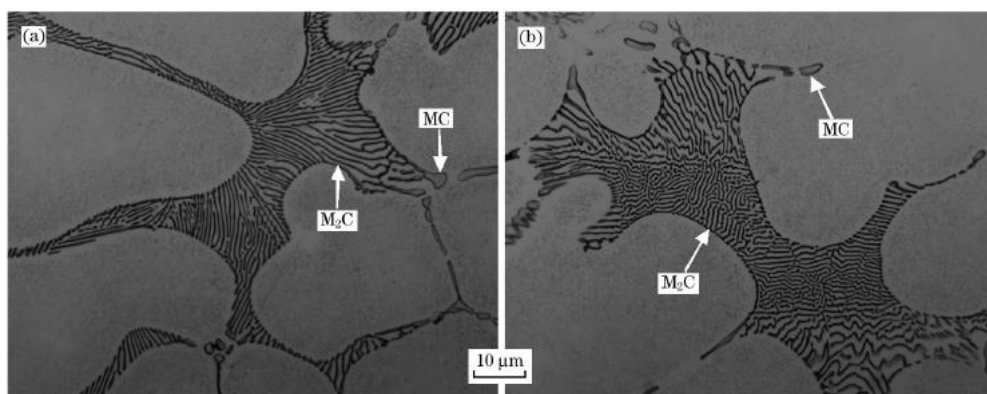


**Figure 2-14:** Typical morphologies of $M_2C$ eutectics formed with different cooling rates, a) lamellar and b) curved-rod [33]

Another example of the influence of the chemical composition of HSS on the $M_2C$ morphology is given in **Figure 2-15**. The base material is HS2-9-2. The aim was to reduce the $M_2C$ stability and

investigate the influence of alloying elements on the carbide structure. Thus the V content was decreased from 1.91 to 1.04 wt.-%, and the Si content was increased from 0.26 to 0.72 wt.-%. This led to a change from plate-like (**Figure 2-15**-left) to lamellar shape (**Figure 2-15**-right) [9].
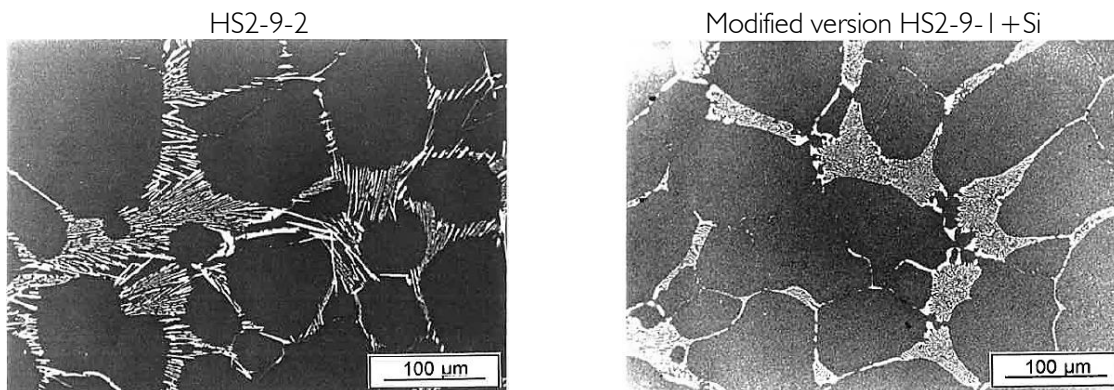
HS2-9-2               Modified version HS2-9-1+Si



**Figure 2-15:** Morphology change of $M_2C$ through the modified chemical composition of HS2-9-2 [9]

Lichtenegger proposed that the finer regions of the $M_2C$ eutectic structure are the first areas to solidify, while towards the end the structures are coarsening. **Figure 2-16** gives an example where the fine lamellar carbide area (top left) changes into coarser shapes (top right and bottom left) towards the end of solidification.
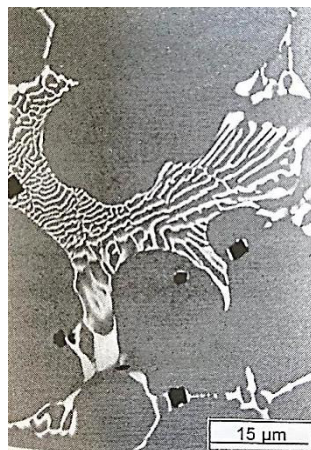


**Figure 2-16:** Coarsening of $M_2C$ carbide at the edge of the eutectic area [9]

From all of the above, it is evident that the standard thermodynamic equilibrium calculation of HS2-9-1-8 does not picture the solidification process under manufacturing conditions well. It would forecast a solidification structure consisting of austenite, M(C, N) and $M_6C$, as shown in the precipitation diagram in **Figure 2-17**. The left part shows the full-scale version, while the right part gives more details on the carbide formation. The red line corresponds to the mass fraction of liquid. Its bend at 1371 °C represents the liquidus temperature, and the solidus temperature is reached at 1210 °C. The precipitation of M(C, N) and $M_6C$ starts at 1324 °C and respectively 1285 °C.
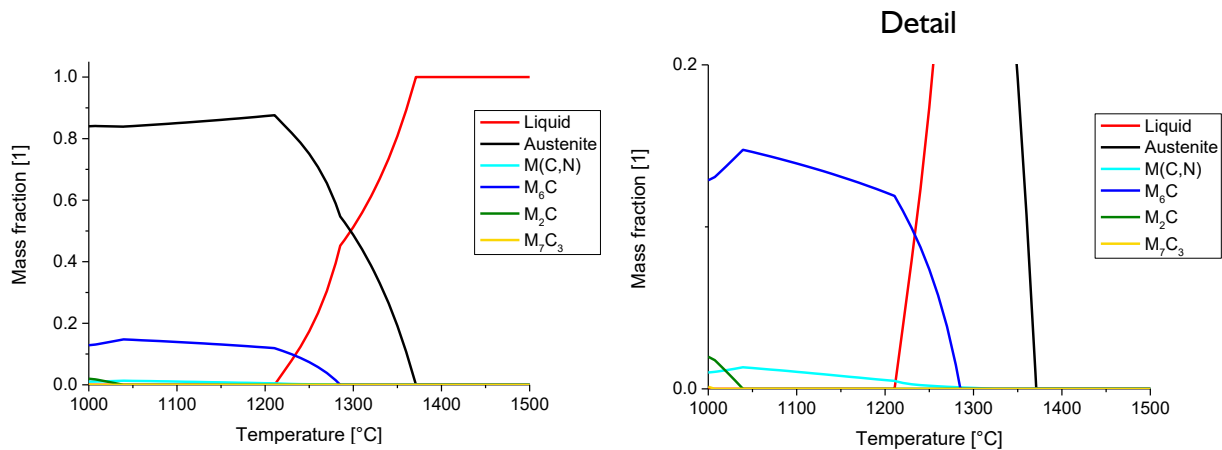
**Figure 2-17:** Equilibrium precipitation diagram of HSS including all carbide phases, calculated with Thermocalc TCFE8.1

But the obtained cooling rates under process conditions favor the formation of the metastable $M_2C$ instead of $M_6C$ for molybdenum-type HSS. Only very low cooling rates lead to the precipitation of $M_6C$ in HS2-9-1-8, as is shown in chapter 6. The only possibility to investigate the formation of $M_2C$ carbides via thermodynamic calculations with Thermocalc is to exclude the $M_6C$ formation. **Figure 2-18** gives the precipitation diagram of such a simulation. The liquidus temperature and M(C,N) precipitation do not change, and solidus drops slightly to 1207 °C. $M_2C$ formation does not happen until 1229 °C, and the simulation also shows that at solidus temperature, the mass fraction of $M_2C$ is 6 % lower than the mass fraction of $M_6C$ in the first calculation. The chemical composition of the $M_2C$ from the simulation and SEM-EDS measurements are compared in **Table 2-2**. SEM-EDS does not allow an accurate analysis of carbon. Thus the carbon content is set to the calculated value, and the remaining elements are normalized to 100 %. The Cr and W contents present the most significant deviations. The calculation result of the chemical composition of the $M_2C$ fits the measurement very accurately.
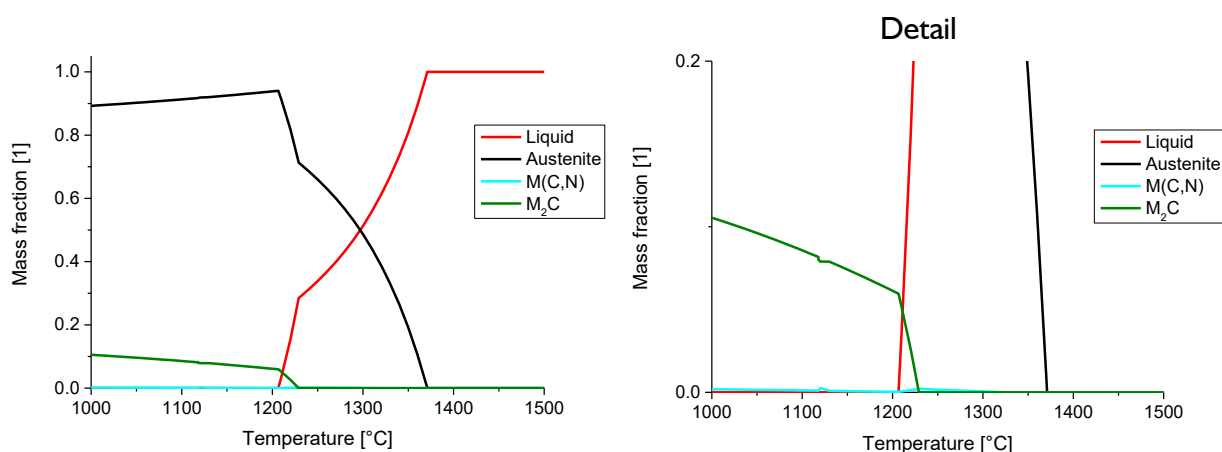


**Figure 2-18:** Equilibrium precipitation diagram of HSS - $M_6C$ excluded, calculated with Thermocalc TCFE8.1

Table 2-2: Comparison of $M_2C$ compositions obtained by SEM-EDS and Thermocalc calculations, normalized to 100 %

|  | Fe | C | Cr | Mo | V | W |
|---|---|---|---|---|---|---|
| $M_2C$ –real | 5.7 | 6.5 | 6.8 | 66.3 | 7.0 | 7.7 |
| $M_2C$ – Thermocalc | 5.4 | 6.5 | 5.9 | 65.7 | 7.7 | 8.7 |

The limitation of this kind of simulation approach is that no predictions about the $M_2C$ stability can be made. Just an example: A minor change of the chemical composition influences the $M_2C$ balance and may favor the $M_6C$ formation. For such a calculation, $M_6C$ must be included as well, because the result should enlighten the influence of the chemical composition on the amount of $M_2C$ vs. $M_6C$. But such a calculation would commonly lead to only $M_6C$ formation and no eutectic $M_2C$ because only with major changes of the chemical composition $M_2C$ would precipitate in the equilibrium calculation at all as long as $M_6C$ is included in the procedure.

Attempts to use the Scheil-solidification module of Thermocalc showed that the program is not able to perform a Scheil-calculation without including $M_6C$ and like in the equilibrium calculation $M_2C$ is not precipitated from the liquid.

## 2.5  Summary

The most important points in this chapter are:

- Solidification takes place when the melt is sufficiently undercooled. In technical solidification processes, impurities and interfaces between mold or crucible and the liquid steel significantly reduce the necessary undercooling and thus accelerate nucleation. This effect is called heterogeneous nucleation.

- In most cases, the as-cast structure has a dendritic morphology. The secondary dendrite arm spacing $\lambda_2$ corresponds to the cooling conditions during solidification and correlates to the local solidification time, as well as to the cooling rate.

- The macrostructure of cast ingots can be divided into three zones, first, the outer equiaxed, second, the columnar and third, the inner equiaxed area. As long as the heat is removed over the mold surface the columnar zone is growing into the melt, only when the liquid gets colder than the melting temperature and heat removal into the liquid is possible, equiaxed grains can form.

- The super austenitic stainless steel X1CrNiMoCuN20-18-7 solidifies as austenite and has no phase transformation during cooling. Additionally, it tends towards completely columnar solidification, and therefore problems like center porosities and segregation could be overcome through the promotion of heterogeneous nucleation.

- High-speed steels are materials with a high amount of eutectic carbides. An optimized solidification process should help to precipitate the eutectic carbides in a preferably small and fine shape. Smaller carbides improve the tool life due to harder crack propagation and also lead to increasing ductility and toughness. The deciding factors in the selection of the eutectic carbide type are summarized in **Table 2-3**. Higher carbon, molybdenum

and vanadium contents, as well as increased cooling rates, favor the $M_2C$ formation, while tungsten, silicon, nitrogen, and niobium promote the precipitation of $M_6C$.

- HS2-9-1-8 belongs to the molybdenum group off high-speed steels. Thus the most crucial eutectic carbide is the metastable $M_2C$. It can be influenced by the chemical composition or the cooling rate. The former is not part of this thesis, because the chemical composition must stay within the specification limits. Therefore the effects of cooling rate and solidification structure on the eutectic carbides are investigated in greater detail.

Table 2-3: Main influencing factors on the formation of carbide eutectics [27]

| Increasing → | C | W/Mo | V | Si | N | Nb | T |
|:---:|:---:|:---:|:---:|:---:|:---:|:---:|:---:|
| $M_2C$ | + | - | +_- | - | - | - | + |
| $M_6C$ | - | + | -_+ | + | + | + | - |

# 3 Grain Refinement

The following second part of the literature review deals with the theoretical background for grain refinement in steels. It includes the motivation for grain refinement, a summary of different theoretical theories on grain refinement mechanisms and an overview for grain refinement approaches in different steel grades, concentrating on the effect of endogenous particles. Due to the numerous applications of thermodynamic modeling in this thesis, the basics for inclusion formation are discussed additionally.

## 3.1  Motivation for Grain Refinement

There exist numerous reasons to prefer a solidification structure which consists of fine primary grains and undergoes an early columnar to equiaxed transition. The most common one is that smaller primary grains lead to a reduction in macrosegregation and an increase of strength and ductility. Other reasons can include the need for more isotropic material properties, the reduction of deformation steps, or the avoidance of porosities [3].

96.3 % of the annual world steel production is manufactured via the continuous casting route. Continuous casting offers various options to influence the ratio of equiaxed solidification: the reduction of casting temperature, electromagnetic stirring or soft reduction are state-of-the-art technologies to achieve a beneficial cast structure and to reduce casting defects [34]. The remaining 3.7 % of the world steel production is manufactured via processes where these technologies are not available at all or only in parts. For example, in the case of large steel castings, a large fraction of equiaxed grains is essential for the center quality of the casting (porosities, hot cracks). Ingot casting still is the casting process of choice for most types of special steels, including stainless and tool steels. Due to their large amount of alloying elements both undergo severe macro- and microsegregation during solidification. Ferritic and austenitic steels are free from phase transformations in the solid-state and hence, the primary grain size is also the grain size at room temperature and decisive for mechanical properties. Many tool steels are characterized by high amounts of precipitates (mostly carbides) in this case prohibiting a columnar solidification may contribute to a refinement of the primary carbide structure and consequently to advanced properties.

In all these cases refining the primary solidification structure would be beneficial. As already stated in chapter 2.1, heterogeneous nucleation is an essential process during solidification. Therefore promoting active locations for nucleation in the melt can lead to a refined as-cast

structure. Basically there are two ways of approach, first are "physical" methods, where electromagnetic fields [35], electric current pulses [36,37] or ultrasonic vibrations [38] most commonly create fragmented dendrite tips, which act as inherent nuclei, besides those options mechanical mixing of semisolid alloys can also be applied [39]. The other approach focuses on "chemical" methods of heterogeneous nucleation. They bear the advantage of being independent of the shape and size of the casting and make use of foreign substances, which act as active nucleation sites. The application of such inoculants is the focus of this thesis.

## 3.2  Potential Nucleation Sites – *A theoretical Approach*

In general, two groups of grain refinement theories can be distinguished. The first one bases upon heterogeneous nucleation and has been considered as the only grain refinement mechanism for many years. An effective nucleant triggers solidification at a low degree of critical supercooling [40]. Nucleation sites are most effective if there is low interfacial energy between them and the solidifying phase. **Figure 3-1** displays the surface free energy for two different interfacial energies. A smaller $\gamma_{SL}$ leads to a slower rising surface free energy and thus to a lower activation energy $\Delta G_0$ and smaller critical radius $r_0$ for nucleation. One factor that is easy to excess and influences the interfacial energy is the crystallographic correspondence with the solid phase [41]. Turnbull and Vonnegut [42] were the first ones to propose such a theory. They were followed by Bramfitt [41] and more recently, also by the edge-to-edge matching model [43]. In addition to those theories, the free growth model concentrates on the particle size. It assumes a critical size that needs to be surpassed to reach irreversible nucleation [44]. For the sake of completeness, the second group of grain refining theories should also be mentioned. These theories focus on the role of segregating solute elements. The growth of the first solid phase can be restricted by segregating solutes, the segregation results in a constitutional supercooling zone in front of the solid-liquid interface and consequently a driving force for the formation of new nuclei within this zone. These newly formed nuclei restrict the growth of the first precipitated solid, similar to the critical ratio of equiaxed grains that stop the columnar growth (section 2.3) [45–47]. Cerium is considered to contribute to grain refinement via segregation as a solute in steel [48].
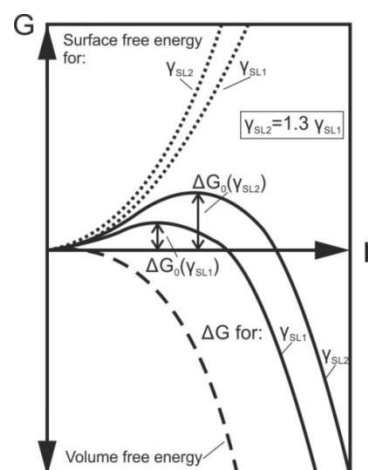


Figure 3-1: Changes of Gibbs free energy depending on interfacial free energy [49]

Grain refinement via inoculation is the main focus of this thesis. Thus it is discussed in more detail in the next paragraphs. For inoculants to be able to promote grain refinement by acting as heterogeneous nucleation sites, three basic requirements have to be fulfilled:

- they must be solid above the solidification temperature of the melt,
- thermodynamic stability must be given
- the wetting angle between the melt and the nuclei must be small [40,50].

If all of these requirements are met, one of the following criteria can be used to choose a favorable particle for inoculation.

### One-dimensional Lattice Disregistry

As already mentioned above, Turnbull and Vonnegut were the first to explain the potency of specific nucleation sites with the help of crystallographic correspondence between the inoculant and the nucleating phase. They proposed the one-dimensional lattice disregistry as follows:

$$\delta = \frac{|a_s - a_n|}{a_n} \tag{13}$$

$\delta$ is the lattice disregistry and $a_n$ and $a_s$ stands for the lattice constant in the low index crystal planes of the nucleus and the nucleating agent. The smaller value for $\delta$ corresponds to lower interfacial energy and therefore improves the potency for grain refinement. The limitation of this approach is that it is only applicable to systems were the inoculant, and the solid have the same atomic lattice structure [42].

### Plane-to-Plane Matching (P2PM) Model

This afore described model was further developed into the plane-to-plane matching (P2PM) model by Bramfitt. A new two-dimensional disregistry was proposed.

$$\delta_{(hkl)_n}^{(hkl)_s} = \sum_{i=1}^{3} \frac{\frac{\left| d_{[uvw]_s^i} cos\theta - d_{[uvw]_n^i} \right|}{d_{[uvw]_n^i}}}{3} \cdot 100 \tag{14}$$

$(hkl)_s$ is a low-index plane of the nucleating agent, $[uvw]_s$ is a low-index direction in the $(hkl)_s$, $(hkl)_n$ is a low-index plane of the nucleus, $[uvw]_n$ is a low-index direction in the $(hkl)_n$, $d_{[uvw]_n}$ is the interatomic spacing along $[uvw]_n$, $d_{[uvw]_s}$ is the interatomic spacing along $[uvw]_s$, and $\theta$ is the angle between $[uvw]_s$ and $[uvw]_n$. The most effective nucleants have disregistries below 6 %, moderately effective are those with a disregistry between 6 and 12 %, and above 12 % grain refinement is very unlikely [41]. **Figure 3-2** displays how $\delta$ corresponds to the actual undercooling of the melt. Particles, which have a beneficial crystallographic correspondence, like CeS or TiN, lead to small undercoolings. This means that they act as active nucleation sites, and the necessary activation energy for solidification is decreased. Inclusions like MnO or $Al_2O_3$, which have planar lattice disregistries lager than 12 % are deemed to be no effective nuclei because they lead to higher undercoolings during solidification [51].
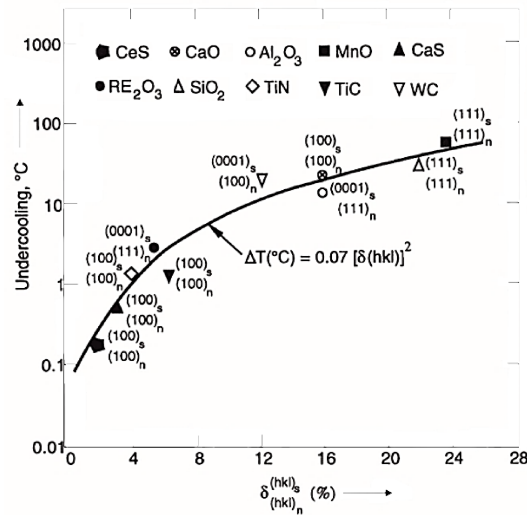
**Figure 3-2:** Relationship between planar lattice disregistry and undercooling for different nuclei in ferrite, adapted from [51]

### Edge-to-Edge Matching (E2EM) Model

The latest addition to these models is the edge-to-edge matching (E2EM) model. It was initially developed to explain the orientation relationships (ORs) and corresponding habit planes of diffusion-controlled solid-solid phase transformations [43,52]. The E2EM model was also successfully implemented to explain the mechanism of grain refinement in cast alloys and to find new grain refiners in Al, Mg, and their alloys [53,54]. It is also based upon the assumption that the interface between two phases strives towards the minimization of interfacial energy, which is reached by the maximization of atomic matching across the interface. The major difference to the P2PM model is that, while the latter uses lattice matching, the E2EM model examines the matching on the atomic scale. This is an advantage because, in reality, the atoms have to match across the interface rather than the lattice points. As criterions, it combines the interatomic spacing misfit ($f_r$) between a pair of close-packed rows and the interplanar spacing mismatch ($f_d$) between a pair of close-packed planes that contain the rows. **Figure 3-3** shows that no absolute matching of the atom rows is required, but the misfit must be relatively small for matching regions to occur. An upper limit of 10 % is feasible. The matching atomic rows can have straight or zigzag surfaces, but it is a requirement that straight rows are matched with consecutive rows and vice versa (**Figure 3-4**). Zigzag rows and straight rows cannot be matched. The interplanar spacing mismatch between the atomic planes is limited to 6 % [55].
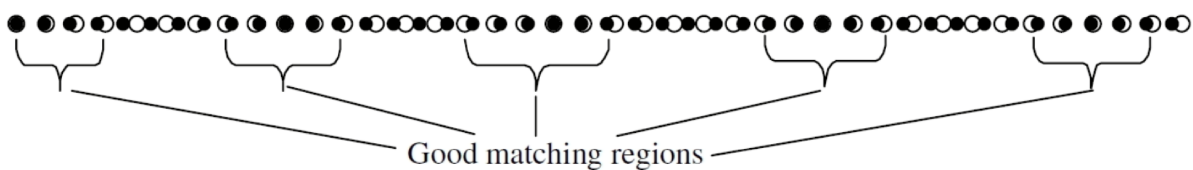


**Figure 3-3:** Atom row matching with a small misfit along the row direction [55]
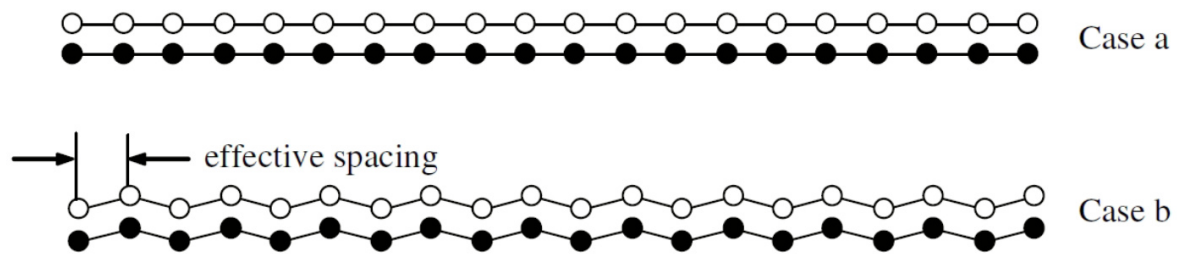
Figure 3-4: Atom row matching on a) straight row and b) zig-zag row [55]

While the E2EM is probably the more accurate and also more recent model, the available values for $f_d$ and $f_r$ are somewhat limited at the moment, and there are still many-particle/matrix systems missing. Therefore the P2PM misfit is used in this thesis to find promising inclusions for grain refinement. The appendix contains tables with misfit parameters for various compositions in relation to austenite or ferrite formation.

## 3.3  Review on Particles acting as Heterogeneous Nucleation Sites

Many authors reported about grain refinement via heterogeneous nucleation in various steel grades. Three general possibilities to induce these substances can be categorized:

- First, is the "in-situ" formation of particles through the reaction of a dissolved element like O, N, S or C with a partner alloyed to the melt like Ti, Zr or Ce.
- Second, is the application of master-alloys which typically consist to 50 % of particles with the required chemical composition and size and a matrix material with a composition similar to the refined alloy [56–59].
- And third, there is the possibility to work with powders [41,60,61].

The first option is the one favored by the author, because the reaction with dissolved elements that are evenly distributed in the whole melt leads to a regular occurrence of nucleation sites, as long as no severe flotation or clustering effects appear.

Table 3-1 holds an overview of publications structured into the reported effects on macro- and microstructure and the investigated steel grade. Expected improvements of a successful inoculation usually are an early columnar-to-equiaxed transition and the refinement of the original grain size. Publications reporting on such effects can be found in the first three columns under "Effects on macrostructure". Further events that can be promoted by heterogeneous nucleation are summarized under "Effects on microstructure". For the case of tool steels, this can be a modification of the carbides either in size or type or both. For carbon steel grades, the formation of acicular ferrite is reported through heterogeneous nucleation on certain particles. Acicular ferrite is a special type of ferrite that has improved mechanical properties. It is an example of a solid-state phase transformation triggered by heterogeneous nucleation. Details concerning the CET, grain refinement, and carbide modification are discussed in the following sections.

Table 3-1: Overview of the effects of heterogeneous nucleation sites on steel

| | | Effect on macrostructure | | | Effect on microstructure | |
|---|---|---|---|---|---|---|
| | | Columnar-to-equiaxed transition | Grain refinement | | Carbide-modification | Phasetrans-formations |
| | | | with α/γ trans-formation | without α/γ trans-formation | | e.g.: acicular ferrite |
| **Steel grade** | Carbon steel | [62–65] | [50,57,62,66–73] | | | [57,74] |
| | Austenitic stainless steel | [7,8,56,75] | | [5,7,8,56,75–77] | | |
| | Ferritic stainless steel | [78–80] | | [5,78–82] | | |
| | Duplex stainless steel | [83] | | [81,83] | | |
| | Tool steel | [84] | [60,61,84–99] | | [60,61,84–98,100] | |

### 3.3.1 Oxides

In carbon steel grades $Ce_2O_3$ is reported to act as nuclei for δ-ferrite by Guo and Suito [65], Nuri et al. [63] and Tuttle et al. [50,71]. Tuttle et al. applied up to 0.3 wt.-% of rare-earth-silicide and achieved a refined cast structure as well as higher yield strength (YS), ultimate tensile strength (UTS) and a drastic increase in percent elongation. **Figure 3-5** shows how the solidification changed from columnar-dendritic to equiaxed-dendritic [71]. Morioka and Suito et al. [64,72] tested various inoculants, e.g. Zr, Al, Mg, Ce, and Ti and also found $Ce_2O_3$ to be the most effective for δ-solidification. If the carbon content was high enough for solidification via austenite, $ZrO_2$ led to the highest amount of equiaxed solidification [64].
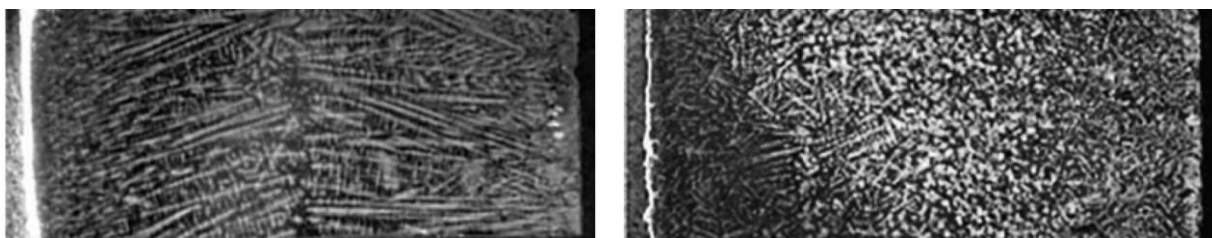


Without addition       With addition of 0.2 wt.-% rare-earth-silicide

Figure 3-5: Refined cast structure of low carbon steel, etched, magnification x7 [71]

Another author suggested that by adding pure titanium in a quantity of 0.058 wt.-% $Ti_3O_5$ nanoparticles are formed, which lead to a refined grain structure but also improve the properties due to precipitation hardening [70].

For austenitic manganese or nickel steel grades, $CeO_2$ and $AlCeO_3$ are favorable particles. When surpassing a critical cerium content of 400 ppm, the grain size drops and the columnar shell gets smaller, but also the highest particle density is reached. In **Figure 3-6**, the relationship between

grain size and cerium content of particles per $mm^2$ is enlightened [7,8,101]. Dahle reported that the cast structure of super duplex steel could be refined by the addition of a commercial Ce-containing grain refiner (EGR). Complex $(AlCeSi)_2O_3$ and $CeSiO_2$ were identified as active NMI. While YS, UTS, and elongation increased, the impact toughness of the grain refined steel decreased [83].
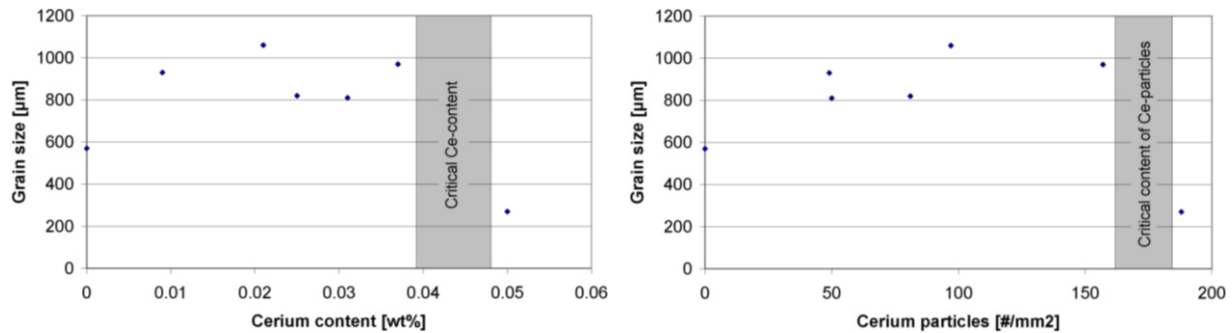


Figure 3-6: Grain size over cerium content and number density of cerium particles [7,8]

The bearing steel grade 100Cr6 is susceptible to NMI, but the content of 192 $CeO_2$/$mm^2$ and 47 CeS/$mm^2$ did not only enhance the amount of equiaxed solidification and refined the original grain size, but additionally, an improvement of the rolling contact fatigue life was reported [84]. In high-speed steels, the distribution of eutectic carbides along the dendrites and primary carbides is essential. Different publications show a grain refining effect of $Ce_2O_3$ and also report on carbide modification or a reduction of coarse carbides [87,89,96,100]. Until now there exists no satisfying explanation for the modification of carbides by Ce and rare-earth metals (REM) in general, but on the one hand the effect is traced back merely to the potential of $Ce_2O_3$ to trigger the primary solidification [89], on the other hand, it is referred to the segregation effect of Ce ahead of the solid-liquid interface, that can restrict the growth of previously formed solid phase, and could lead to increased divisions, neck contraction and separation of austenite dendrites and a refinement of the eutectic structures [48,87].

### 3.3.2 Oxysulfides / Sulfides

CeS and $Ce_2O_2S$ are reported to have a grain refining and enlarging effect on the equiaxed structure of carbon steel and tool steel [63,65,73,97]. In the case of tool steels containing the chromium carbide, $M_7C_3$ Hamidzadeh et al. stated that $Ce_2O_2S$ acts as a nucleation site for this carbide and Tehovnik et al. found a change from lamellar to the better globular shape of $M_7C_3$ [102,103]. But besides these positive results, in [101] $Ce_2O_2S$ and cerium phosphides were identified as disadvantageous for the toughness.

### 3.3.3 Nitrides

Titanium nitride is the most common nitride acting as heterogeneous nucleation site for ferrite during solidification [62,79,80,82,104,105]. For the successful application of TiN, a parent nuclei in the form of $Al_2O_3 \cdot MgO$ or MgO is helpful [62,79,82,104]. Wang et al. concluded that while $Al_2O_3$ can act as a nucleation site for TiN too, it also leads to oxide clusters and therefore no grain refining

effect occurs, as long as the aluminum content in the melt is not decreased. With very low Al amounts in the steel, TiN can nucleate on fine dispersed $Ti_2O_3$ [105]. **Figure 3-7** shows how different magnesium and titanium additions influence the macrostructure of ferritic stainless steel. For them, this grain refinement mechanism is of special interest, because a fine-grained structure is important to reduce riding, a surface defect which occurs during deformation [79,82]. Besides all these factors, which have to be taken into account, for the TiN formation, it also has to be considered that the inclusion landscape in the melt is time-dependent. In the case of simultaneous addition of Mg and Ti the inclusions change from MgO to MgO(core)+TiN(shell) to $Ti_2O_3$ in 60 min, this corresponds to a shift in solidification structure from columnar to equiaxed to columnar [104].
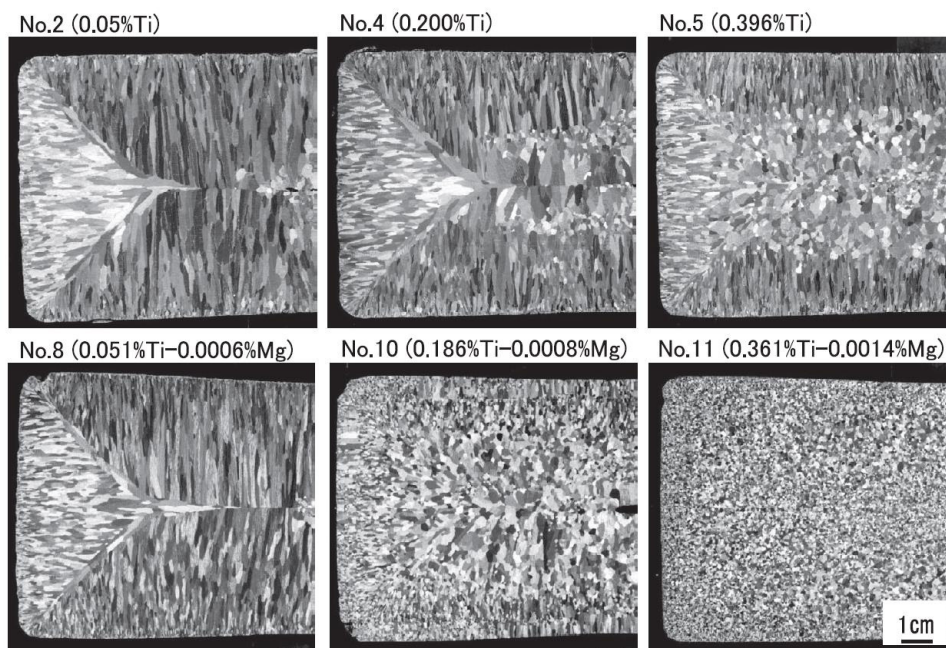


**Figure 3-7:** Effect of combined Mg-Ti treatment on ferritic stainless steel [79]

### 3.3.4 Carbides / Carbonitrides

As carbides are essential phases in tool steels, carbides are rather used as heterogeneous nucleation sites in these grades, than in low alloyed or stainless steels. In tool steels normally many strong carbide forming elements are already present, therefore elements like Ti and Nb with an even higher affinity for carbide, nitride or carbonitride formation have to be used to alter solidification. Nucleation can either follow the sequence $Al_2O_3 - Ti(C, N) - MC - \delta$-ferrite (M=predominantly vanadium), or TiC/NbC — austenite/$\delta$-ferrite. It is important to notice that Ti and Nb reduce the amount of C in the remaining liquid. So there is less carbon that remains for the eutectic, carbide-forming reaction, which can lead to a decrease of overall carbide content. This can result in beneficial mechanical properties of the steel, but it has to be taken under account if the change of the eutectic carbides is intended [86,88,91–95,98]. Improvement regarding the carbide distribution is reported by Löcker. The inoculation with $Al_2O_3 - Ti(C, N) - MC$ resulted in a finer equiaxed grain structure in HS6-5-2. He found that an even distribution of $Al_2O_3$ is necessary to guaranty a homogeneous inoculation effect. **Figure 3-8** shows how a beneficial distribution leads to an improved uniform carbide distribution, while **Figure 3-9** pictures that an

inhomogeneous occurrence results in the formation of carbide clusters. These are disadvantageous, because an accumulation of carbides in the cast-structure, cannot be dissolved during hot deformation [99].



**Figure 3-8:** Improvement of carbide distribution through homogeneous distributed nucleation sites (x20) [99]



**Figure 3-9:** Carbide clusters through inhomogeneous distribution of nucleation sites (x20) [99]

Nevertheless, there are some examples of other steel grades influenced by carbides. The grains of austenitic stainless steel can be refined with an additive containing NbC. Additions of 3 wt.-% of a Fe-Nb-C master alloy led to a fine-grained structure, but the effect faded away in 60 s due to the instability of NbC in austenitic stainless steels [77]. In the case of plain carbon steel (Nb, Ti)C particles, manufactured through mechanical alloying, were applied. They refined the macrostructure and also altered the final microstructure by increasing the ferrite content at the expense of perlite [57].

### 3.3.5 Conclusions concerning the grain refinement of X1CrNiMoCuN20-18-7 and HS2-9-1-8

The first phase solidifying for both of the steel grades discussed in this thesis is austenite. From the literature review, $AlCeO_3$ emerges to be a very useful particle to trigger heterogeneous nucleation for austenitic steel grades. It is thermodynamically very stable and solid above the liquidus temperature. Additionally, its density of 6.62 $g/cm^3$ is rather high for a non-metallic inclusion. This is favorable because it prevents flotation effects. Depending on the regarded lattice planes and directions, the planar lattice misfit varies between 5.0 and 5.9 %. Thus $AlCeO_3$ is applied in SASS and HSS to act as a heterogeneous nucleation site. Additionally, it is reported that Ce can influence the carbide size in its dissolved form by segregating ahead of the solid-liquid interface and restricting the growth of previously precipitated solid. Thus the potential exists that the application of Ce simultaneously leads to grain refinement via $AlCeO_3$ and reduces the carbide size.

Thermodynamic stability and a small misfit would be given for TiN in the SASS as well. But the application of Ti is not allowed for this steel grade, so it is no possible course of action. For the HSS, on the other hand, the usage of Ti is acceptable. Under normal circumstances, the grain refinement of HSS occurs through the following sequence: oxide particles like $Al_2O_3$ act as parent nuclei for TiN or TiC, which are nucleation sites for MC that facilitates the precipitation of primary iron phase. The reviewed literature does not always differentiate very well between the influence of grain refinement on the primary carbide distribution and carbide size. While it can be assumed that the grain refinement of the primary iron phase does influence the carbide distribution and the ledeburitic carbide network, it is not sure at this point if the carbide size can be altered as well.

## 3.4 Formation of Particles in Steel – *Thermodynamic Considerations*

The sources of inclusions in steel are manifold: In general, exogenous and endogenous inclusions can be distinguished. Exogenous inclusions result from the contact between steel and slags (e.g. entrapment) and refractories (e.g. erosion). Endogenous inclusions result from chemical reactions in the bulk or along with the interfaces steel/slag/refractories. Exogenous inclusions are most harmful as they are mostly macroscopic, and their existence is difficult to predict. Macroscopic inclusions worsen mechanical properties, fatigue resistance, and corrosion resistance, to name a few features. For microscopic inclusions – and inclusions for heterogeneous nucleation are typically in a size of one micron or less – thermodynamic considerations are helpful to predict their chemistry based on the chemical composition of the steel. Inclusion kinetics is useful to predict the size of inclusions and also a potential change of their nature due to modification. Thermodynamics is applied in high-temperature metallurgy to gain an understanding for which reactions and processes are possible and how large the driving force is [2]. Nowadays, software tools like FactSage or Thermocalc are used to enable us to perform thermodynamic calculations for very complex systems with two and more components.

As established above, $AlCeO_3$ is an extremely promising particle for active grain refinement, therefore defining the limits of its formation with the help of thermodynamic calculations is useful.

When the temperature of the melt decreases during solidification or teeming, the solubility of oxygen is decreasing. Thus alloying elements like Ce and Al may react with oxygen, according to the formula in equation (15), and form the reaction product $AlCeO_3$. The equilibrium constant K is given in equation (16) and can be calculated as the quotient of the activities of the product and the reactants [49].

$$Al + Ce + 3O \leftrightarrow AlCeO_3 \tag{15}$$

$$K = \frac{a_{\mathrm{AlCeO_3}}}{a_{Al}a_{Ce}a_O^3} \tag{16}$$

If the reaction in equation (15) is in equilibrium ($\Delta G = 0$), equation (17) can be given. It brings the equilibrium constant K into context with the Gibbs free energy $\Delta G^0$ in equilibrium (R…ideal gas constant). If $\Delta G^0$ is negative, a reaction is thermodynamically able to happen [49]. At 1600 °C the value for $\Delta G^0$ is $-648\,313$ kJ/mol for the formation of $AlCeO_3$ [106,107].

$$\Delta G^0 = -RT \, lnK = -648 \, 313 \text{ kJ/mol} \tag{17}$$

In comparison to $AlCeO_3$, $\Delta G^0$ is only $-478 \, 924$ kJ/mol for the formation of $Al_2O_3$ according to the formula given in equation (18) [106,107]. This means at 1600 °C $AlCeO_3$ is more stable than $Al_2O_3$.

$$2Al + 3O \leftrightarrow Al_2O_3 \tag{18}$$

The software tools mentioned above help to forecast the stable compounds of complex more component systems. Their basis is the minimization of the Gibbs free energy of a system, and they can access various pure substances and solution databases. Different parameters can be changed for such a calculation, for example, pressure, temperature, or the content of a component. If the data is complete and the degrees of freedom are met, the programs can calculate phase diagrams, property diagrams, and many other thermodynamic values.

An example of such a calculation performed with FactSage 7.0 is given in **Figure 3-10**. It shows a Ce/Al phase diagram in a Fe system containing 75 ppm O and 40 ppm S. The framed areas correspond to the predominance regions of the individual particles. Besides being a highly active partner for oxygen, cerium also reacts very strongly with S forming sulfides and oxisulfides. In this particular system, $Ce_2O_2S$ formation has to be taken under account when a threshold of approx. 0.08 wt.-% Ce is passed. The stability area of $Ce_2O_2S$ is seemingly independent of the Al content. $AlCeO_3$ inclusions can precipitate for Ce levels between $10^{-5}$ and 0.08 wt.-% and Al from $10^{-5}$ to 8 wt.-%. Reasonable alloying contents that result in a high number of $AlCeO_3$ lie near the single-phase stability region of this particle at contents of approx. 200 ppm Ce and 100 ppm Al [108].
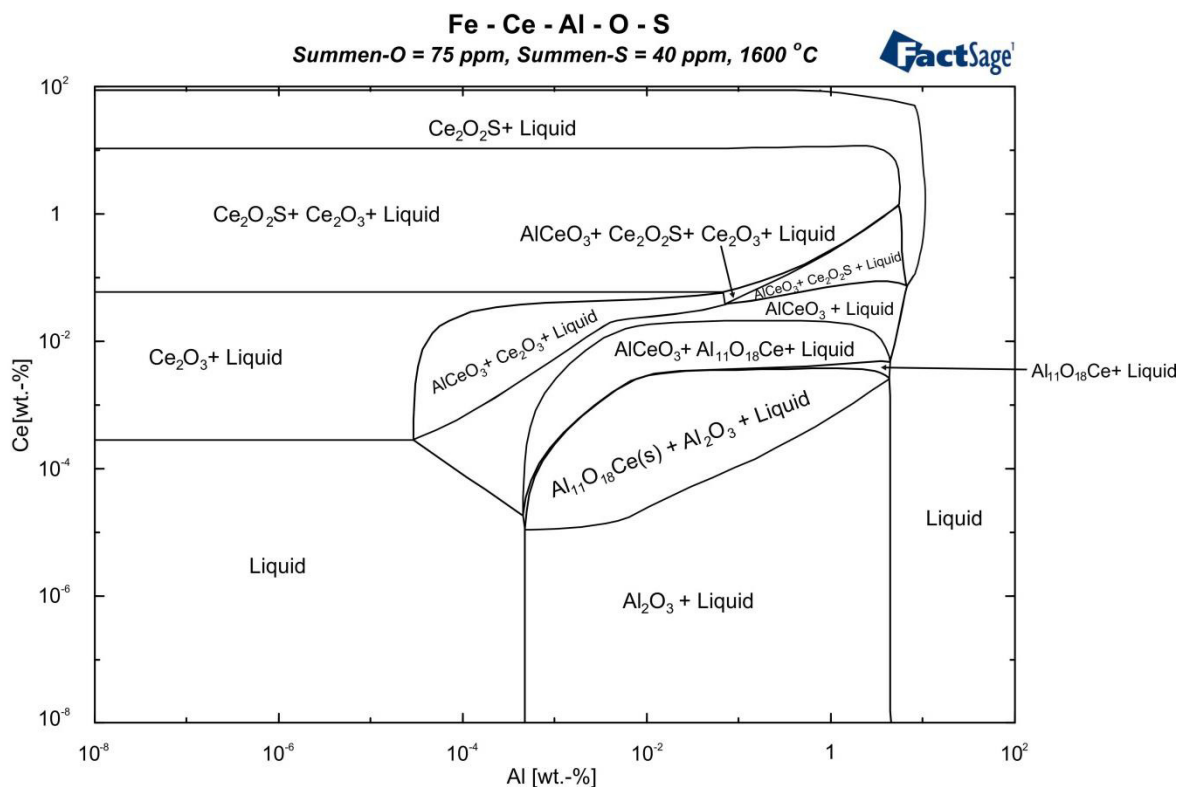


**Figure 3-10:** Ce/Al phase diagram in a Fe-Ce-Al-O-S system at 1600 °C with 75 ppm O and 40 ppm S (calculated with FactSage 7.0; databases FSStel, FTOxid and SGPS) [108]

## 3.5 Summary

Manufacturing methods like ingot casting and heavy steel castings do not offer the same simple technological measures for the improvement of solidification structure as the continuous casting process. For these processes, the application of in-situ formed nucleation sites via NMI that are independent of dimensions, size, and casting process, is a promising research topic.

The criteria which particles have to fulfill to be active nuclei can be summarized as follows:

- They need to be thermodynamically stable,
- solid above liquidus temperature,
- and a suitable wetting between particle and melt must be given.
- When all of these points are met, the inclusions must be checked for the crystallographic correspondence with the primary solidifying phase. The model applied in this thesis is the P2PM model. Particles with misfits smaller than 6 % are considered highly active to promote grain refinement.

The in-situ formation of nuclei is favored because the least difficulties with the homogeneous distribution of the particles are expected. Besides grain refinement, the effects of inoculation can also alter the CET, as well as carbide structures and can even promote phase transformations like the formation of acicular ferrite. Very popular is the application of rare-earth metals, for example Ce, they form various oxidic and oxisulfidic particles. $AlCeO_3$ and $\gamma$-austenite have a planar misfit of 5 %, and it is a very promising nucleation site for the SASS X1CrNiMoCuN20-18-7.

For the HSS HS2-9-1-8, it has to be distinguished between the influence of inoculation on the primary grain structure and the eutectic carbides. From the literature review, it is unclear if there is an interaction between those two or if they are independent of each other. Various authors report on the carbide modifying effect of cerium, but they do not agree on the cause. Some see the grain refining effect of the heterogeneous nucleation through Ce-oxides or -sulfides as deciding factor, while others include the segregation effect of Ce ahead of the liquid-solid interface, that can restrict the growth of the eutectic. To enhance the understanding of the effect of Ce on HS2-9-1-8 test is performed in the experimental part of this thesis.

Another interesting approach to influence the primary structure of HSS is the application of titanium. It is reported to precipitate as Ti(C, N) that facilitates the MC formation. The latter acts as a heterogeneous nucleation site for austenite or $\delta$-ferrite. This should lead to an earlier CET and a finer primary grain structure. If the size of the primary carbides can be influenced as well is tested in the practical part.

# 4 Experimental Procedures

The following chapter describes the experimental methods used in the course of this thesis. It also holds the settings for tests performed with a Gleeble forming simulator and the details of the metallographic and analytical procedures.

## 4.1 Melting and Solidification Experiments

The melting experiments are performed on two melting apparatus. The first is an open-hearth induction furnace (IF) with a capacity of 20 kg and the second is a vertical tube furnace with an inert gas atmosphere (=Tammann-type furnace; TO), which can hold around 300-400 g of melt.

### 4.1.1 Experimental Procedure on the Induction Furnace

An induction furnace from Inductotherm is applied for the melting operations. It has a maximum capacity of 20 kg and can reach temperatures as high as 1650 °C. For melting it utilizes electromagnetic forces. The refractory material consists of magnesia lining with a MgO content of 98 wt.-%, and there is the possibility of flushing the surface with argon inert-gas. **Figure 4-1** shows the primary sequence of all experiments performed on the IF. The first step is melting industrial raw material provided by vBEG. Afterwards, a lollipop sample is analyzed, and the chemical composition readjusted to the original contents in one or two steps. Then the temperature of the melt is adjusted to the requested casting temperature, afterwards, whether necessary the inoculation treatment is performed. When the melt treatment is finished, it is top poured into grey iron molds, in the form of small 12 kg ingots and dimensions of approx. 80x80x270 mm. For some experiments the possibility of preheating the molds with gas-jet burners to approx. 400 °C is applied.

With this kind of procedure, the influence of casting conditions (e.g., varying casting temperature or preheating of the mold) and the effect of inoculation on X1CrNiMoCuN20-18-7 and HS2-9-1-8 is investigated.
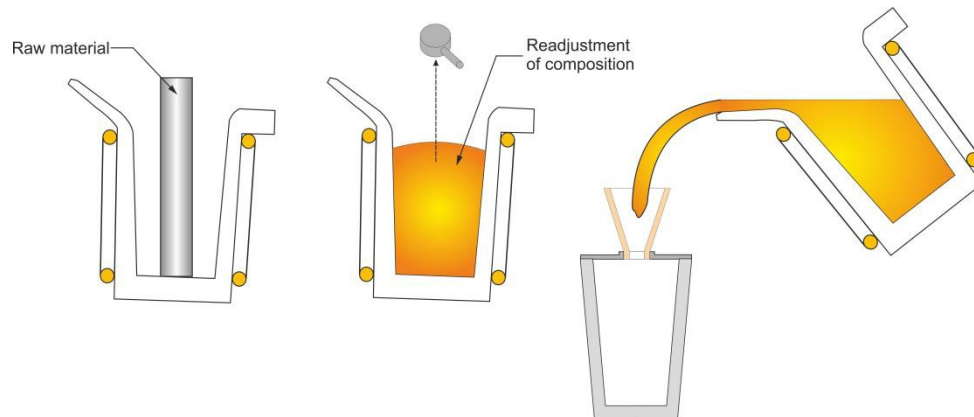
**Figure 4-1:** Experimental procedure at the IF – Melting – Readjustment of composition (possibly inoculation) – Casting

## 4.1.2 Experimental Procedures on the Tammann-type furnace

The Tammann-type furnace is a vertical tube furnace manufactured by Ruhrstrat GmbH. It has a capacity of up to 500 g and utilizes resistance heating through a graphite tube. The furnace control enables controlled heating and cooling of the samples. To prevent the formation of CO-gas the furnace shell, as well as the working area, is flushed with argon or nitrogen as protective gas. This holds the advantage of a controlled atmosphere surrounding the whole experimental work area and prevents oxidation. **Figure 4-2** shows the cross-section of the furnace.
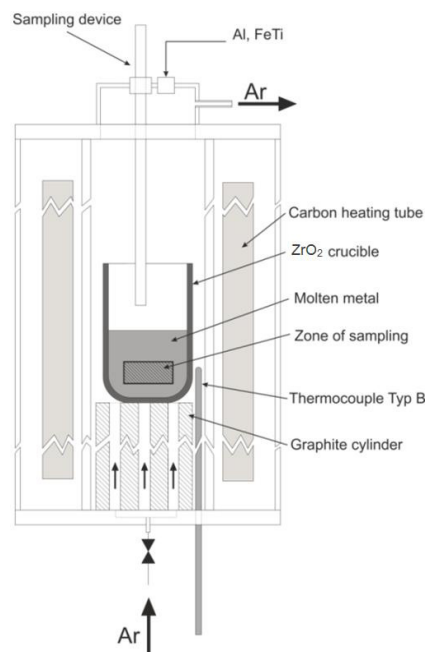


**Figure 4-2:** Cross-section of the vertical tube furnace [109]

### Tests on Inclusion Formation

The first type of experiment performed on the TO is designed to investigate the formation of inclusions containing cerium and aluminum. **Figure 4-3** pictures the procedure. The raw materials charged into a $ZrO_2$ crucible are X1CrNiMoCuN20-18-7 and additionally on-demand technically pure iron containing 2000 ppm of oxygen. The crucible material is chosen because it is considered inert against reactions with cerium [108].

**Figure 4-4** shows the time-temperature profile of the tests. The temperature is increased to 1545 °C, although the liquidus temperature of the SASS is much lower. The high temperature has to be chosen to ensure the melting of the oxygen-containing pure iron. Additionally, 10 min of waiting time is applied after reaching 1545 °C to give the raw materials enough time to melt completely and reach a homogeneous state. After this period, an initial sample P0 is taken. In general, the specimen is sucked in a steel tube out of plain carbon steel with the help of a flip-style pipette filler [109]. The probes are taken from the middle of the melt, as indicated in **Figure 4-2**. They are quenched in water immediately to freeze the inclusion population in the liquid. Directly after P0, a stainless steel tube containing cerium and aluminum is sunk into the melt. Then every 10 minutes, further samples are retrieved from the melt. This is repeated up to 3 or 4 times. As soon as the last specimen is taken, the furnace control is changed into the cooling mode, and the solidified regulus is quenched in water when the furnace reaches a temperature of 300 °C.
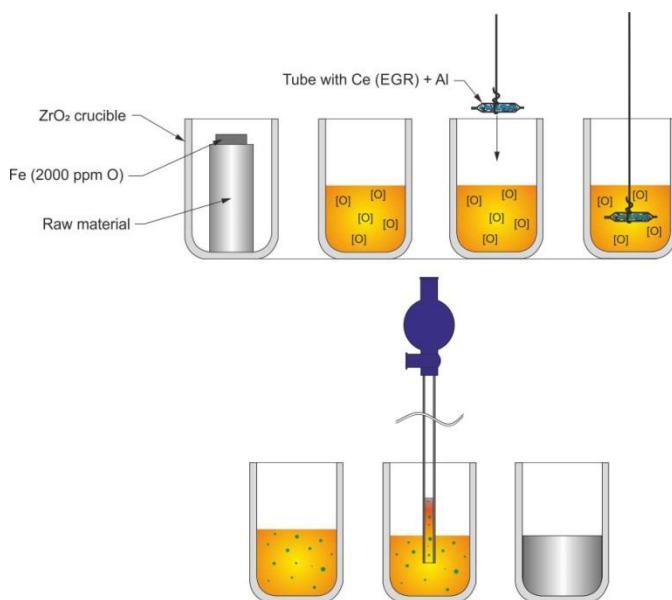


Figure 4-3: Experimental procedure of the inclusion formation test – Melting – Homogenization – Alloying – Inclusion formation – Sampling – Cooling
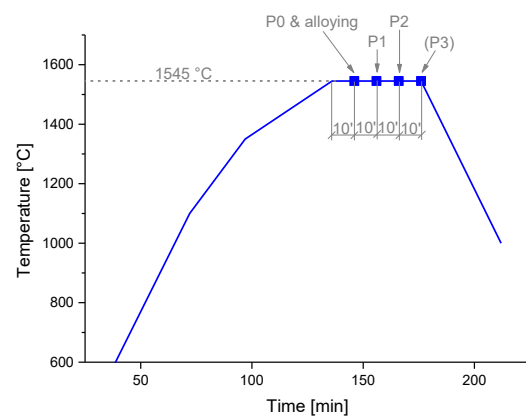


Figure 4-4: Time-temperature profile of the inclusion formation test

**Tests with defined Cooling Rate**

The influence of cooling rate on the solidification structure and carbide formation in HS2-9-1-8 is enlightened by using the possibility of applying a defined cooling regimen at the TO. For these experiments, 300 g of HS2-9-1-8 is heated up to 1500 °C. When the final temperature is reached, the melt is given 10 min to homogenize. Then the cooling procedure starts. Cooling rates of 1, 5, and 15 K/min are applied until a temperature of 1150 °C is reached. Below this point, all tests are finished with a cooling rate of 15 K/min and the regulus is quenched, when 300 °C are passed.
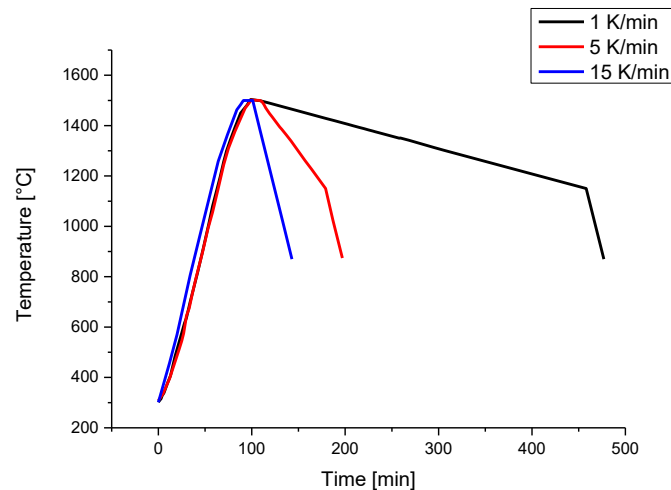
**Figure 4-5:** Time-temperature profile for TO tests with a defined cooling rate

## 4.2 Deformation Experiments with a Gleeble Machine

A Gleeble 3800 situated at vBEG is applied for deformation experiments in this thesis. It is a thermo-mechanical physical simulation system that allows for 20 t of force, heating rates of 10000 °C/s and stroke rates of 2000 mm/s to be applied to a specimen. To investigate, if the grain refining effect can be retained after hot deformation and recrystallization, experiments are performed on this machine.

The parameters of the experiment are defined with the help of industrial X1CrNiMoCuN20-18-7 material in a re-annealed state with enlarged grains. The most promising time-temperature plot is shown in **Figure 4-6**. At first, the sample is heated to 1150 °C and homogenized for 10 min, then it is cooled to 800 °C, where it is pressed to a degree of deformation of 0.8 and at last, it is heated to 1100 °C for recrystallization and grain growth. At this temperature, different holding times between 60 s and 3600 s are applied.
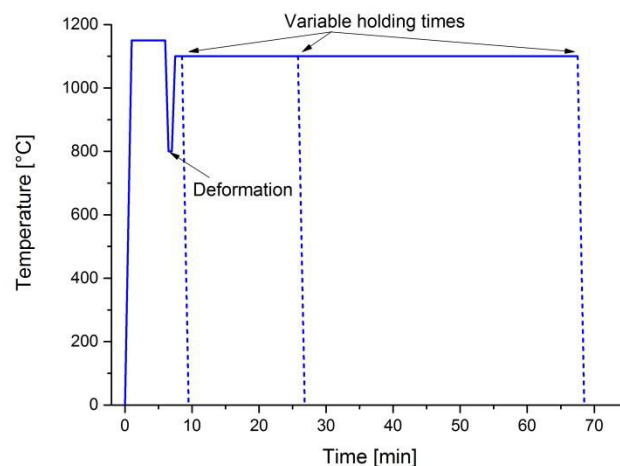


**Figure 4-6:** Time-temperature profile of Gleeble experiments

## 4.3  Metallographic methods

This section gives an overview of the sample preparation and metallographic methods used in the course of this thesis. Basically there are three types of samples. The first is to investigate the macrostructure, the second for measurements via light microscope and the third type for observations via SEM-EDS or SEM-EBSD.

### 4.3.1  Investigation of the Macrostructure

For the analysis of the macrostructure, the cast ingots have to be cut, ground and etched. Afterwards, different methods are applied to retrieve various parameters defining the macrostructure.

**Cutting and Sample Preparation**

Figure 4-7 shows how the ingots are cut and which surfaces are prepared for the etching of the macrostructure. For both steel grades, the ingot is separated 80 mm from the bottom and then sectioned vertically exactly in the middle. The upper part of the ingots is reserved for hot deformation and the investigation of mechanical values that are not part of this thesis. The blue highlighted area is prepared for the SASS and the red for the HSS. While the separation of X1CrNiMo20-18-7 can be facilitated with simple methods like a bandsaw and abrasive cutting wheels, the sectioning of HS2-9-1-8 is performed with waterjet cutting, because of the high hardness. Otherwise, it would have been impossible to cut the HSS without previous heat treatment or methods that induce heat during cutting. For the investigation of the solidification structure heating the samples should be avoided. The disadvantage of waterjet cutting is the rather rough surface finish that makes a high amount of grinding necessary. For this reason, a smaller area is chosen for the investigation of the solidification structure for the HSS (see red highlighted area in Figure 4-7).
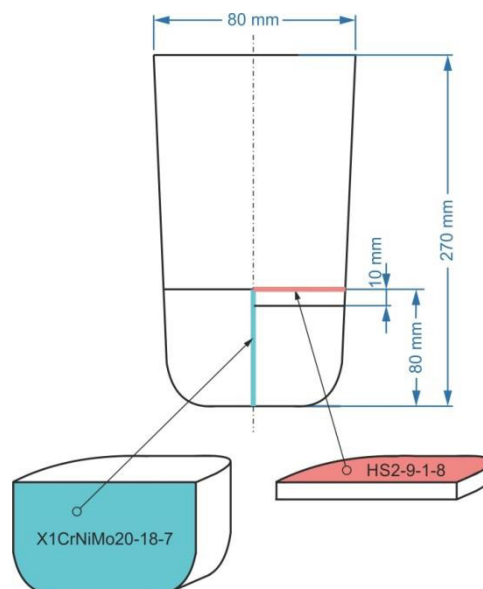


Figure 4-7: Position of sectioning and prepared areas (blue…SASS; red…HSS)

The further processing steps are grinding down to grade 1200 grit-paper and only for HSS also polishing with diamond polishing suspension (9 and 3 µm). Then the specimens are etched according to **Table 4-1**. On X1CrNiMoCuN20-18-7, a strong etchant on HCl basis with copper-chloride and $H_2O_2$ is applied for 4 to 6 min. HS2-9-1-8 is treated with 10% Nital to reveal the macrostructure. The specimens are immerged for several minutes in the acid until a clear result is gained.

**Table 4-1:** Applied etchants

| Steel grade | Application | Etching name | Etchant composition | Applied time |
|---|---|---|---|---|
| SASS | Macrostructure, primary grain size | B-etching | 100 ml $H_2O$, 300 ml HCl, 15 ml $H_2O_2$, 5 g CuCl | 4-6 min |
| SASS | Austenite grain size | V2A etchant | 100 ml $H_2O$, 100 ml HCl, 10 ml $HNO_3$, 2 ml Dr. Vogel pickling inhibitor | 30 s @ 60 °C |
| HSS | Macrostructure | 10% Nital | 90 ml $C_2H_6O$, 10 ml $HNO_3$ | Minutes |
| HSS | Dendrites | 3% Nital | 97 ml $C_2H_6O$, 3 ml $HNO_3$ | Minutes |

**Applied Measurement Methods**

The quantitative characterization of the grain structure on the ingot samples comprises the following analytics:

- The position of the columnar to equiaxed transition and the ratio of equiaxed solidification
- and if the appearance of the primary grains on the macro-etchings is sufficiently clear, also the number and number density of primary grains close to the ingot center.

The macrostructure was captured via a high-resolution single-lens reflex camera. The contrast of the photographs was mostly sufficient for the SASS to analyze the CET as well as the number of primary grains in a defined area. **Figure 4-8** shows a schematic sketch. Over a length of 50 mm a grid of 13 lines is applied, and the length of the columnar area is measured on both ends. In equation (19) the mean value of all these measurements is used to calculate the ratio of equiaxed solidification $R_{Eq}$. The average equiaxed area $\overline{A_{Eq}}$ is given by equation (20). The last step is counting the number of equiaxed grains $N_{Gr}$ within the $80 \times 50$ mm area marked in **Figure 4-8**. Then equation (21) can be used to calculate the average area per grain $\overline{A_{Gr}}$ and the mean equivalent area diameter $d_A$ is given by equation (22) [110]. Because of the limited number of grains and their size, the calculation of $d_A$ had to be adapted from ASTM E112 and is not an exact application of the standard [111].

$$R_{Eq} = \frac{1}{80 \text{ mm}} \cdot \frac{\sum_{i=1}^{n}(80 \text{ mm} - 2l_i)}{n} \tag{19}$$

$$\overline{A_{Eq}} = R_{Eq} \cdot 80 \text{ mm} \cdot 50 \text{ mm} \tag{20}$$

$$\overline{A_{Gr}} = \frac{\overline{A_{Eq}}}{N_{Gr}} \tag{21}$$

$$d_A = \frac{1.5}{1.2} \sqrt{\frac{\pi}{4} \overline{A_{Gr}}} \tag{22}$$
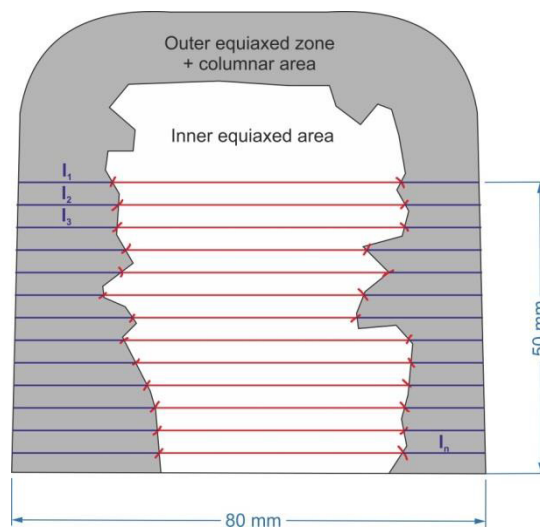
Figure 4-8: Measurement of the CET in SASS

For the HSS the CET is marked in mosaic images captured with an optical microscope Nikon MM 40. **Figure 4-9** shows an example. The mosaics are used to mark the CET, and then the same methods as for the SASS are applied to define the ratio of equiaxed solidification $R_{Eq}$. The number of equiaxed grains cannot be detected for HS2-9-1-8, but qualitative differences regarding the appearance of the primary grains are made visible with SEM images.
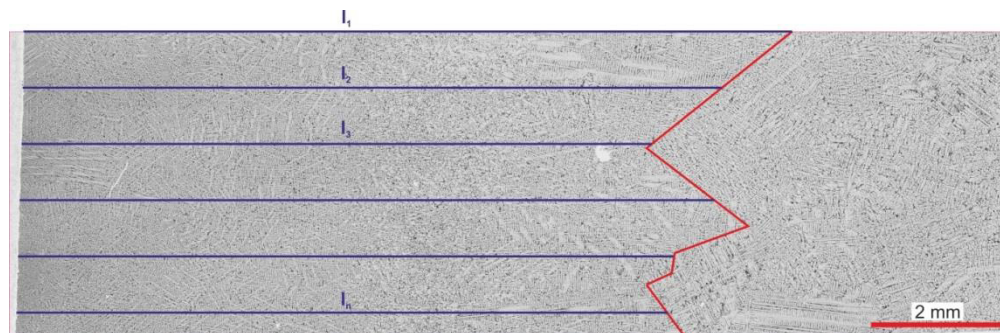
Figure 4-9: Measurement of the CET in HSS

## 4.3.2 Investigation of Microstructure via Light-Microscopy

Two measures are identified on etched samples namely the austenite grain size on samples retrieved from the Gleeble experiments and second the secondary dendrite arm spacing on the HSS samples.

**Gleeble Samples – Industrial SASS**

To perform the preliminary Gleeble tests specimens are machined out of industrial material. The pressed cylinders are cut in a vertical line in the center. The level cutting surface is embedded and prepared for etching. V2A etchant is applied with 60 °C for 30 s to reveal the grain size of the recrystallized austenite (see also **Table 4-1**). Then the line intercept method is used to generate

the mean intercept length $l_m$. Equation (23) shows how to convert $l_m$ into the mean equivalent area diameter $d_A$ [110].

$$d_A = \frac{1.5}{1.2} l_m \tag{23}$$

**Secondary Dendrite Arm Spacing – HSS**

Samples taken from the plate shown in **Figure 4-7** are used to investigate the secondary dendrite arm spacing. They are etched with 3% Nital according to **Table 4-1** and $\lambda_2$ is measured with the help of the line intercept method. For an accurate evaluation only secondary arms attached to a primary arm are valid to detect $\lambda_2$. This is easily possible in the columnar ingot area, but in the equiaxed area the correct identification of primary, secondary and tertiary arms is more challenging.

### 4.3.3  SEM Investigations

Various kinds of SEM investigations are used in the course of this thesis, for more information on the functioning of a SEM please refer to the relevant literature. This section shall only give an overview of the special metallographic techniques that are applied for the evaluation. If not stated differently, the samples are always taken from the red highlighted area shown in **Figure 4-7** and the measurements are performed in the ingot center. The standard specimens are ground and polished down to 3 μm. Only the EBSD samples are additionally treated with 1 μm diamond suspension and OPS.

**Carbide Structure Investigation on HSS**

The carbide structure is one of the primary interests of this thesis. A criterion suggested in a patent by Hitachi is adapted to investigate the carbide structure. Within this patent, carbide structures thicker than 3 μm are defined as massive or coarse carbides  [112]. This threshold is decreased to 1.2 μm, because in most samples the amount of structures thicker than 3 μm is not sufficient enough to ensure a statistically valid value.

Electron pictures recorded with the JEOL 7200F SEM typically with a magnification of 200 are used for the image analysis with the software "Clemex Vision 7". The carbides have a very distinctive grey threshold in comparison to the grey matrix. This can be used to determine the entire carbide area and then with a feature of the software called "String Width", it is possible to evaluate the amount of coarse carbides. "String Width" can be used to detect the width of thin and long structures, as can be seen in **Figure 4-10**. It is calculated according to equation (24) [113]. This course of action gives a quantitative value to determine how coarse the carbide structure is, this is an invaluable advantage in comparison to the often only qualitative assessment of the solidification structure of HSS. **Figure 4-11** gives an example, blue is the entire carbide area and green additionally marks the coarse carbides.

$$String\ With = \frac{perimeter - \sqrt{perimeter^2 - 16 \cdot area}}{4} \tag{24}$$
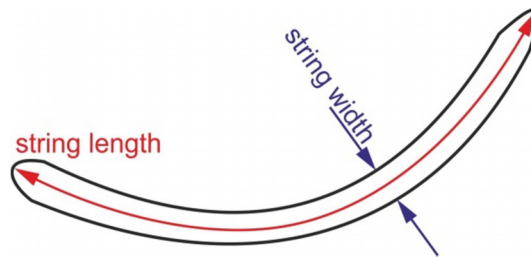
Figure 4-10: Definition of "String Width" [113]
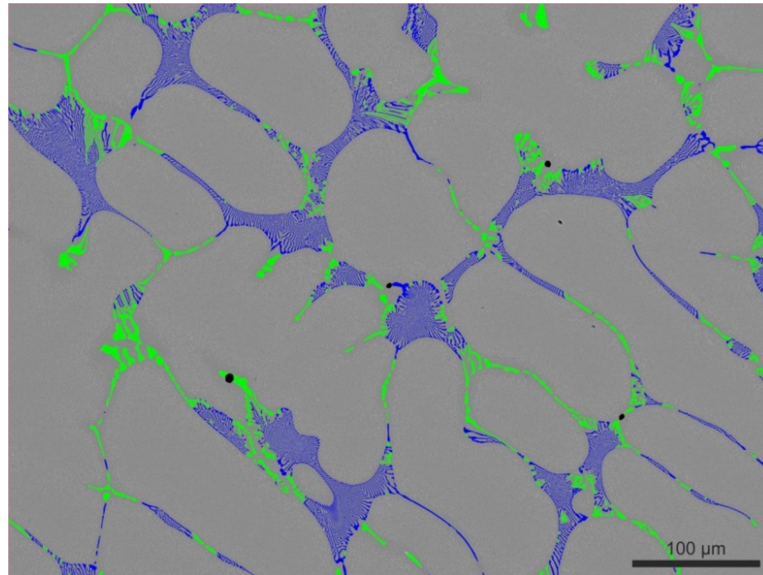


Figure 4-11: Example for the examination of coarse carbides (blue – entire carbide area; green – carbides thicker than 1.2 µm)

## Automated SEM-EDS Feature Analysis of Non-Metallic Particles

Feature analysis is a tool that gives the possibility to measure the size and chemical composition of a statistically adequate number of inclusions to get a clear picture of the inclusion population. Michelic et. al. elucidate this very detailed in [114]. The data generated with this analysis has to be classified. For this the chair of Ferrous Metallurgy has its own software tool to evaluate standard inclusions containing elements like Al, Mg, Ca, Si, S and O, this tool is not sufficient enough to give an exact classification of the complex Ce-containing inclusions in the SASS and also not for the carbides and carbonitrides in the HSS. **Figure 4-12** provides the classification with schemata for oxides containing cerium used for the TO experiments on inclusion formation in SASS. The other classifications used for the evaluation of the feature measurements of this thesis are given in the appendix. It has to be noted that this are specific custom-tailored classifications for each special inclusion landscape in this thesis, thus they must be adapted to fit other experiments.
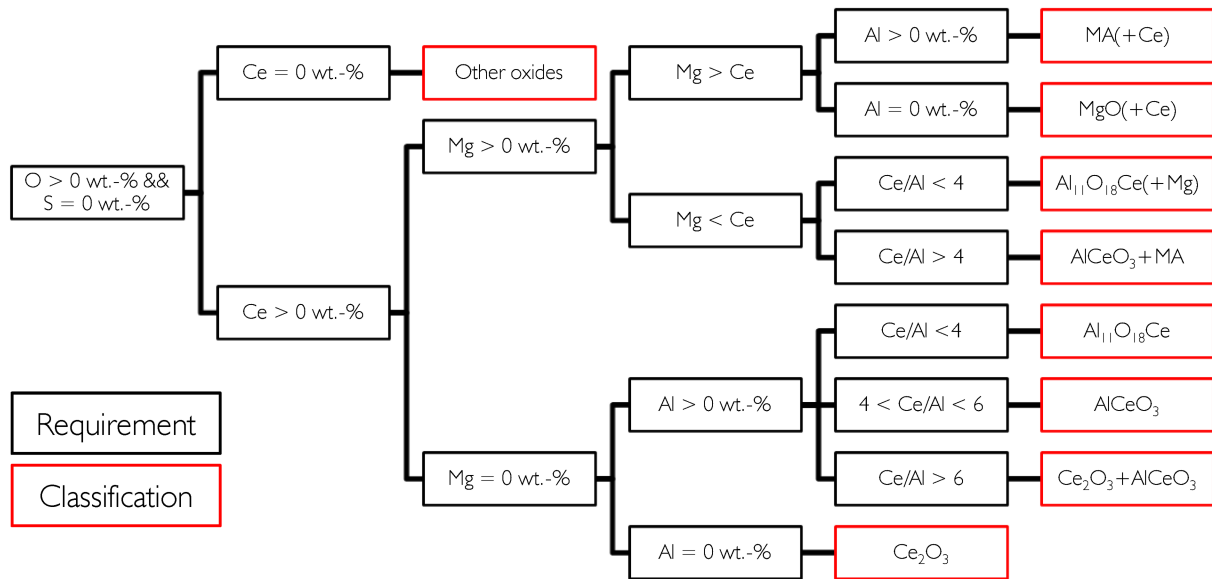
**Figure 4-12:** Particle classification of oxides for inclusion formation experiments with SASS

## SEM-EBSD measurements of the grain size in Gleeble samples

While it is possible to exceed the grain size via etching and light-microscopy for the Gleeble samples out of industrial SASS, the grain size of the gain refined specimens has to be measured with the help of the EBSD detector of the JEOL 7200F SEM. The examination is not possible without applying the EBSD detector, because the etching with V2A revealed the cast structure in the samples, before making the grain boundaries visible. The basic settings are given in **Table 4-2** and the selected phases for the measurement have been ferrite and austenite.

**Table 4-2:** Basic settings for EBSD measurements

| Acceleration voltage | Probe-current | Magnification | Binning | Frame time | Frame averaging | Step size |
|---|---|---|---|---|---|---|
| 20 keV | 13 | 200 | 4x4 | 24 ms | 1 | 1.2 μm |

The generated measurements can be analyzed with the tool "Tango" included in the "Channel 5" software package. It is applied to perform an automated analysis of the grain size via the line intercept method.

## 4.4 Summary of Experimental Procedures

The practical work of this thesis covers different forms of melting experiments and applies various metallographic methods.

- Small scale experiments are performed on a vertical-tube furnace. They include tests on the inclusion formation of Ce and Al in X1CrNiMoCuN20-19-7 and systematic variations of the cooling rate (1, 5 and 15 K/min) with the HS2-9-1-8.

- The other applied melting apparatus is a classic open hearth induction furnace. It is used to perform experiments with different casting parameters and inoculation tests with SASS and HSS.

- Light microscopy and photographs are used to evaluate the macrostructure of the as-cast ingots. The applied etchants are given in **Table 4-1**.

- With the help of secondary electron microscopy the carbide structure, the inclusion population and the grain size in the deformed Gleeble-samples is investigated.

# 5  X1CrNiMoCuN20-18-7 – *Experimental Results*

The super austenitic stainless steel X1CrNiMoCuN20-18-7 passes no phase transformation from solidification to room temperature. Therefore the grain refinement mechanism through phase transformation is not available and the primary grain size has greater importance for the microstructure at room temperature. This is discussed in more detail in section 2.4. The potential of a combined Al-Ce treatment for inoculation was already investigated in previous works, and AlCeO$_3$ was found to be a very promising particle to aid to heterogeneous nucleation [4]. This thesis aims to enlighten if the FToxid database included in FactSage is a reliable resource to forecast the inclusion population in the system SASS-Ce-Al-O. Studies in the system Fe-Ce-Al-O(-S) already pointed towards useful results [108]. Additionally, further grain refinement tests are performed to get a better understanding of the mechanisms and the importance of single experimental parameters. Lastly, to ensure that the smaller size prevails after deformation and recrystallization, tests with a Gleeble apparatus are conducted.

## 5.1  Formation of inclusions in the system SASS-Ce-Al-O

A Tammann-type furnace (=vertical tube furnace) is used to perform tests on inclusion formation of Ce, Al, and O in the SASS. The experimental setup is discussed in section 4.1.2. Three series with a varying initial oxygen content of 50, 80, and 110 ppm are conducted. Table 5-1 holds the chemical compositions. For all experiments the Al content ranges from 200-300 ppm, except for O-110-4 and O-110-5 where it is increased to 1000 ppm. Within every test series cerium is raised stepwise to picture as many different regions in the phase diagrams as possible.

Table 5-1: Chemical composition of inclusion formation experiments (detected with ICP-OES and LECO)

| Test | Ce [ppm] | Al [ppm] | O [ppm] |
|---|---|---|---|
| O-50-1 | 53 | 290 | 55 |
| O-50-2 | 230 | 290 | 62 |
| O-50-3 | 540 | 210 | 50 |
| O-80-1 | 93 | 180 | 90 |
| O-80-2 | 120 | 170 | 80 |
| O-80-3 | 500 | 330 | 84 |
| O-110-1 | 120 | 250 | 100 |

| Test | Ce [ppm] | Al [ppm] | O [ppm] |
|---|---|---|---|
| O-110-2 | 390 | 400 | 119 |
| O-110-3 | 460 | 350 | 115 |
| O-110-4 | 84 | 980 | 105 |
| O-110-5 | 310 | 960 | 119 |

**Figure 5-1** shows the phase diagrams calculated with FactSage 7.2 and the databases FToxid and FSmisc. The simulations are performed for 1545 °C as this is the holding temperature. The oxygen values are varied according to the content in the three-test series. It is evident that the stability regions are depending on the oxygen and especially the single-phase $AlCeO_3$ area is getting drastically smaller and moves towards higher Ce contents for Al values lower than 0.1 wt.-%. Every experiment is represented in the diagrams by a symbol.
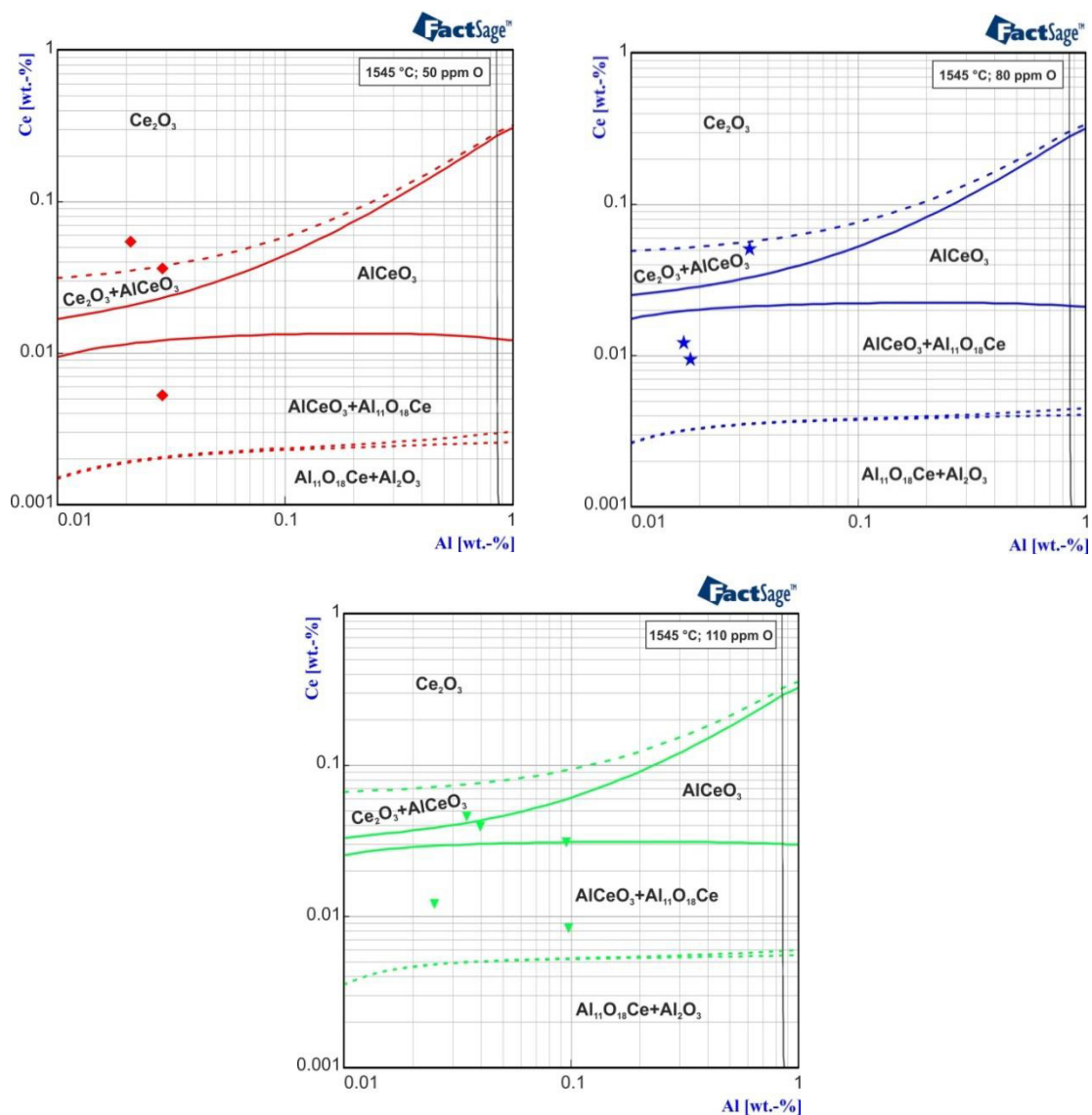


**Figure 5-1:** Ce-Al-phase diagram for SASS at 1545 °C with 50, 80 and 110 ppm of O (calculated with FactSage 7.2; FToxid and FTmisc databases)

The automated SEM-EDS feature measurement is the chosen instrument to evaluate the inclusion population in every sample. For more details on the classification, please refer to section 4.3.3 and the appendix. **Figure 5-2** shows exemplary particles for the homogeneous

$Ce_2O_3$, $AlCeO_3$, and $Al_{11}O_{18}Ce$. The latter can be easily differentiated from $AlCeO_3$ because of its grey value. Besides these, there also exists a heterogeneous form of $AlCeO_3+Ce_2O_3$. The example shows a NMI with a $Ce_2O_3$ core and a shell consisting of $AlCeO_3$, which is the most common type. Another possibility would be an interchange of the core and the shell phase, or there could also be a third layer on the outside. The classes $AlCeO_3$ and $AlCeO_3+Ce_2O_3$ are assumed to be active for grain refinement. The last inclusion shown in **Figure 5-2** is a MgO core with a (Mg, Al)O shell, as there is no Mg in the system in form of alloying elements or crucible material, this type must have its origin in the original production process. The second-to-last particle pictures one of these original inclusions with a seam of cerium at its edge.
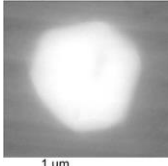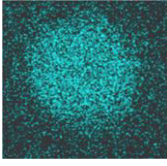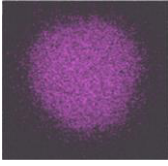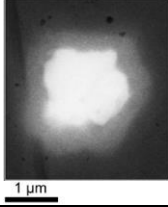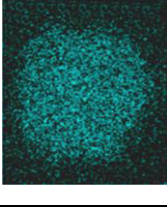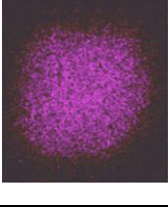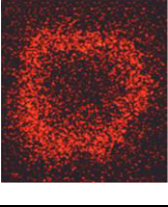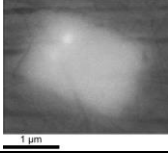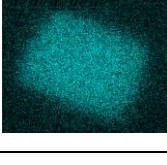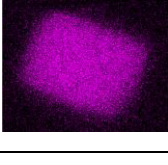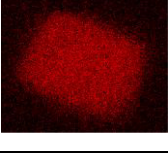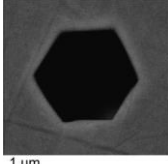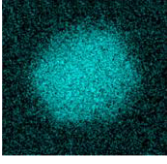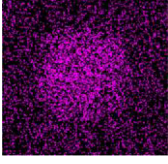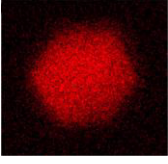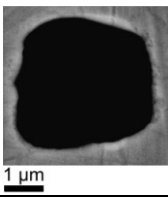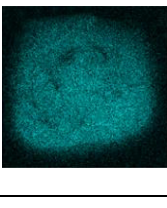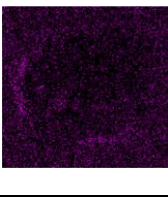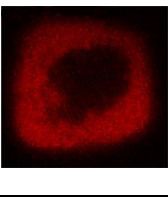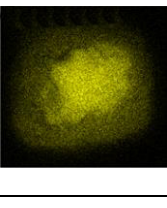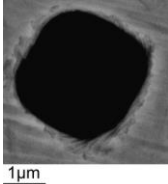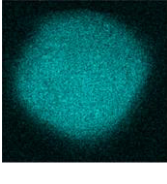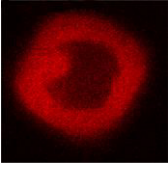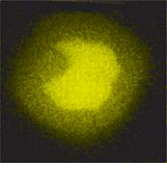
| Particle type | Electron pic. | O | Ce | Al | Mg |
|---|---|---|---|---|---|
| $Ce_2O_3$ | | | | | |
| $AlCeO_3+Ce_2O_3$ | | | | | |
| $AlCeO_3$ | | | | | |
| $Al_{11}O_{18}Ce$ | | | | | |
| MA(+Ce) | | | | | |
| Other Oxides | | | | | |

**Figure 5-2:** SEM phase mappings of oxidic particles

The oxidic particles are in very good correspondence with the phase diagrams calculated with FactSage. Additionally to these inclusions, there is also a considerable number of NMI containing oxygen and sulfur. It must be noted that the SASS has a high amount of molybdenum and thus the detection of sulfur is difficult because the characteristic K-alpha radiation of S (2.307 keV) is

remarkably similar to the L-alpha radiation of Mo (2.293 keV). Only when S surpasses a limit of 1 wt.-%, it is considered to be a compound of the NMI.

The formation of oxisulfides is not predicted by the equilibrium calculations performed with FactSage. Their existence can be explained by a local oversaturation of Ce during the dissolution in the melt. Then the fraction of Ce in the local melt could be high enough, that even the 4 ppm of sulfur contained in the SASS is enough to form $Ce_2O_2S$. A calculation with FactSage suggests that the local Ce content has to surpass a value of 0.25 wt.-% for $Ce_2O_2S$ to become stable (**Figure 5-3**).
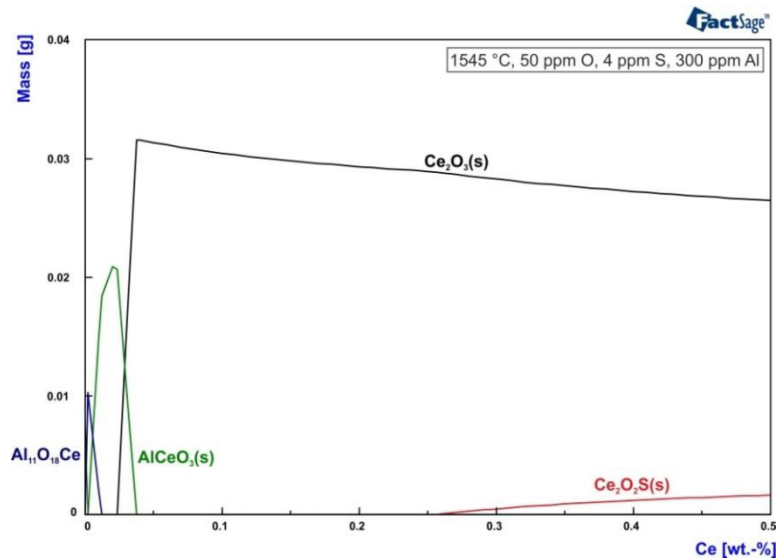


**Figure 5-3:** Cerium variation in SASS containing 50 ppm O, 4 ppm S and 300 ppm Al at 1545 °C (calculated with FactSage 7.2; FToxid, FTmisc and SGPS databases)

**Figure 5-4** shows examples for every type of particle containing both oxygen and sulfur. Similar to the oxides a homogeneous $Ce_2O_2S$ exists, but additionally mixtures of $Ce_2O_2S+Ce_2O_3$ or $Ce_2O_2S+AlCeO_3$ are possible. Beside those solid forms, an inclusion type denoted as "Ce low (+Al, S, O)" is also defined. They are perfectly round, which points towards the formation as liquid phase in the molten steel. This means this is a kind of slag phase with cerium that is not described in the thermodynamic databases available today.

| Particle type | Electron Pic. | O | S | Ce | Al |
|---|---|---|---|---|---|
| $Ce_2O_2S+Ce_2O_3$ |  | | | | |
| $Ce_2O_2S+AlCeO_3$ |  | | | | |

| Particle type | Electron Pic. | O | S | Ce | Al |
|---|---|---|---|---|---|
| $Ce_2O_2S$ |  1 µm |  |  |  | |
| Ce low (+Al, S, O) |  1 µm |  |  |  |  |
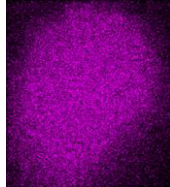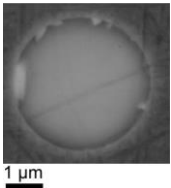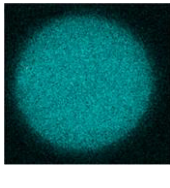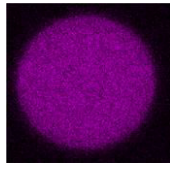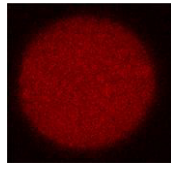
**Figure 5-4:** SEM phase mappings of oxisulfidic particles

**Selected results**

The samples taken 20 min after the addition represent the final results of the investigation. At 20 min a stable state regarding the chemical composition of the inclusions is reached, and only the number of inclusions is decreasing slightly, because of flotation effects. The initial state of the system, as found in P0, depends on the oxygen content. The number of particles increases from around 30 to 50 per mm², but the dominant type stays the same, namely (Mg, Al)O. A typical example is displayed in **Figure 5-5**.
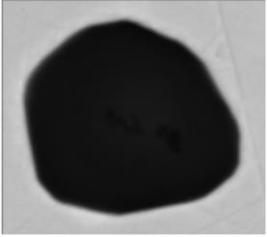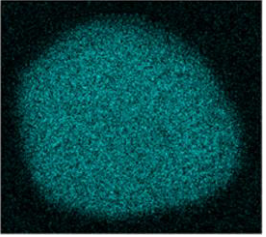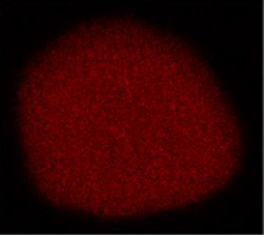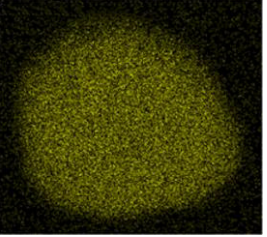
| Electron Pic. | O | Al | Mg |
|---|---|---|---|
|  5 µm |  |  |  |

**Figure 5-5:** SEM phase mapping of a typical (Mg, Al)O inclusion in P0

The experiments O-50-2, O-80-3 and O-110-3 all represent the $AlCeO_3+Ce_2O_3$ phase region, as can be seen in the phase diagrams in **Figure 5-1**. **Table 5-2** shows the chemical composition of the samples. If there are 62 ppm of oxygen in the system, already 230 ppm of Ce are enough to reach this phase area.

**Figure 5-6** represents the inclusion population in each test via the number of particles per mm². In the SASS the detection of the white cerium-containing NMI is a challenge, because the sigma-phase is brighter than the matrix, too. Thus it is impossible to exactly differentiate between sigma-phase and nonmetallic inclusions in the backscattering image only via the adjustment of grey value settings. The consideration of the sigma phase for the EDS analysis would, on the other hand, result in a skyrocketing of the required measuring time.

The most apparent difference in the particle populations displayed in **Figure 5-6** is the total number of particles. It is increasing with the rise of oxygen. The most prominent types in every test are $Ce_2O_3$ and $AlCeO_3+Ce_2O_3$, which correspond very well with the performed FactSage

calculation. The oxysulfide inclusions are additionally present in the samples. Most of them represent a mixture of $Ce_2O_2S$ and $Ce_2O_3$ or $AlCeO_3$. This means that also the oxysulfides reflect the equilibrium phase regions.

**Table 5-2:** Chemical composition of tests with varying O content in the $AlCeO_3+Ce_2O_3$ phase region

| Test | Ce [ppm] | Al [ppm] | O [ppm] |
|---|---|---|---|
| O-50-2 | 230 | 290 | 62 |
| O-80-3 | 500 | 330 | 84 |
| O-110-3 | 460 | 350 | 115 |
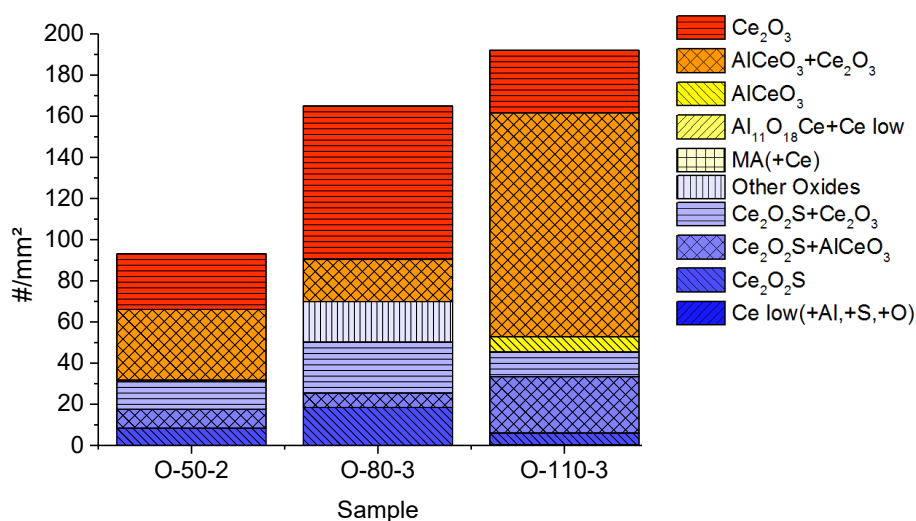


**Figure 5-6:** Influence of the oxygen content on the inclusion population in the $AlCeO_3+Ce_2O_3$ phase area

The next experiments that are discussed are those containing 50 ppm of O. According to their chemical composition and the phase diagram (**Figure 5-1**) they should represent the $AlCeO_3+Al_{11}O_{18}Ce$, $AlCeO_3+Ce_2O_3$, and $Ce_2O_3$ regions, in this order with increasing Ce content. Most inclusions in the test O-50-1 are $AlCeO_3$. $Al_{11}O_{18}Ce$ is not detected in vast amounts. The second most frequent particle type is "Other Oxides" which corresponds mostly to (Al, Mg)O. As explained above these NMI have their origin in the original production process, and the transformation to $Al_{11}O_{18}Ce$ is either thermodynamically or kinetically not favorable. O-50-2 is already discussed before. In O-50-3 the most common NMI are $Ce_2O_3$ and $Ce_2O_2S+Ce_2O_3$.

**Table 5-3:** Chemical composition of test series with 50 ppm O and varying Ce content

| Test | Ce [ppm] | Al [ppm] | O [ppm] |
|---|---|---|---|
| O-50-1 | 53 | 290 | 55 |
| O-50-2 | 230 | 290 | 62 |
| O-50-3 | 540 | 210 | 50 |
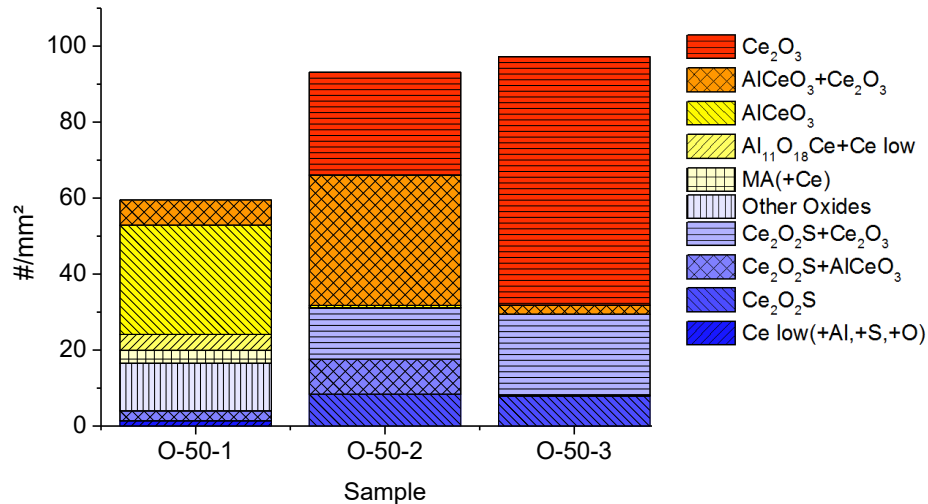
**Figure 5-7:** Influence of cerium content on the inclusion population at a total oxygen content of 50 ppm

The inclusion landscapes for both described sets of experiments give an excellent replica of the calculated phase regions. This is also true for the tests not discussed at this point, for their inclusion populations please refer to the appendix (**Figure 9-4** and **Figure 9-5**). The thermodynamic calculations with FactSage are a valid tool to forecast the inclusion landscape and it can be applied to design experiments and choose the right alloying amounts with the goal of $AlCeO_3$ formation.

## 5.2 Grain refinement of X1CrNiMoCuN20-18-7

To develop an advanced understanding of the processes and requirements to perform a successful grain refinement of the SASS, experiments with $AlCeO_3$ inoculation are conducted. They are divided into two test series and a reference ingot. While series A is cast with a temperature of approximately 1470 °C, series B is performed with a casting temperature of 1540 °C. In both of the two different kinds, cerium carriers are applied, pure metallic cerium and the commercial grain refining product "Elkem Grain Refiner – Grain seed" (=EGR), to verify if differences are occurring from the two inoculation materials. The chemical composition of EGR is given in **Table 5-4**, due to the high amounts of Si and Cr, oxidation during storage is prevented, which makes an industrial application of EGR easier than of metallic cerium. As mentioned in the experimental description material provided by vBEG is melted during the tests, thus the application of EGR is not ideal because the Si content is increased beyond the specification limits. In series A, the application of metallic Ce leads to a decrease in the total oxygen to 80 ppm. The other experiments all have oxygen contents near 140 ppm. The chemical analysis of the tests for Ce, Al and O are given in **Table 5-5** together with the applied grain refiner and the casting temperature. A more detailed chemical analysis is provided in the appendix. Four tests performed in series A are cast in molds preheated approximately to 400 °C.

**Table 5-4:** Chemical composition of EGR in wt.-%

| Si | Cr | Ce | C | Fe |
|------|------|------|-----|------|
| 19.5 | 34.6 | 10.3 | 0.1 | Bal. |

Table 5-5: Chemical composition of grain refinement experiments

| Test | Applied grain refiner | Casting temp. [°C] | Ce [ppm] | Al [ppm] | O [ppm] |
|---|---|---|---|---|---|
| Ref | none | 1540 | - | < 50 | 160 |
| A-E-1* | EGR+Al | 1470 | 320 | 60 | 140 |
| A-Ce-2* | Cer+Al | 1452 | 310 | 130 | 72 |
| A-E-3 | EGR+Al | 1473 | 210 | 70 | 130 |
| A-E-4* | EGR+Al | 1470 | 730 | 90 | 110 |
| A-Ce-5 | Cer+Al | 1468 | 310 | 140 | 78 |
| A-E-6* | EGR+Al | 1470 | 190 | 60 | 140 |
| A-Ce-7 | Cer+Al | 1456 | 1220 | 240 | 86 |
| B-Ce-1 | Cer+Al | 1531 | 180 | 130 | 130 |
| B-Ce-2 | Cer+Al | 1530 | 200 | 180 | 130 |
| B-E-3 | EGR+Al | 1546 | 90 | 190 | 120 |
| B-Ce-5 | Cer+Al | 1536 | 1080 | 220 | 170 |
| B-Ce-4 | Cer+Al | 1550 | 350 | 120 | 150 |

* preheated mold

## 5.2.1 Test series A – Casting temperature 1470 °C, 140 and 80 ppm O

For the evaluation of grain refinement, the columnar to equiaxed transition and grain density per unit area are functional parameters. **Table 5-6** gives an overview of the most important values. All of them are measured via metallographic methods, except for the amount of dissolved cerium, which is calculated at 1420 °C with FactSage. A successful inoculation should lead to a short columnar zone and a high grain density. The apparent difference between the macrostructures of the reference and the refined ingots is displayed in **Figure 5-8**.
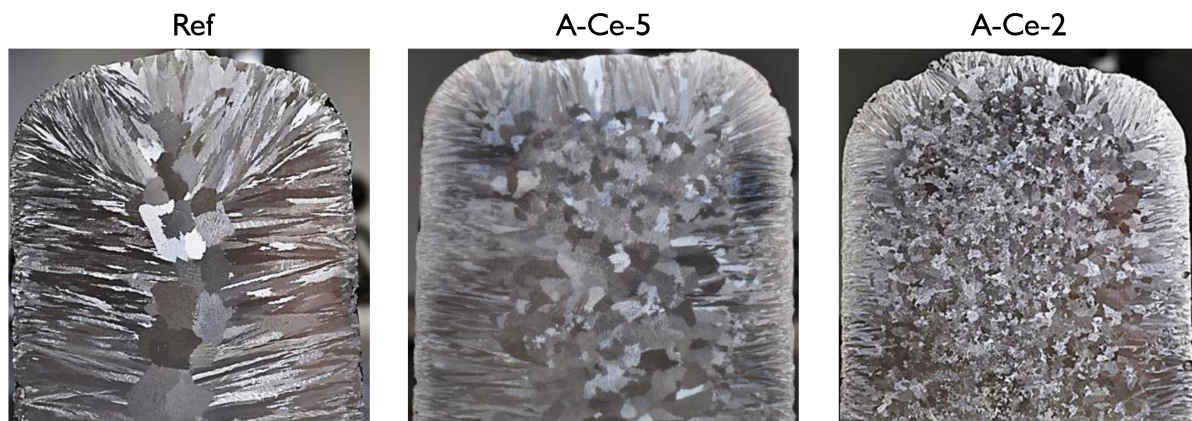


Figure 5-8: Examples for macrostructures with and without grain refinement – Series A

Table 5-6: Overview of the results regarding grain refinement – Series A

| Test | $R_{Eq}$ [1] | $N_{Gr}$ [1/cm²] | $d_A$ [mm] | N° of inclusions [1/mm²] | N° of AlCeO₃ [1/mm²] | Dissolved Ce@1420 °C [ppm] |
|---|---|---|---|---|---|---|
| Ref | 0.23 | 1.7 | 8.6 | 147 | 0 | 0 |
| A-E-1 | 0.64 | 41.3 | 1.7 | 320 | 36 | 0.552 |
| A-Ce-2 | 0.74 | 25.2 | 2.4 | 257 | 109 | 31 |
| A-E-3 | 0.57 | 21.1 | 2.2 | 207 | 44 | 0.028 |
| A-E-4 | 0.54 | 8.3 | 3.9 | 188 | 126 | 94 |
| A-Ce-5 | 0.57 | 6.1 | 4.5 | 334 | 152 | 33 |
| A-E-6 | 0.40 | 3.0 | 6.4 | 340 | 6 | 0.028 |
| A-Ce-7 | 0.20 | 1.3 | 9.8 | 670 | 0 | 729 |

It is essential to notice that the combined treatment with Ce and Al on the open hearth induction furnace is a challenge. The nearly infinite oxygen, that is available with this melting procedure, makes choosing the right alloying amount a delicate matter.

**Figure 5-9** gives the Ce/Al phase diagrams for SASS at 1470 °C with 80 and 140 ppm of O. The chemical compositions of the experiments are represented by dots. The color scale from green to red represents the outcome from very good grain refinement (green) to no change (red). When the chemical composition of the test lies within the Ce₂O₃ region or at the edge, there was no effect of the treatment. Most beneficial are cerium/aluminum contents that are near the AlCeO₃ area.
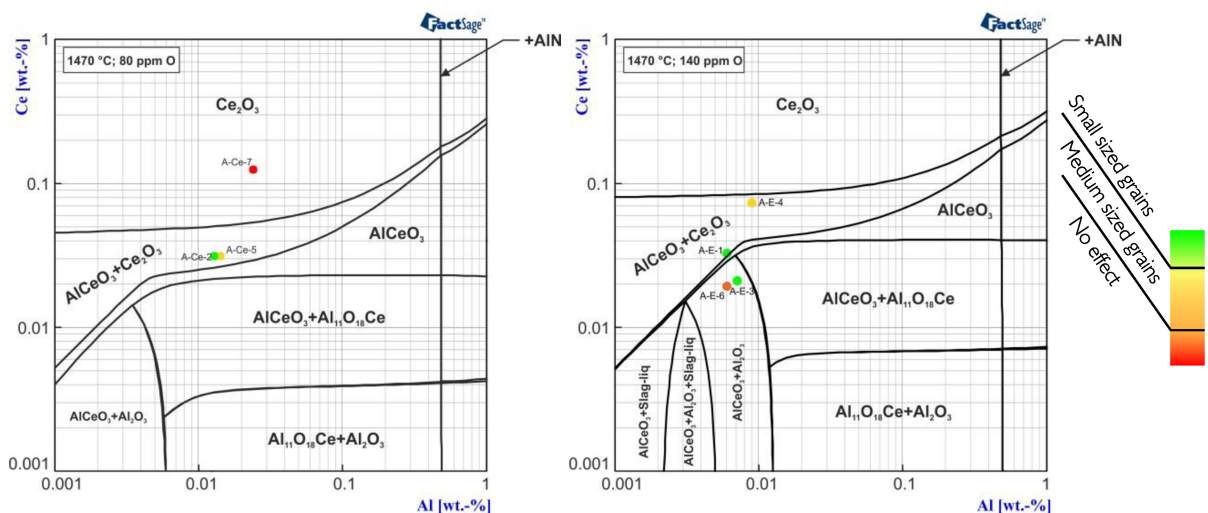


Figure 5-9: Ce/Al phase diagrams for SASS with 80 and 140 ppm O at 1470 °C (calculated with FactSage 7.2; FToxid and FTmisc databases)

The automated feature analysis is applied to these samples as well, and again, the reliability of the thermodynamic calculations is checked. Additionally to the NMI detected in the experiments on inclusion formation (refer to **Figure 5-2** and **Figure 5-4**) (Ce, Si)O particles are discovered. An example is given in **Figure 5-10**. They only appear in tests performed with the commercial grain refiner EGR, very likely due to the high silicon content of the product. The Ce-containing slag phase, that is already explained for oxisulfides above, does emerge in a purely oxidic form too and can also contain traces of Mn and Si (**Figure 5-11**).

| Electron Pic. | O | Ce | Si |
|---|---|---|---|
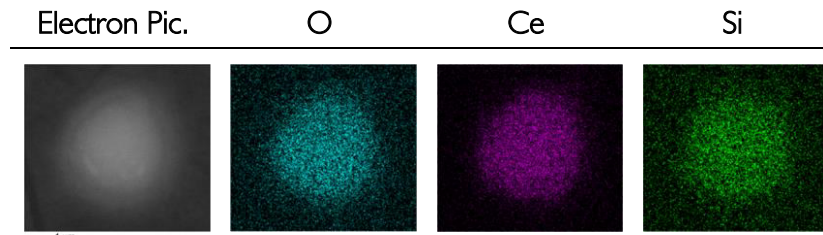


**Figure 5-10:** SEM phase mapping of (Ce, Si)O inclusion

| Electron Pic. | O | Ce | Al | Si | Mn |
|---|---|---|---|---|---|
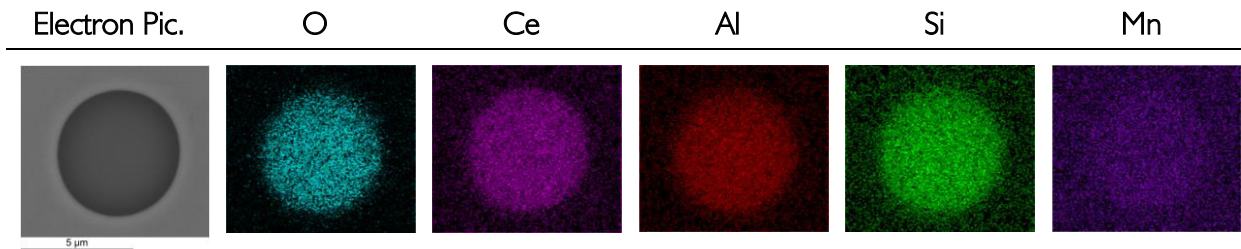


**Figure 5-11:** SEM phase mapping of oxidic slag phase containing Ce, Al, Si, and Mn

Inclusion populations, as measured with the automated feature analysis, are shown in **Figure 5-12**. The particles in test A-Ce-7 almost exclusively are $Ce_2O_3$, which corresponds perfectly with the phase diagram. Due to the masses of oxygen available at the open hearth induction furnace, the oxisulfides are negligible in comparison to the results of the vertical tube furnace. The experiments A-E-6 and A-E-3 both represent the $AlCeO_3$+$Al_2O_3$ phase region. The correspondence to the phase diagram is useful for A-E-3, but instead of $Al_2O_3$ inclusions, $Al_{11}O_{18}Ce$+Ce low is contained. A-E-6 deviates even further and shows (Ce, Si)O in place of $AlCeO_3$. The feature measurement of A-Ce-2 pictures the phase region of $AlCeO_3$+$Ce_2O_3$ very well. In reality the population is a result of over alloying, severe oxidation of Ce, and Al and separation of NMI between inoculation treatment and casting, it is a very dynamic and fast process. Thus it should be no surprise that the equilibrium phase diagram is not able to give a perfect picture of the inclusion landscape. Nonetheless, it is a useful tool to evaluate reasonable contents of Ce and Al and to make sure that the desired particles are even able to occur. The appendix holds the inclusion population for every experiment, together with other chosen parameters.
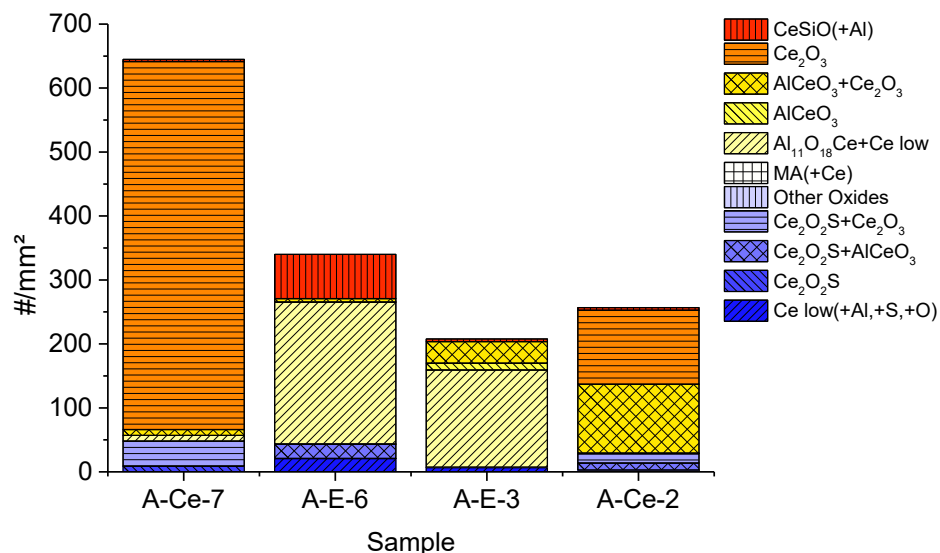


**Figure 5-12:** Inclusion populations of test series A

It seems obvious to assume that a higher amount of $AlCeO_3$ should reach better grain refinement because this implies that there are more potential nucleation sites available. But in the performed tests, an increased number of $AlCeO_3$ does not lead to improved results. **Figure 5-13** shows that while 40 $AlCeO_3/mm^2$ trigger the smallest grain sizes, more than 100 $AlCeO_3/mm^2$ do not decrease it further. But they still amend it compared to a sample without $AlCeO_3$ particles at all ($d_A = 6$ mm). What all tests with a high number of this inclusion have in common is an increased content of dissolved Ce. This could indicate that the NMI are not as active as nuclei as long as there is solute Ce in the melt.
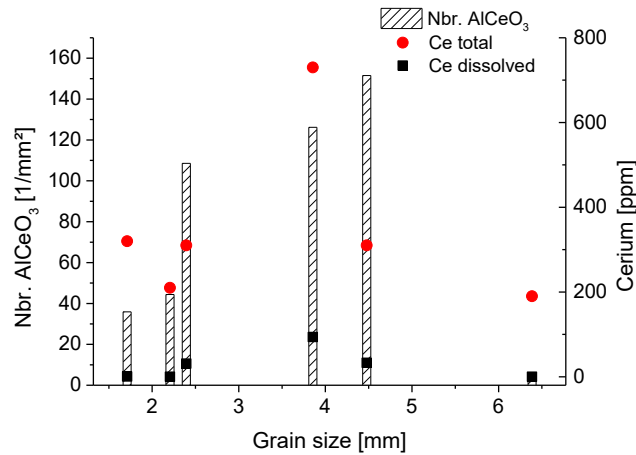


**Figure 5-13:** Grain size vs. number of $AlCeO_3$, total Ce and dissolved Ce content

## 5.2.2 Test series B – Casting temperature 1540 °C, 140 ppm O

In test series B the casting temperature is increased to 1540 °C, to investigate the effect of casting conditions on grain refinement. The CET and the grain size are not as drastically influenced as in series A. **Figure 5-14** compares two of the better macrostructures to the reference ingot. Test B-Ce-1 shows a clear improvement concerning the ratio of equiaxed solidification and also in regard to grain size. The difference between experiment B-E-3 and the reference is less distinct, but the equiaxed area is still 8 % larger. **Table 5-7** holds the exact results. The number of $AlCeO_3$ per unit area is much smaller than in the tests of series A, which is an issue of the difficult process control. With the higher casting temperature the alloy loss of cerium becomes nearly incontrollable and is too high in the cases of experiment B-Ce-1, B-Ce-2 and B-Ce-3 and too low in B-Ce-5 to ensure a favorable particle population.

| Ref | B-E-3 | B-Ce-1 |
|---|---|---|



**Figure 5-14:** Examples for macrostructures with and without grain refinement – Series B

**Table 5-7:** Overview of the results in regard to grain refinement – Series B

| Test | $R_{Eq}$ [1] | $N_{Gr}$ [1/cm²] | $d_A$ [mm] | N° of inclusions [1/mm²] | N° of AlCeO₃ [1/mm²] | Dissolved Ce@1420 °C [ppm] |
|------|------|------|------|------|------|------|
| Ref | 0.23 | 1.7 | 8.6 | 147 | 0 | 0 |
| B-Ce-1 | 0.46 | 3.2 | 6.2 | 185 | 9 | 0.076 |
| B-Ce-2 | 0.34 | 2.5 | 7.0 | 198 | 13 | 0.134 |
| B-E-3 | 0.31 | 1.7 | 8.5 | 165 | 6 | 0.138 |
| B-Ce-4 | 0.22 | 2.1 | 7.7 | 172 | 88 | 0.075 |
| B-Ce-5 | 0.16 | 3.1 | 6.2 | 700 | 0 | 94 |

**Figure 5-15** displays the phase diagram for 1540 °C and 140 ppm O. The mildly successful tests all are in the $AlCeO_3 + Al_{11}O_{18}Ce$ phase region. This stands in direct correlation with the low number of $AlCeO_3$ that are detected in these experiments.
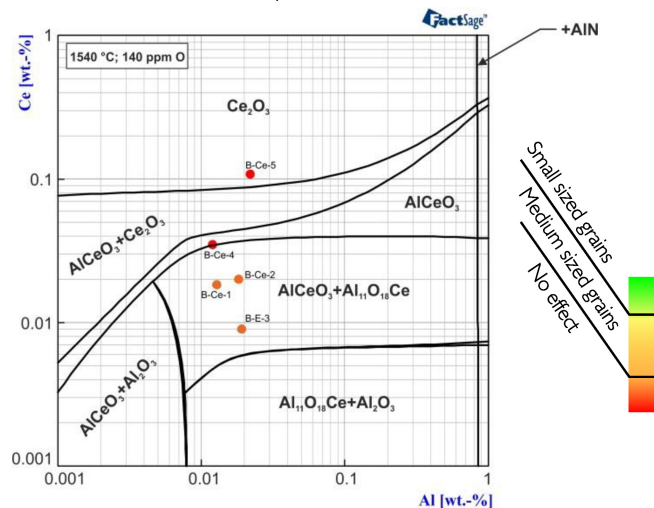


**Figure 5-15:** Ce/Al phase diagram for SASS with 140 ppm O at 1540 °C (calculated with FactSage 7.2; FToxid and FTmisc databases)

**Figure 5-16** displays the macrostructure of B-Ce-4. Surprisingly, there is no improvement visible because the test fulfills all the aforementioned requirements with regard to inclusion number and amount of dissolved Ce discussed for series A. A possible explanation lies within the casting conditions. The casting temperature is the highest of all experiments at 1550 °C and leads at the one hand to a very steep temperature gradient at the surface of the mold and thus to a very fast-growing columnar zone and on the other hand the overheating inside the melt is also increased, this makes nucleation more difficult. Both of which can prevent a successful grain refinement.



**Figure 5-16:** Macrostructure of test B-Ce-4

## 5.3 Deformation Experiments with a Gleeble Machine

The grain refinement of the as-cast structure brings improvements in regard to macro segregations and porosities, but the most significant benefit would lay within a permanent smaller grain size that results in optimized properties regarding strength and ductility. For materials undergoing hot deformation, the grain size is usually controlled by static and dynamic recrystallization and not by the as-cast primary grain size. The following deformation experiments are performed to evaluate if there is a potential for grain refined material to retain a smaller grain size even after deformation, recrystallization, and annealing. A Gleeble apparatus is used for these experiments to apply a defined amount of deformation and heat treatment.

Before starting the Gleeble experiments with the inoculated steel, the parameters are tested with industrial material in a re-annealed state with enlarged grains. This is necessary because there are only a limited number of refined samples available. As mentioned in section 4.2, different holding times at 1100 °C are applied. Recrystallization and 60 s at this temperature lead to a mean grain size of 66 µm, increasing the period at 1100 °C to 3600 s leads to growth and a final measure of 182 µm. The connection of holding time and size is pictured in **Figure 5-17**, and **Figure 5-18** contains exemplary images of the inspected grain structures after 60, 600, and 3600 s.
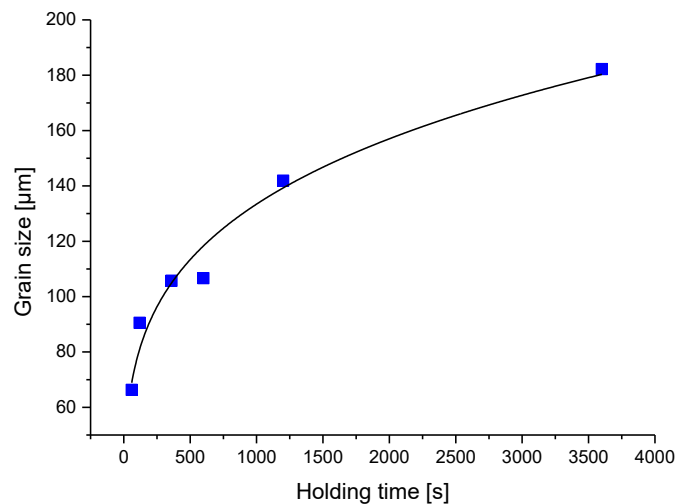


**Figure 5-17:** Grain growth of deformed and recrystallized industrial material at 1100 °C
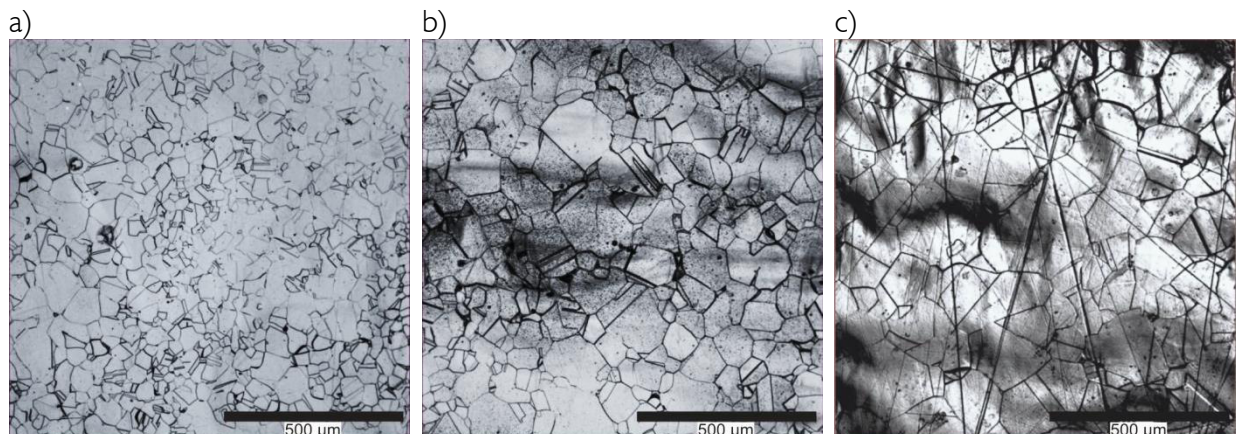


**Figure 5-18:** V2A etched images of grain structure in deformed and recrystallized industrial material after different holding times at 1100 °C; a) 60 s; b) 600 s; c) 3600 s

With the same parameters as for the industrial steel, deformation and recrystallization experiments are performed with inoculated material. The grain size measurements of these samples are conducted with an EBSD detector. For the reason of comparability, the equivalent industrial samples are additionally measured via the same method. **Figure 5-19** displays the sizes for both steels. It is evident that the grain growth of the refined material is restricted and much smaller than that of the industrial.
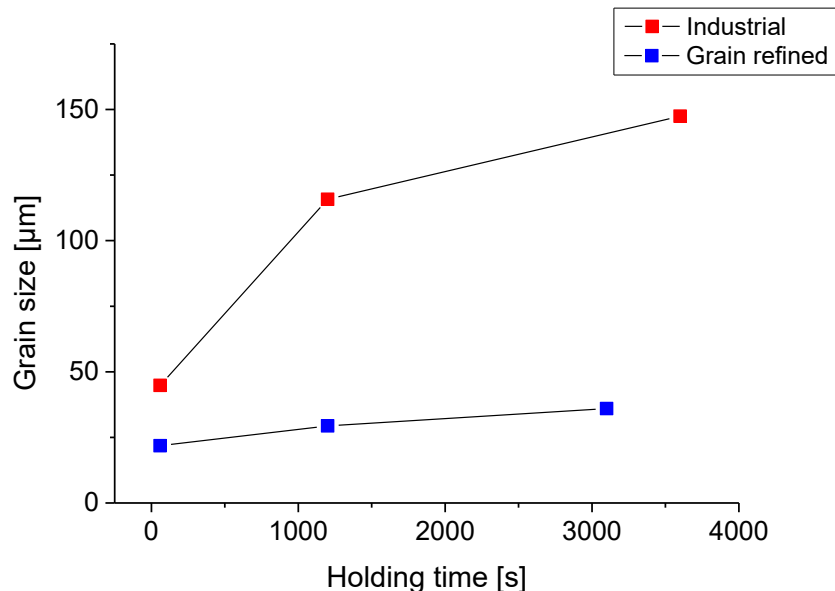


**Figure 5-19:** Grain growth of industrial vs. grain refined material measured by EBSD

Actual images of the grain structures in both steels after a holding time of 1200 s at 1100 °C are pictured in **Figure 5-20**. On the left side is the industrial and on the right the refined material. The latter exhibits a grain structure much smaller than in the industrial steel. This could be a result of a sort of pinning effect due to oxides precipitated at a later time during solidification or of the smaller initial grain size. Besides, it has to be noted that the grains have rather inhomogeneous sizes in the grain refined material. Larger grains are interrupted by bands of smaller ones. When observing the material with the backscattered electron contrast of the SEM (**Figure 5-21**), it becomes clear that the sigma-phase (white), that has its origin in the solidification process, is still present. The different shades of grey in the image are an effect of the applied OPS-polishing and not of different phases in the material. It reveals the grain structure and twinning boundaries to some extent, even with the backscattering detector. The heat treatment and deformation in the Gleeble experiment are not sufficient enough to dissolve the sigma-phase. The bands of smaller grain size manifest themselves exactly around it.

**200 µm**          **200 µm**
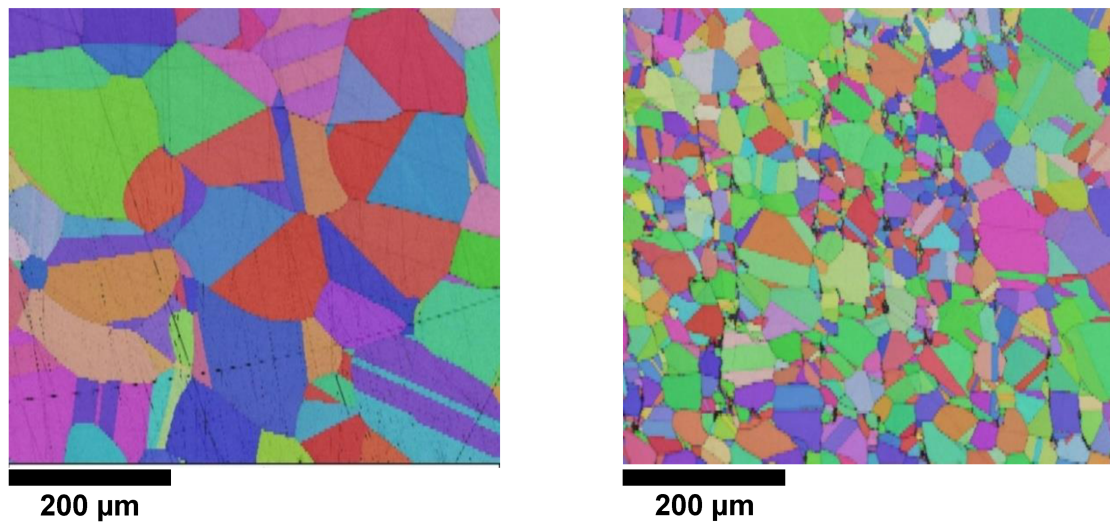
**Figure 5-20:** Grain structure after 1200 s at 1100 °C
(left – industrial; right – grain refined)



100 µm          10 µm
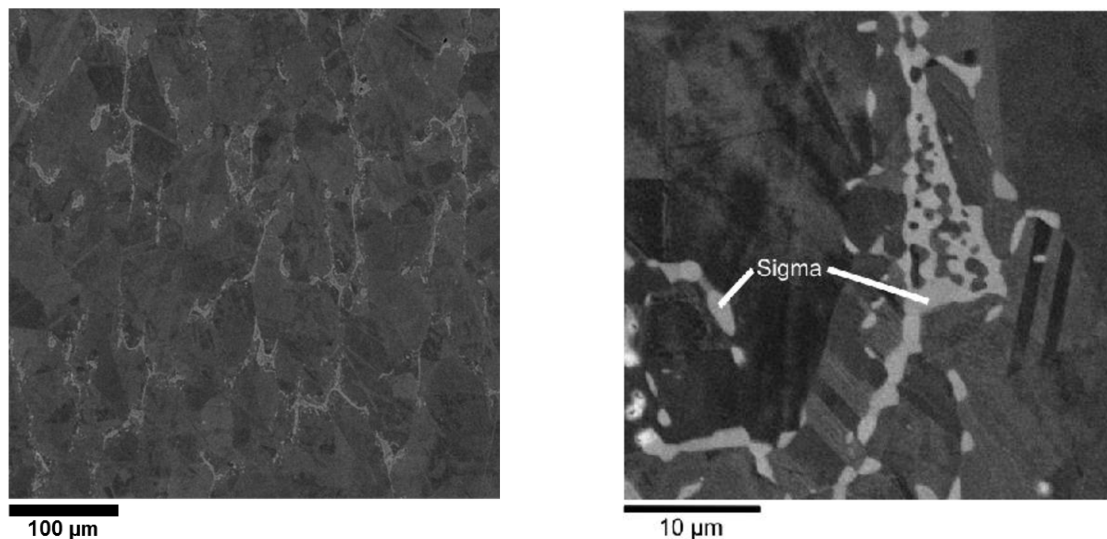
**Figure 5-21:** Electron contrast of refined material after Gleeble experiment,
(left – overview; right – detail, sigma-phase)

It is a promising result that the larger grains in between the sigma-phase in the inoculated steel do not grow at the same extent as those in the industrial material. To enlighten the exact reason, more investigations would be necessary. The smaller grains in the refined material constitute an advantage in comparison to the enlarged grains in industrial steel. Therefore the toughness and ductility of the inoculated material should be improved. At which extent the still existent chemical inhomogeneity contributes to retaining the smaller grain size cannot be answered with the available data, but this is also not the focus of this thesis which lay primarily on the possibilities to influence the as-cast structure.

## 5.4 Summary of Experimental Findings for X1CrNiMoCuN20-18-7

The experimental results and highlights concerning X1CrNiMoCuN20-18-7 are summarized in the following points. Especially the interaction between the two types of melting experiments is enlightened.

**Investigations on inclusions: Thermodynamics and experiments**

The survey on previously published literature indicates that the application of cerium improves the macrostructure of austenitic steel grades. Depending on the first solidifying phase this effect is attributed to various cerium inclusions, e.g., to $CeO_2$ and $AlCeO_3$ for austenitic manganese steels. A previous study conducted at the Chair of Ferrous Metallurgy also suggested a high potential for the application of $AlCeO_3$ for the grain refinement of X1CrNIMoCuN20-18-7. Thus the current thesis wants to enlighten the formation and application of $AlCeO_3$ for grain refinement in greater detail.

In a first step, the significance of the results of thermodynamic calculations with FactSage and the database FToxid are verified by extensive laboratory experiments. Therefore the formation of cerium-aluminum inclusions in pure iron was investigated in the course of a master thesis, followed by eleven tests with the SASS in this thesis to include the influence of the steel grade.

The test results show that a vast amount of different NMI can form in the system SASS-Al-Ce-O:

- $AlCeO_3$ and the mixture of $AlCeO_3 + Ce_2O_3$ are regarded as active for grain refinement.
- $Ce_2O_3$ and $Al_{11}O_{18}Ce$ occur as expected from the thermodynamic simulation.
- Additionally, the dissolution of Ce leads to the formation of $Ce_2O_2S$ and mixtures of $Ce_2O_2S$ and oxides even at the very low S levels in the SASS during cooling and solidification.

Although the databases for such highly alloyed steels and cerium-inclusions surely are not perfect, they provide a solid basis to perform simulations on the inclusion formation of $AlCeO_3$. The experiments conducted in the controlled argon atmosphere show an ideal correspondence for the thermodynamic calculations performed with FactSage.

As established in the grain refinement experiments, a high number of $AlCeO_3$ simultaneously with a low content of dissolved Ce leads to the best results. Both of these criterions can be applied to these tests. In **Figure 5-22** and **Figure 5-23** every performed experiment is represented by a dot in a Ce vs. Al plot. The size of the circles is proportional to the number of $AlCeO_3$ and respectively to the content of dissolved cerium. Favorable amounts of Ce and Al can be distinguished between 40 and 350 ppm of cerium and less than 400 ppm aluminum. The oxygen content always has to be taken under account, because the exact position of the phase regions depends on it. It is not necessary to accurately hit the $AlCeO_3$ stability area to generate a beneficial inclusion population, even the fields surrounding it lead to a sufficient amount of $AlCeO_3$. Cerium contents in the $Ce_2O_3$ stability region have to be avoided.

Higher Al contents theoretically also result in $AlCeO_3$ and low content of solute Ce, but in reality, the precipitated inclusions are often inhomogeneous and corrupted and therefore could be unavailable to perform as nucleation sites.
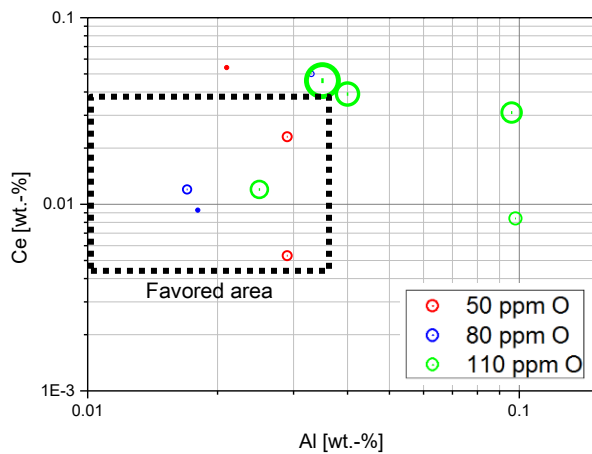


**Figure 5-22:** Number of $AlCeO_3$/mm² depending on the position in the Ce-Al-O phase diagram
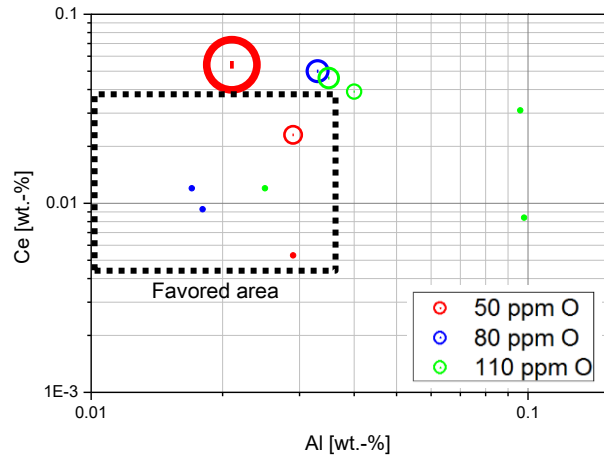
**Figure 5-23:** Amount of dissolved Ce depending on the position in the Ce-Al-O phase diagram

## Grain refinement tests

After proofing the applicability of the thermodynamic calculations for the simulation of cerium-inclusions in the SASS, the next step is to investigate the potential for grain refinement of particular particle populations. The thermodynamic simulations with FactSage are less applicable for the tests at the induction furnace. The steel melt in the furnace cannot be protected from reactions with oxygen from the air. This results in an immediate reoxidation of the steel after the addition of Al and Ce (or grain refiner). The exact adjustment of the Ce- and Al-content is thus difficult, but also the precise alignment of the inclusion composition. But even under these unfavorable conditions, it is possible to choose promising combinations of Ce and Al, but the reproducibility is limited. An additional need is the definition of a standardized casting procedure, namely the definition of a holding time between the addition of Ce and Al and the casting of the ingot.

**Figure 5-24** displays the number of equiaxed grains as a function of the ratio of equiaxed solidification. Thus it gives a good overview of all experimental outcomes in test series A and B. Based on this diagram the influence of the number of $AlCeO_3$ inclusions, oxygen content, casting temperature, preheating of the mold and application of EGR or metallic cerium shall be discussed.
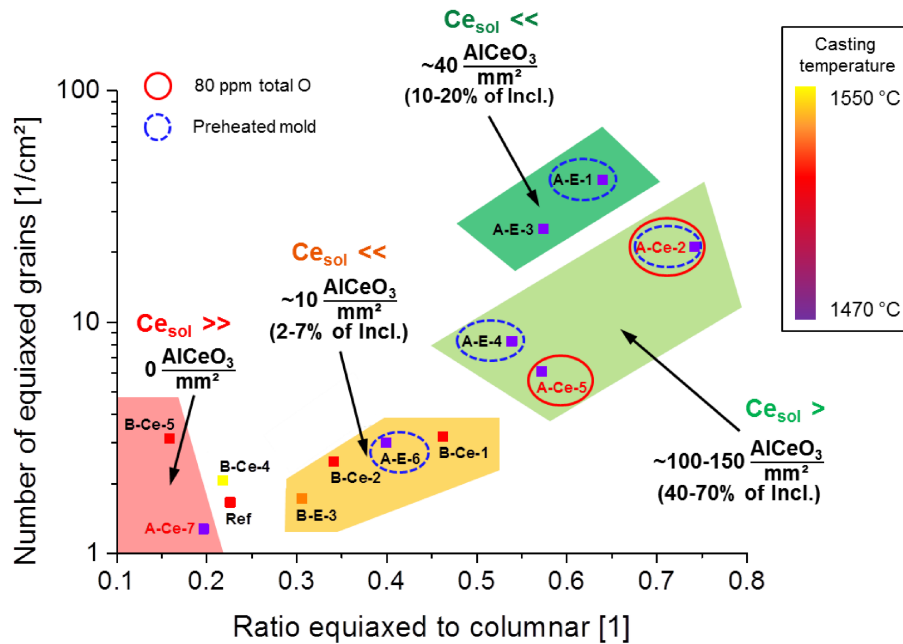
**Figure 5-24:** Overview of the experimental results on grain refinement of SASS

- **Number of AlCeO$_3$ and content of dissolved Ce**

The number of AlCeO$_3$ is the most critical factor influencing the outcome in regard to grain refinement. The experiments are grouped according to the number of AlCeO$_3$ inclusions.

The smallest grain sizes are reached by the tests in the dark green area in **Figure 5-24** with around 40 AlCeO$_3$/mm$^2$ that make up 10-20 % of all NMI present in the samples.

In the light green area, the ratio of equiaxed to columnar solidification is also adequate and the particle number is higher than 100 AlCeO$_3$/mm$^2$. Simultaneously the content of dissolved Ce is increasing. It is assumed that it either alters the inclusions and inhibits them from becoming active nuclei or it is promoting grain growth in its dissolved form, which opposes different publications that propose a positive effect of solute Ce on grain refinement.

In the orange area in **Figure 5-24** AlCeO$_3$ decrease to 10 per mm$^2$. There is still a measurable improvement compared to the reference, but a higher number would be more desirable.

The content of Ce in the red zone surpasses the boundary for AlCeO$_3$ formation. Thus only Ce$_2$O$_3$ is contained. This leads to a macrostructure even worse than the reference. Besides the wrong population of particles, also the amount of dissolved Ce is high, which indicates again that dissolved Ce does not contribute to grain refinement, at least in this specific steel grade.

- **Total oxygen content**

While the mean total oxygen content in most of the tests is approx. 140 ppm, the experiments treated with metallic Ce in series A contain only 80 ppm. The red circles in **Figure 5-24** indicate the mentioned tests. For industrial applications, it is an advantage, that already 80 ppm lead to such an improvement because the usual request for low oxygen contents can be met and simultaneously inoculation through heterogeneous nucleation is possible.

- Casting temperature

The casting temperature is varied between 1470 and 1550 °C. The symbols of the tests in **Figure 5-24** give an estimated value for the casting temperature due to their color. Overall higher casting temperatures lead to worse results, but this is primarily an effect of the hard to control cerium alloying at elevated temperatures and only secondarily of the casting condition itself. But if the casting temperature surpasses a certain limit, the solidification process becomes so disadvantageous that even the most promising inclusion population does not lead to grain refinement, as discussed for test B-Ce-4.

- Preheating of mold

The tests performed with preheated molds are indicated in **Figure 5-24** through dotted blue circles. It seems that with the right inclusion population, the results can be improved by preheating. But when the particle landscape is not ideal, like for test A-E-6, even the preheated mold cannot enhance the macrostructure significantly.

- Application of EGR vs. metallic cerium

Regarding the success in grain refinement, there is no significant difference between the use of EGR or Ce. In the experimental setup, where the chemical composition of the melt cannot be adjusted to consider the significant amount of Si alloyed via EGR, the application of metallic Ce has the advantage that the specification limit for Si is not crossed. Another effect observable with the application of EGR is the formation of CeSiO, that has no effect as a nucleation site but consumes a vast amount of cerium which otherwise could be used to form $AlCeO_3$.

**Deformation and recrystallization experiments**

The comparison of industrial and refined material after a certain deformation and varying annealing times show a significantly slower grain growth of the latter. This indicates that the original grain size or a pinning effect by oxides precipitated after solidification contributes to the grain size even after deformation and recrystallization. The smaller grains in the refined material constitute an advantage in comparison to the enlarged grains in industrial steel. Therefore the toughness and ductility of the inoculated material should be improved. The chemical imbalances resulting out of the cast-structure cannot be dissolved by the applied temperature and deformation in the Gleeble experiment. Thus further investigations are necessary to gain a more distinct result.

# 6  HS2-9-1-8 – *Experimental results*

The high-speed steel HS2-9-1-8 is a tool steel for very demanding applications. As discussed in section 2.4, the solidification structure is characterized by the eutectic precipitation of a vast amount of $M_2C$ carbides. The main objective in this thesis is to investigate if the size of these carbides can be refined either by the solidification parameters or by the application of grain refinement. To study how different parameters like the casting temperature or the cooling rate influence the carbide precipitation, two types of tests are performed: First is the small-scale experiment on the impact of cooling conditions in the Tammann-type furnace and second the variation of casting temperatures (superheat) on the induction furnace. Additionally, the opportunity to examine an industrial ingot is used to allow a comparison with the solidification structure of the test ingots. Last, experiments on the influence of grain refinement on the primary carbides are conducted.

## 6.1  Effect of cooling rate on the carbide structure of HS2-9-1-8

A significant influence of the cooling rate on the carbide type and morphology is well established and thoroughly investigated for many standard HSS types, but not for HS2-9-1-8. Under standard casting conditions, the eutectic carbide that is precipitated is $M_2C$. The present study enlightens the influence of cooling rate (1, 5, 15 K/min) on the microstructure of HS2-9-1-8 experimentally in the Tammann-type furnace. The aim is to illustrate the influence of the cooling rate on the type and size of the eutectic carbides. A mass of 300 g is used, which is not sufficient to conclude the solidification macro-structure, but it is enough to evaluate the relationship between carbide types, size, and cooling rate in more detail. The retained regulus is cut in half, and then $\lambda_2$ measurements and the investigation of carbide structure via SEM takes places on the planar surface in the center of the specimen. Equation (10) gives the relationship between $\lambda_2$, cooling rate, and local solidification time. The measured $\lambda_2$ are correlated with the respective cooling rates. Numerical methods are applied to find values for k=23.44 and n=0.359. The liquidus temperature of 1381 °C is determined through DTA-measurements, and the solidus temperature of 1212 °C originates from a FactSage calculation. The final version of the equation is given below.

$$\lambda_2 = k \left( \frac{T_L - T_S}{\dot{T}} \right)^n = 23.44 \left( \frac{1381 - 1212}{\dot{T}} \right)^{0.359} = 23.44 \cdot t_f^{0.359} \qquad (25)$$

Table 6-1 holds an overview of the results. The cooling rate is defined through furnace control, the secondary dendrite spacing is measured via light microscopy, and the local solidification time is

calculated according to equation (25). The lowest cooling rate (1 K/min) results in the highest $\lambda_2$ of 147.3 µm, and 15 K/min leads to 55.7 µm. **Figure 6-1** and **Figure 6-2** picture the graphical version of these results. The nature of equation (25) leads to drastic changes in the cooling rate for $\lambda_2 < 55.7$ µm, this is indicated through the black graph in **Figure 6-1**.

Table 6-1: Determined values for $\dot{T}$, $\lambda_2$ and $t_f$

| $\dot{T}$ [K/min] | 1 | 5 | 15 |
|---|---|---|---|
| $\lambda_2$ [µm] | 147.3 | 70.2 | 55.7 |
| Std. dev. $\lambda_2$ [µm] | 31.7 | 13.2 | 10.3 |
| $t_f$ [min] | 168.3 | 21.3 | 11.2 |
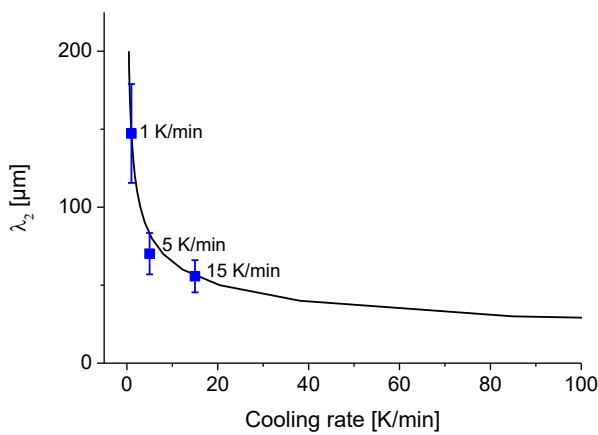


Figure 6-1: $\lambda_2$ vs. cooling rate
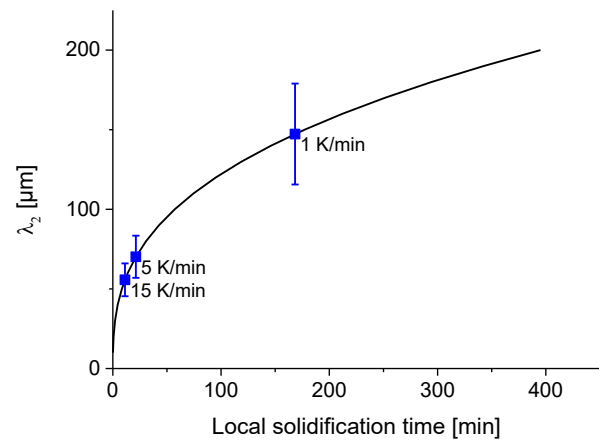


Figure 6-2: $\lambda_2$ vs. local solidification time

The next step in the evaluation of these experiments is the investigation of the carbides via high-resolution electron images captured with a SEM. Exemplary pictures are given in **Figure 6-3**. The first step of the image analysis is the marking of the whole carbide area, detectable by its different grey value (blue area). Next, carbides thicker than 1.2 µm are automatically colored in green. The areas can be measured and used to calculate the total carbide area and the ratio of coarse carbides. For 5 and 15 K/min, the morphology of the carbides remains the same, and in the metallographic evaluation, only $M_2C$ carbides are detected (**Figure 6-3**). Cooling of the sample with 1 K/min leads to the typical fishbone like morphology of $M_6C$. An area ratio of 70.7 % $M_6C$ is estimated with the help of element phase mappings. The result is given in **Table 6-2**.

Table 6-2: Area ratios of carbide types at varying cooling rates

| Cooling rate [K/min] | $M_2C$ [%] | $M_6C$ [%] | MC [%] |
|---|---|---|---|
| 1 | 28.8 | 70.7 | 0.5 |
| 5 | 100 | | |
| 15 | 100 | | |

$\dot{T}$ = 1 K/min

$\dot{T}$ = 5 K/min

$\dot{T}$ = 15 K/min
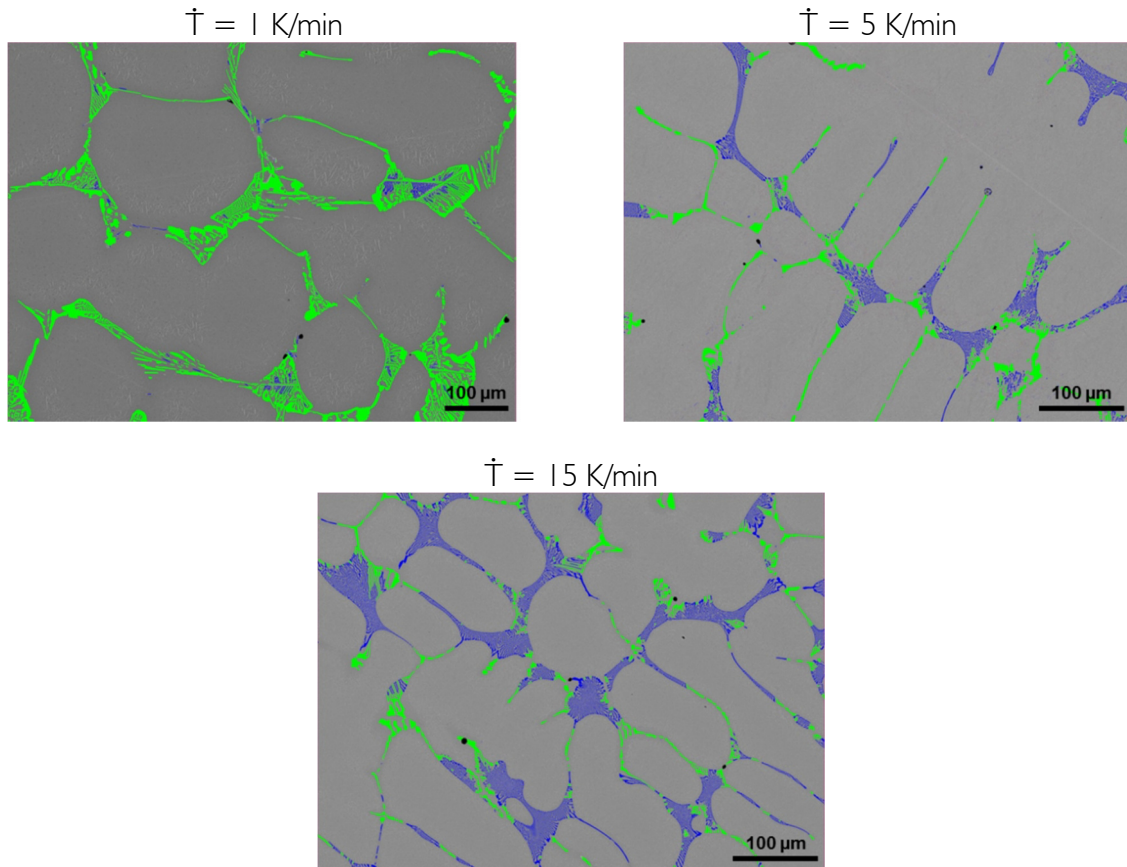


**Figure 6-3:** Image analysis of electron images at different cooling rates
(blue – total carbide area; green – area of coarse carbides thicker 1.2 μm)

Besides $M_2C$ and $M_6C$ also eutectic MC is detected, but due to its color, it is difficult to distinguish from the matrix. **Figure 6-4** shows an example of dark grey MC carbide, surrounded by matrix, $M_2C$ plates, and also $M_6C$. Typically for MC, the dominant elements are vanadium and carbon. In $M_2C$ molybdenum is the brightest element and $M_6C$ has the most tungsten, and Mo and V are depleted in these zones.



C          V          Mo          W
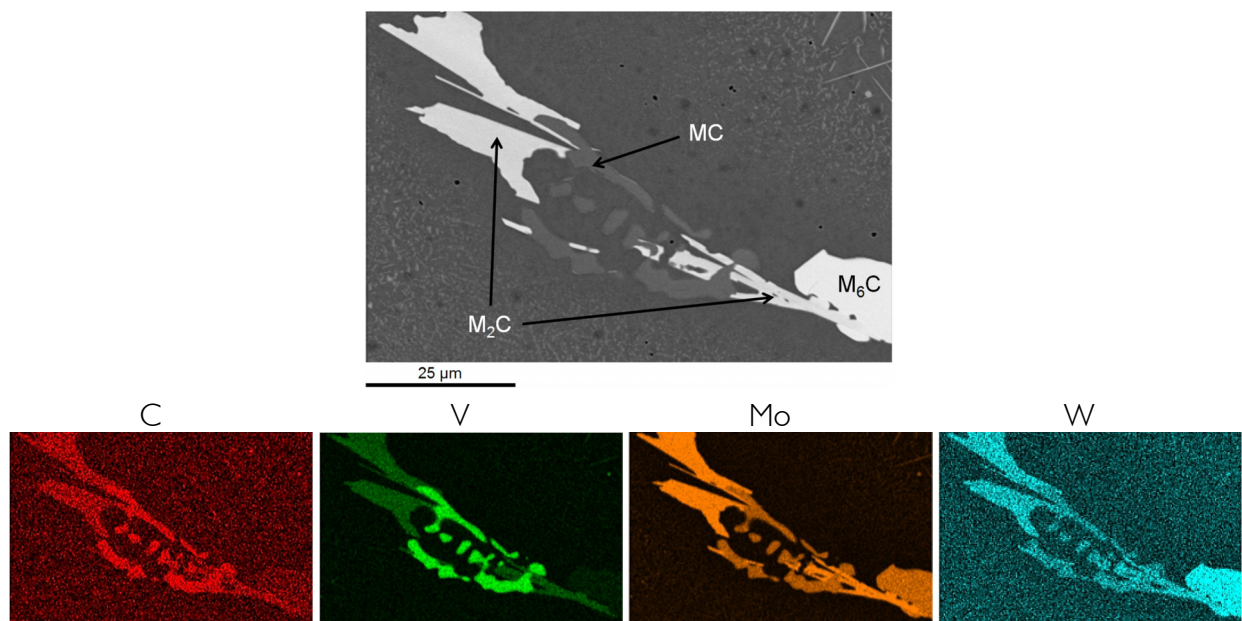
**Figure 6-4:** Eutectic MC carbide at $\dot{T}$=1 K/min

The total carbide content varies within the standard deviation between 6 and 8 % (**Figure 6-5**). This could be an effect of the cooling rate, but it seems more likely that alloy losses during the remelting play a more critical role. Especially V and Mo are affected, with losses up to 0.5 wt.-%. In **Figure 6-3** it is evident that the amount of green areas that represent the coarse carbides increases significantly with slower cooling rates. **Figure 6-6** pictures the ratio of carbide areas with a thickness greater than 1.2 µm. For 1 K/min, the ratio is as high as 96 % of the total carbide area and decreases to 47 % for 15 K/min.
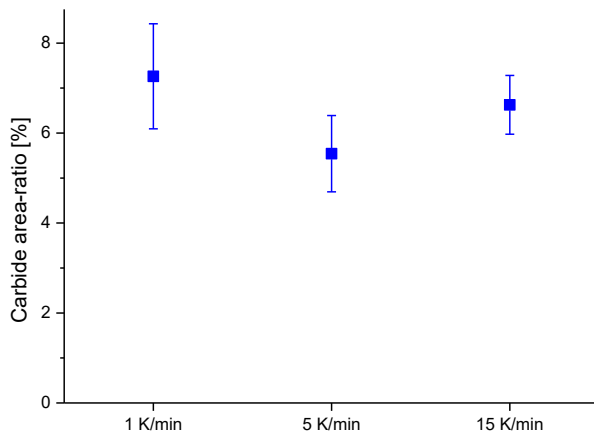


Figure 6-5: Area ratios of total carbide content at varying cooling rates
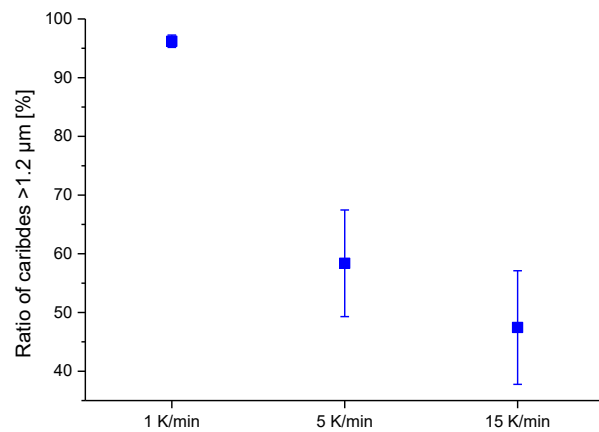


Figure 6-6: Ratio of coarse carbides at varying cooling rates

## 6.2 Effect of casting conditions on the solidification of HS2-9-1-8

The casting temperature (=CT) is a key parameter for the solidification of an ingot. An increased CT favors columnar solidification, as the temperature gradient in front of the dendrite tips gets steeper and the nucleation of equiaxed grains is prevented. To improve the knowledge of the influence of casting conditions on the macro- and carbide-structure of HSS, casting experiments on the open hearth IF are performed. Before the experiments are conducted, simulations with calcosoft-2D were performed to develop an advanced understanding of the solidification process. Thermocouples in the wall of the mold are used to document solidification and then inverse methods are applied to calculate the local solidification time over the cross-section of the ingot. The results are extrapolated to other casting temperatures and show that an increase of casting temperature from 1500 to 1650 °C leads to a change in the cooling rate in the ingot center from 55 K/min to 49 K/min. Based on these results four experiments with the HSS are performed, where the casting temperature is varied from 1500 to 1650 °C in steps of 50 °C. **Figure 6-7** shows how the macrostructure of the gained ingots changes. While the CET is near the surface for 1500 and 1550 °C, it moves farther to the ingot center for 1600 and 1650 °C. Limitations in the proper control of the experiment (e.g. asymmetrical filling of the mold) might influence this result. The ratio of directional solidification is given in **Figure 6-8**. It shows an increase from 15 to 35 % of the cross-section.
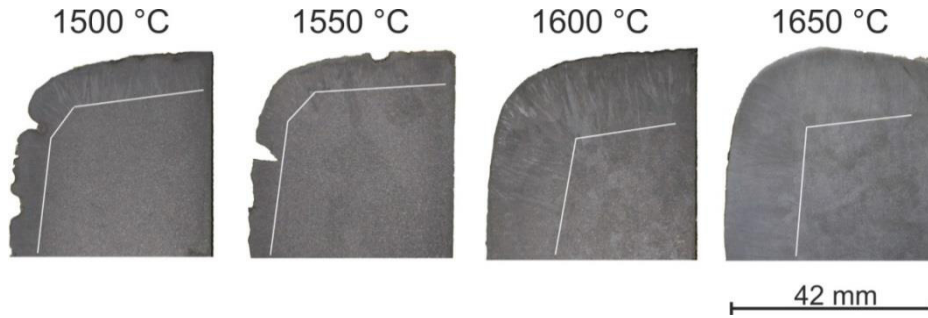
**Figure 6-7:** Macroetchings of HSS cast at varying temperatures
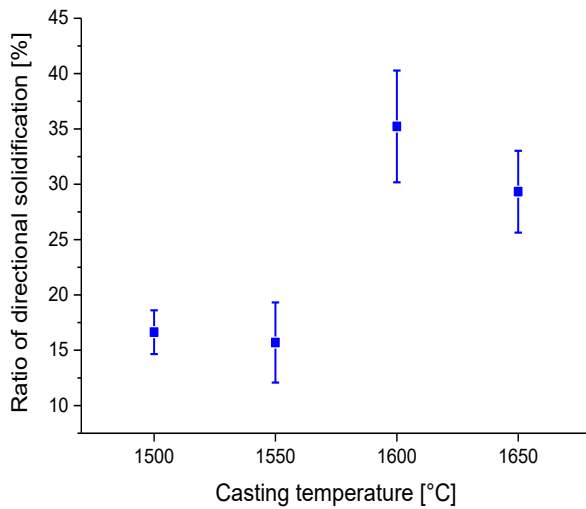


**Figure 6-8:** Ratio of directional solidification at varying casting temperatures
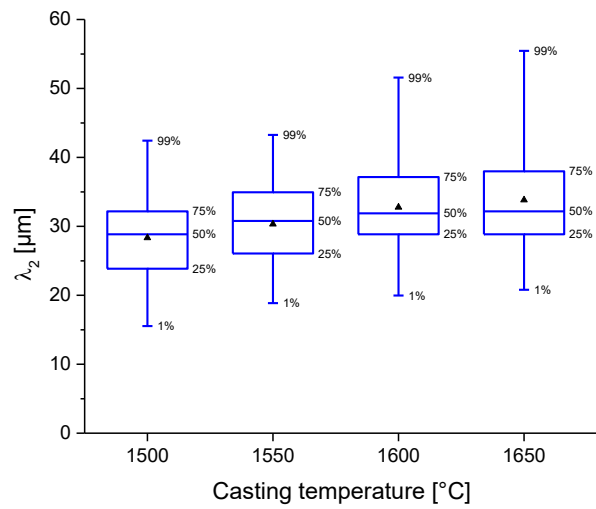
**Figure 6-9:** Secondary dendrite spacing at varying casting temperatures

$\lambda_2$ is measured in the ingot center, and as can be seen in **Figure 6-9** the mean values show a slight increase with growing casting temperature, this stands in good correlation with the results from the simulation of the solidification process.

The primary grain size changed massively through the increase of CT. On the left side of **Figure 6-10** the primary grain structure in an ingot cast with 1500 °C is indicated, on the right site, the respective image for a casting temperature of 1650 °C. The number of primary grains decreased with rising temperature. This indicates that the conditions for nucleation are better at lower casting temperatures. As discussed in the literature review, a higher supercooling leads to a significantly higher nucleation rate and a lower CT results in an earlier undercooling of the residual liquid, which results in the fine primary grain structure shown for 1500 °C.
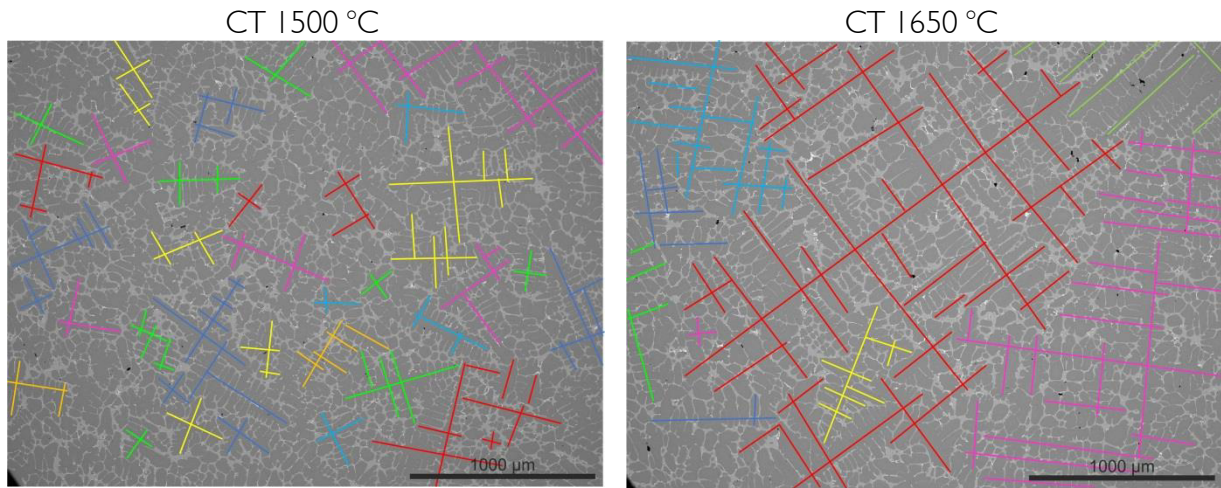
**Figure 6-10:** Qualitative image of the primary grain structures gained through different casting temperatures (left – 1500 °C, right – 1650 °C)

**Figure 6-11** gives the total carbide area in the four experimental ingots. No significant influence of the casting temperature is visible, and it fluctuates around a level of 8 %. In contrast, the ratio of coarse carbides depends significantly on the CT. At 1650 °C the amount of coarse carbides is as high as 27 %, while it is considerably lower at 13 % for 1500 °C. **Figure 6-12** shows how the ratio of coarse carbides corresponds to the casting temperature. **Figure 6-13** pictures the carbide structures for 1500 and 1650 °C. The amount of green areas increases apparently, as these zones correlate to the coarse carbides. There are no changes in the carbide type and the lamellar structure evident.
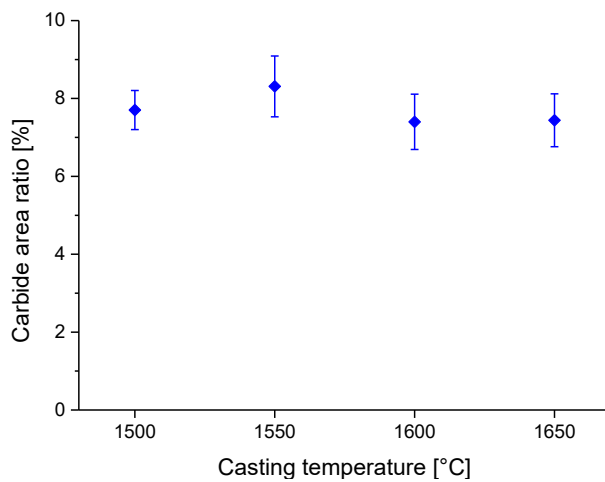


**Figure 6-11:** Total carbide area at varying casting temperatures
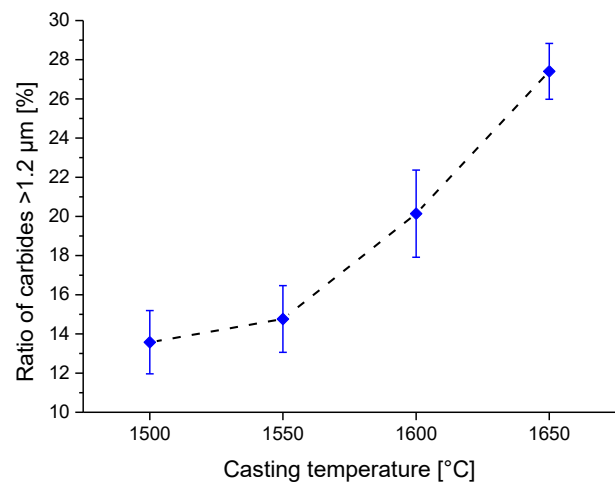


**Figure 6-12:** Ratio of coarse carbides at varying casting temperatures
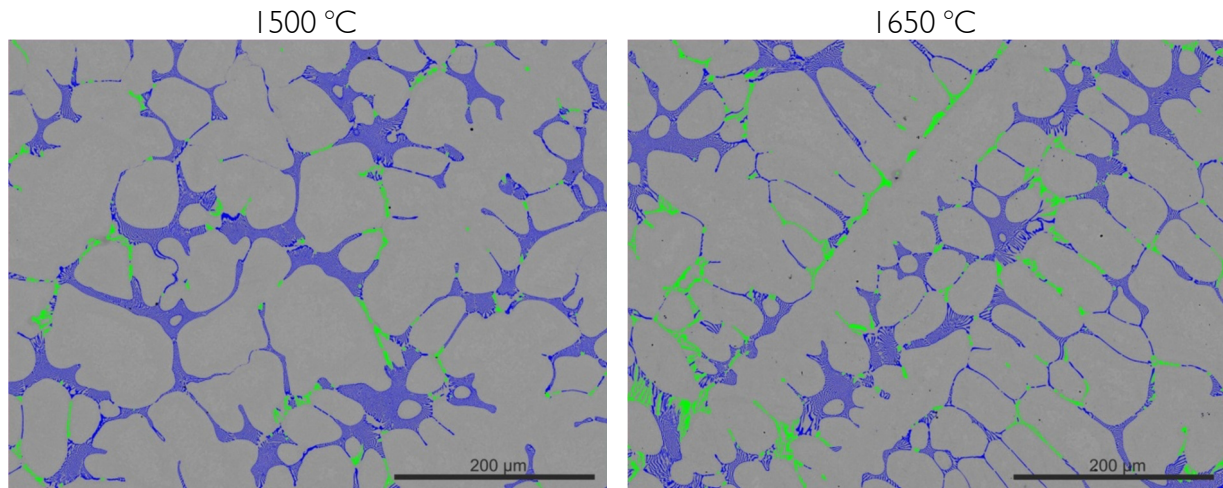
**Figure 6-13:** Image analysis of electron pictures at different casting temperatures
(blue – total carbide area, green – area of coarse carbides thicker 1.2 μm)

An increasing casting temperature results in a delayed CET and the size of primary grains and the ratio of coarse carbides rises significantly. The change in the carbide morphology is evident, and at this point, it is unclear if this is only an effect of the different cooling conditions and the resultant SDAS or also an influence of the finer primary grain size, and thus indicating that grain refinement could contribute to a refinement of primary carbides.

## 6.3 Industrial ingot

vBEG provided samples from an industrial as-cast HS2-9-1-8 ingot. The same measurement methods, as discussed before, are applied to these specimens. The results from the experiments are then compared with those of the investigation on the industrial ingot. Investigated are the CET, the secondary dendrite spacing, and the carbide morphology. The sketch in **Figure 6-14** shows the approximated sampling position.
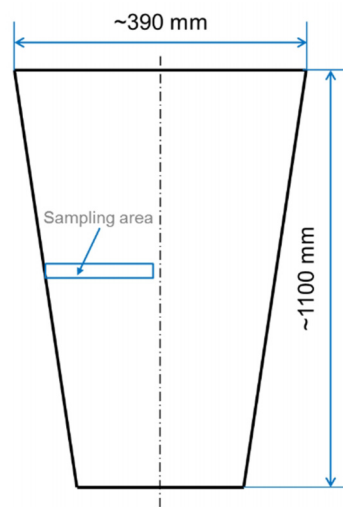


**Figure 6-14:** Sketch of sampling position in industrial ingot

In each of the seven samples the center area is analyzed (sample 1-surface; sample 7-center). Additionally, the ingot surface and center are investigated at position 0 and 8. **Figure 6-15** shows

the exact positions and the respective macrostructure. The CET is located approx. 50 mm under the ingot surface. From this point forward, the macrostructure consists of dendritic equiaxed grains. Further, towards the ingot center, the size of these grains gets smaller. As the ingot center is the last area to solidify, the supercooling could be higher and therefore the nucleation rate increases and the critical nuclei size decreases, leading to more nucleation sites and smaller primary grains.
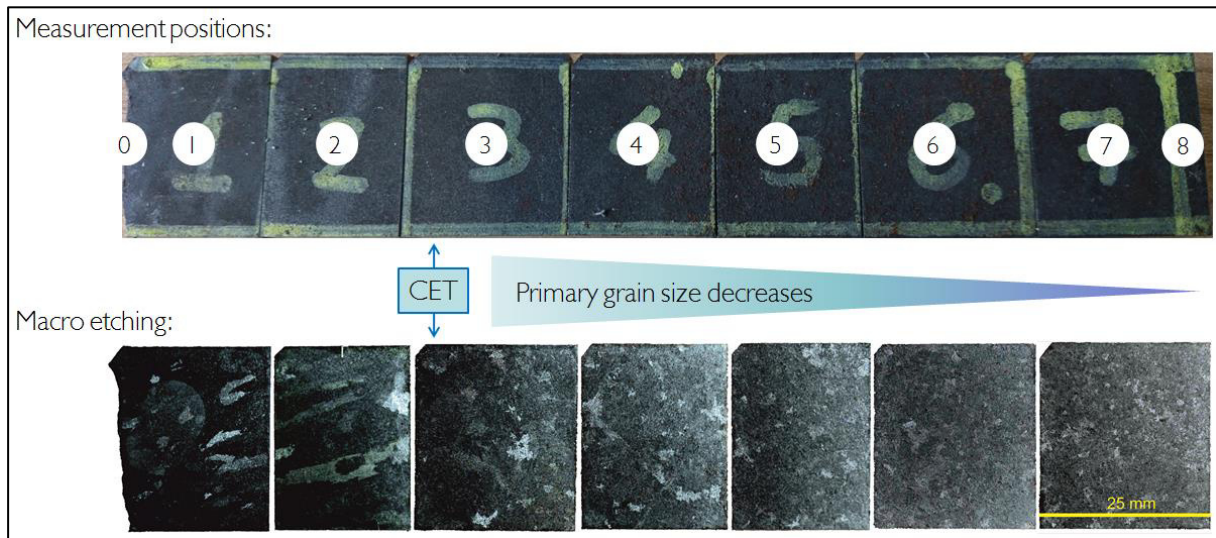


**Figure 6-15:** Measurement positions and macro etchings of industrial HSS ingot

The secondary dendrite spacings have a size of 22 µm at the surface and increase continuously until position 4 (74 mm to the surface). Then $\lambda_2$ reaches a plateau and deviates around a mean value of 70 µm. **Figure 6-16** pictures the course of $\lambda_2$ over the ingot cross-section.
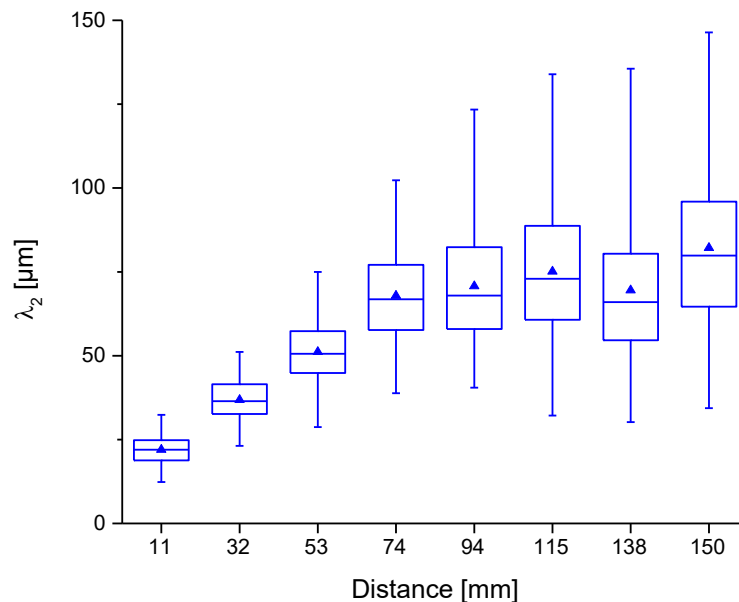


**Figure 6-16:** Secondary dendrite arm spacing from ingot surface to center

The total amount of carbides remains constant from the surface of the ingot to the center. **Figure 6-17** shows the mean total carbide area ratio for every position. The value oscillates around 8 %. Similar to the increase of $\lambda_2$ also the amount of coarse carbides grows. **Figure 6-18** pictures

the increase of carbide structures thicker than 1.2 µm as ratio of the total carbide content. It starts at 12 % and ends at a maximum of 69 %.
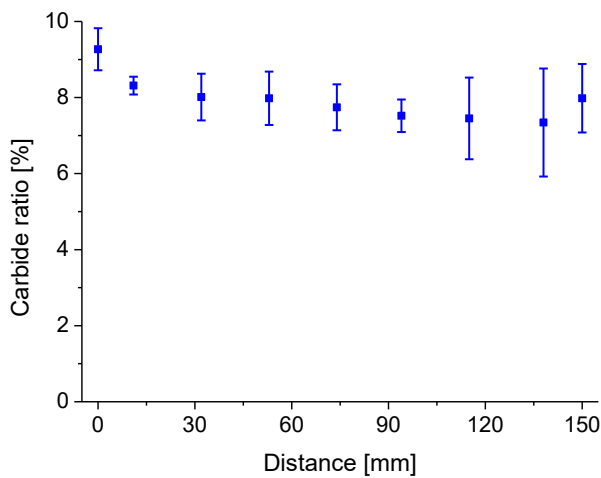


**Figure 6-17:** Total carbide area from ingot surface to center
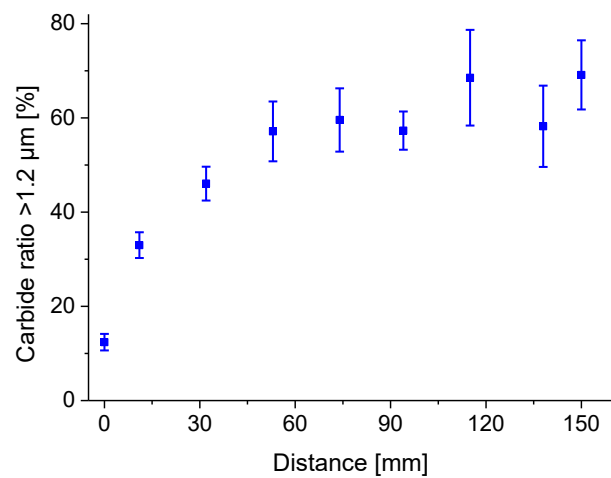
**Figure 6-18:** Ratio of coarse carbides from ingot surface to center

## 6.4  Effect of grain refinement on the solidification of HS2-9-1-8

The literature review does not clarify if the grain refinement of the primary grains can affect the eutectic carbides or not. While it is clear that the carbide distribution and eutectic carbide network can be improved by a higher number of primary grains, it is unclear if an additional effect on the carbide size exists. For this reason and the findings of the tests with changing casting temperature, experiments are performed with the aim of grain refinement, to investigate the influence of primary grain size on the volume fraction, size and size distribution of the eutectic carbides.

To achieve the most distinct results, a casting temperature of 1650 °C is chosen for the tests because here the ratio of coarse carbides is highest and possible differences induced to the carbide morphology through the change of primary grain size should be visible best. The first thing to consider when choosing an inoculation treatment is the primary solidifying phase. In the case of HS2-9-1-8, this is austenite, as can be seen in **Figure 2-6**. Thus, conditionings with Ti and Ce+Al are applied. It is expected that Ti reacts with nitrogen to form TiN, on which MC is precipitated. This combination is often reported as active to trigger grain refinement in high-speed steels. Significant changes of carbide types and forms have to be avoided. Thus the amount of titanium is strictly limited. **Figure 6-19** pictures a precipitation diagram calculated with FactSage. It shows that 150 ppm of Ti are sufficient to form (Ti, V)N just over the liquidus temperature, this is favorable because then the primary nitride has less time to grow into a coarse, blocky form. The second approach is the application of Ce and Al. A Ce/Al phase diagram for HSS is given in **Figure 6-20**. To ensure the formation of $AlCeO_3$ that is capable of nucleating austenite, the cerium content should be between 200 and 500 ppm and aluminum from 60 to 400 ppm. The red dot represents the actual contents of the experiment.
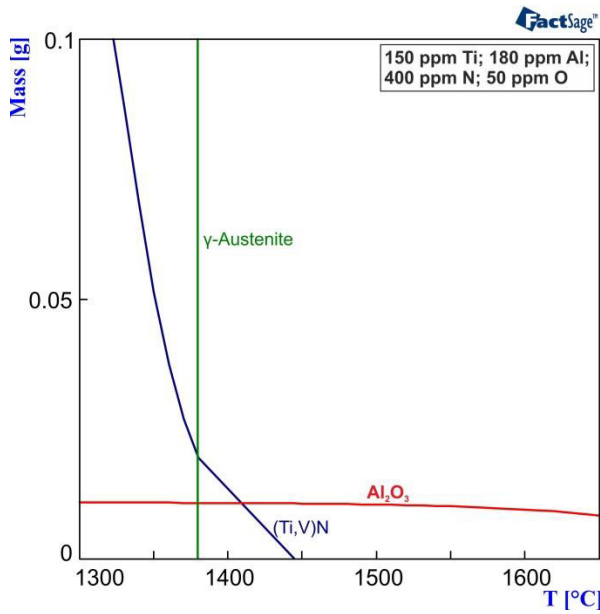
**Figure 6-19:** Precipitation diagram of (Ti,V)N for HSS (calculated with FactSage 7.2; FToxid and FSstel databases)
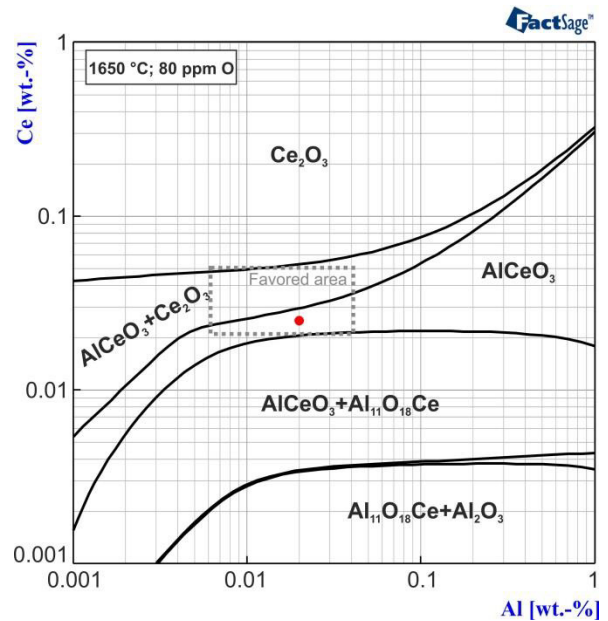
**Figure 6-20:** Ce/Al phase diagram for HSS with 80 ppm O at 1650 °C (calculated with FactSage 7.2; FToxid and FSstel databases)

Four castings are performed: The first is a reference ingot cast at 1650 °C, the second receives an Al deoxidation, the third is treated with cerium and aluminum, and the last is inoculated with titanium. The final chemical compositions are given in **Table 6-3**. The table with the composition of all elements can be found in the appendix.

**Table 6-3:** Chemical compositions of HSS inoculation experiments

|     | Ref     | Al-Ref  | CeAl    | Titanium |
| --- | ------- | ------- | ------- | -------- |
| C   | 1.03    | 0.95    | 1.04    | 1.00     |
| Si  | 0.41    | 0.49    | 0.49    | 0.48     |
| Mn  | 0.26    | 0.25    | 0.20    | 0.22     |
| Cr  | 3.83    | 3.79    | 3.68    | 3.66     |
| Mo  | 9.08    | 9.04    | 9.30    | 8.98     |
| Ni  | 0.35    | 0.41    | 0.35    | 0.38     |
| V   | 0.99    | 1.18    | 1.01    | 1.01     |
| W   | 1.36    | 1.38    | 1.31    | 1.37     |
| Co  | 7.62    | 7.50    | 7.73    | 7.80     |
| Ti  | <0.005  | <0.005  | <0.005  | 0.015    |
| Al  | 0.008   | 0.017   | 0.020   | 0.018    |
| N   | 0.035   | 0.042   | 0.040   | 0.040    |
| O   | 0.0072  | 0.0067  | 0.0084  | 0.0051   |
| Ce  | -       | -       | 0.025   | -        |

The ratio of directional solidification is one of the most significant parameters defining the success of grain refinement. Macro etchings turned out to be not very successful in revealing the ratio of equiaxed solidification. Micro etchings were necessary to determine the CET, exemplarily

**Figure 6-22** shows the microstructure 5 mm below the ingot surface. The Al deoxidized reference ingot, and the Ti treated sample show no detectable columnar area. In contrast, the ratio of columnar solidification amounts to roundabout 30 % for the reference ingot, and the CeAl treated the sample as can be seen in **Figure 6-21**. This indicates that CeAl treatment does not result in noticeable grain refinement.
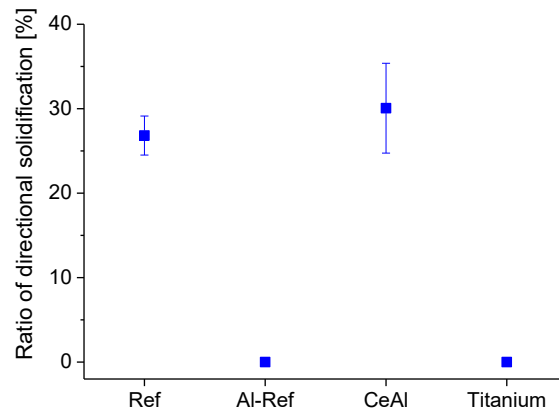


Figure 6-21: Ratio of directional solidification with different inoculation treatments
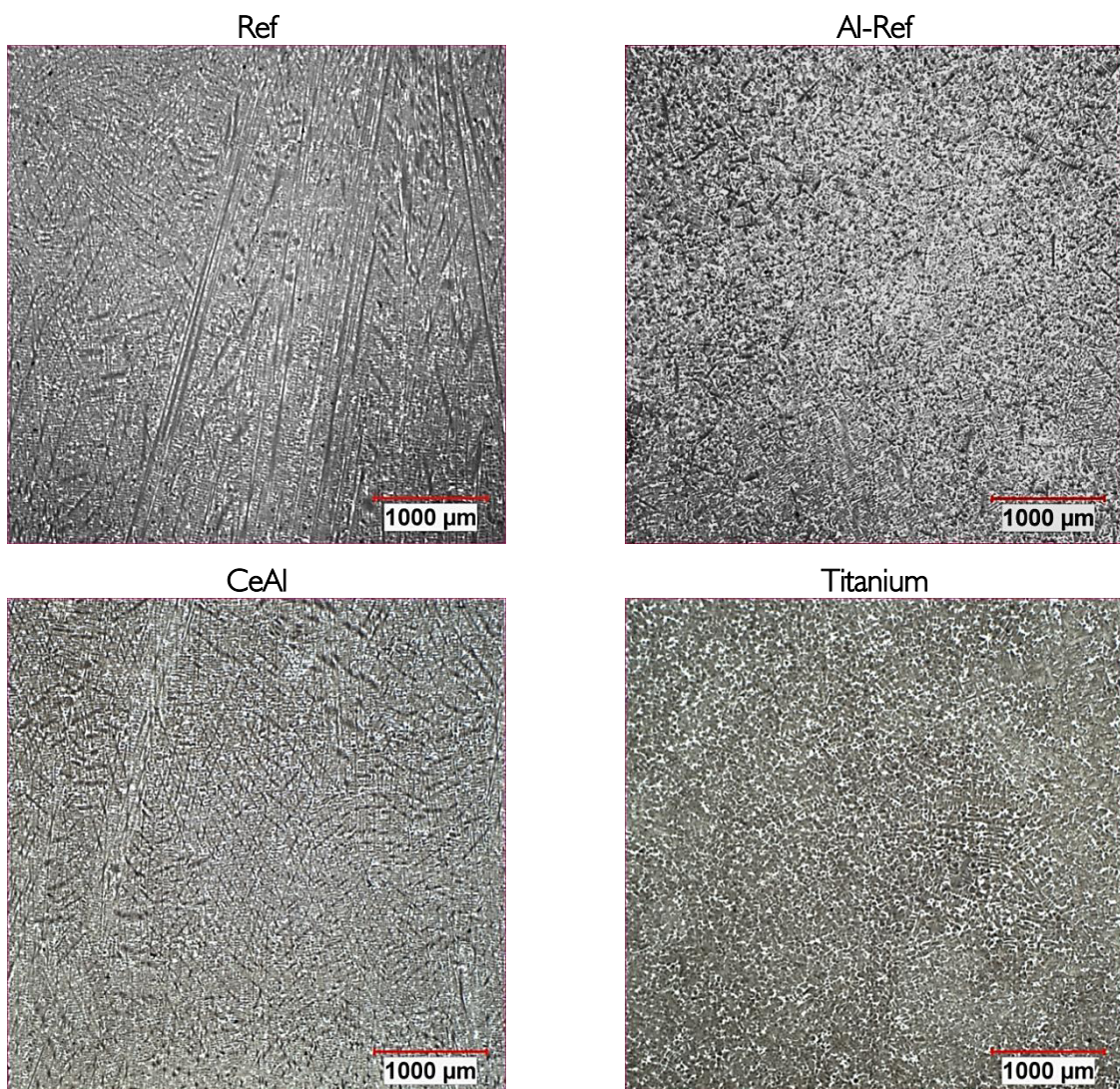


Figure 6-22: Microstructures of inoculated HSS 5 mm from the surface

The primary grain structure is qualitatively displayed in **Figure 6-23**. This result confirms the impression from the CET evaluation: Only the Al addition and the Ti treatment result in a change of macrostructure. The grains in the titanium treated ingot are so fragmented and difficult to distinguish from each other that only some of them can be marked.
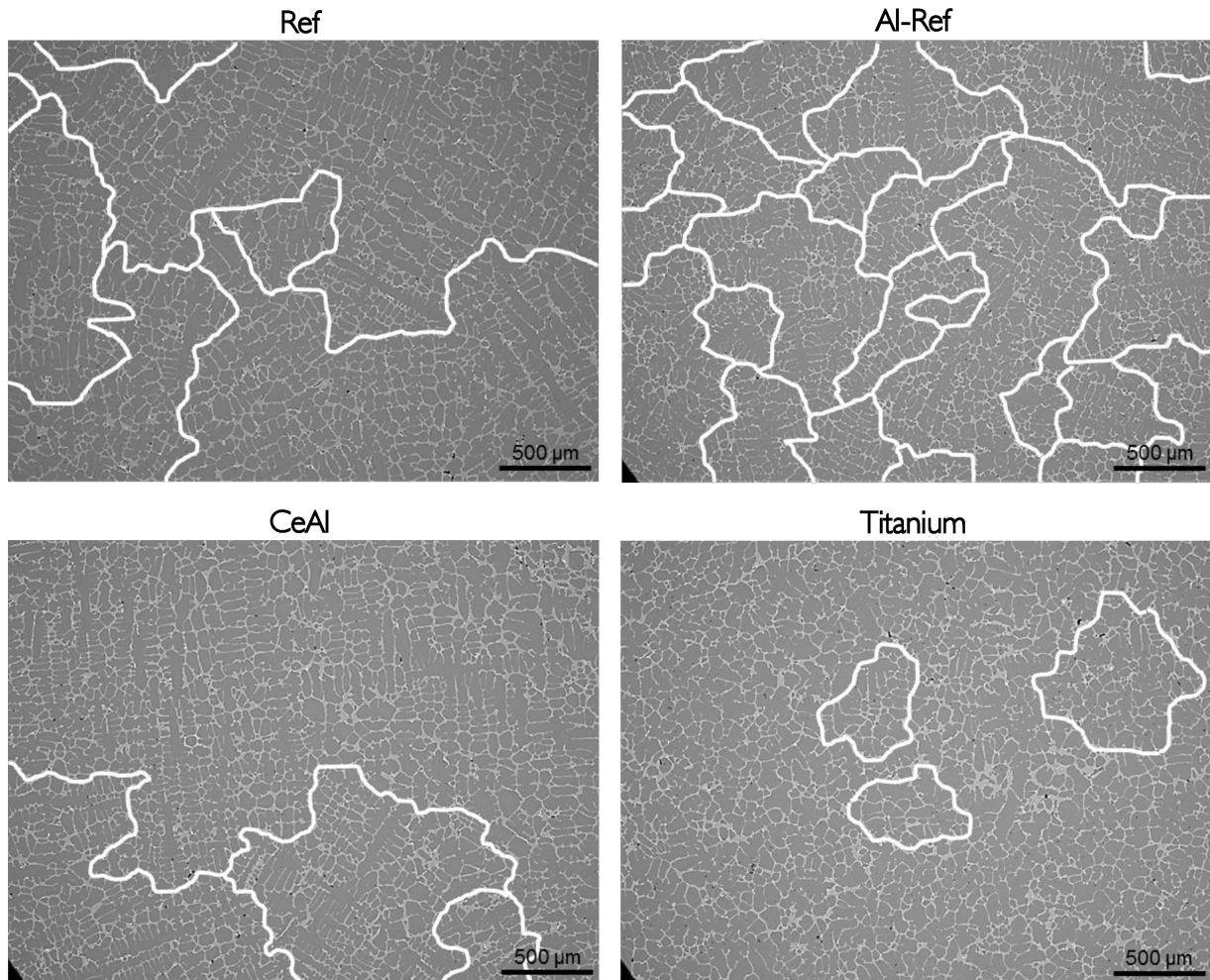


**Figure 6-23:** Primary grain structures after different inoculation treatments

As the NMI is one of the keys to successful grain refinement, they are evaluated in the next step. This is carried out via automated SEM-EDS measurements. Especially for the cerium-inclusions, it is a challenge to define a specific grey value to detect the particles as there is again a second phase ($M_2C$ in this case) brighter than the matrix. Thus, it seems very likely that only a part of the cerium-inclusions is detected. **Figure 6-24** shows the respective inclusion populations. The reference test ingot contains mostly mixed oxides with Al, Si and Mn with sizes between 1.2 and 1.5 µm. A typical example of such an inclusion is pictured in **Figure 6-25**.
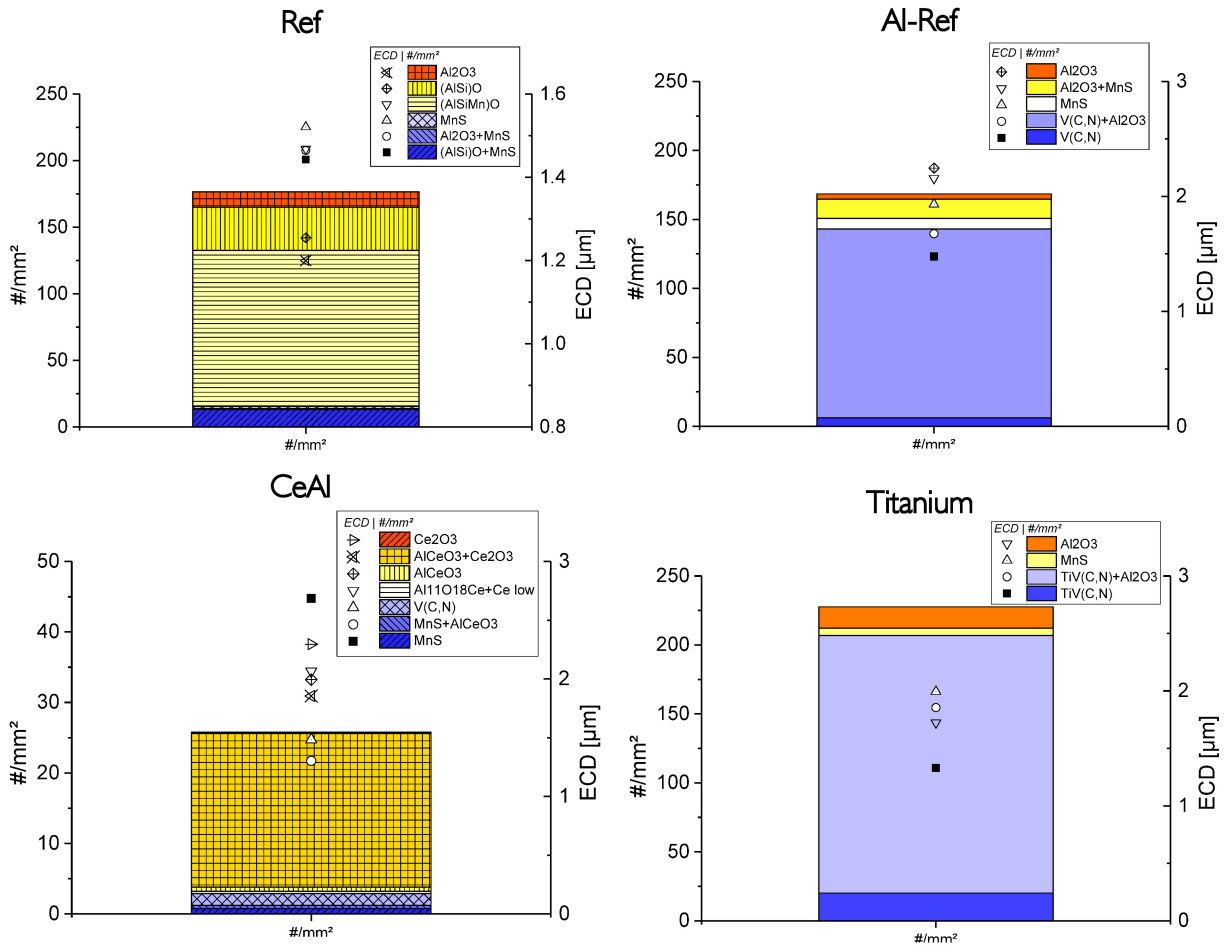
**Figure 6-24:** Number of particles and size with different inoculation treatments
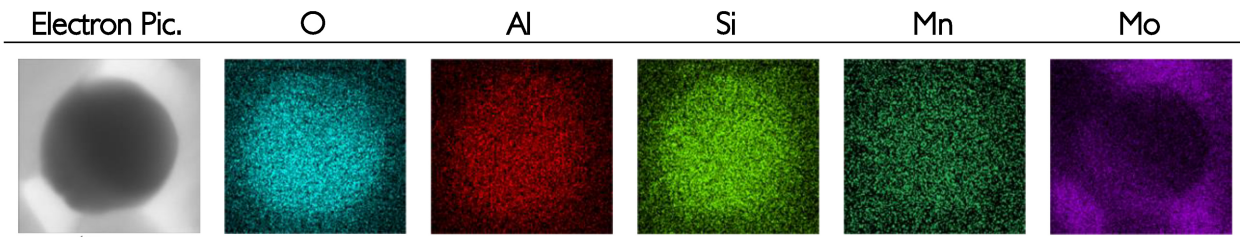


**Figure 6-25:** SEM phase mapping of (Al, Si,Mn)O in reference test ingot

The Al-Ref ingot shows mostly V(C,N) with a core of $Al_2O_3$. This can be attributed to the high content of V and N in this sample, which makes the precipitation of V(C,N) more likely. The mean ECD of this type of NMI is 1.5 µm. A phase mapping of such a particle is given in **Figure 6-26**. If these particles are located in the interdendritic region, they are quite large and thus disadvantageous for the mechanical properties. The grain refined structure indicates that V(C,N) is an active nucleus for austenite formation in HS2-9-1-8.
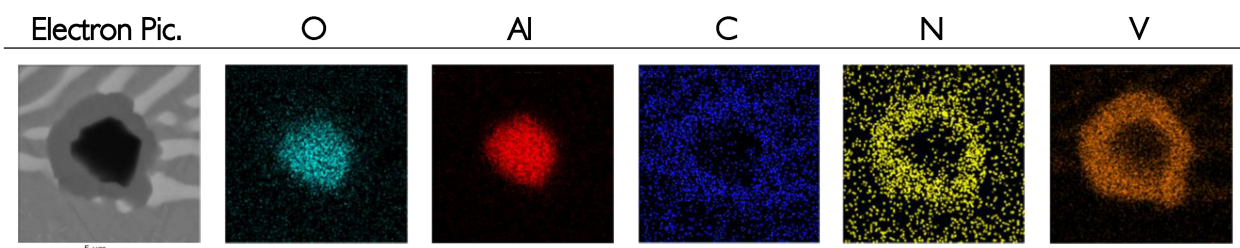


**Figure 6-26:** SEM phase mapping of $Al_2O_3$+V(C,N) in Al-Ref test

The difficult detection of the cerium-inclusions in the CeAl-ingot leads to a much lower number of detected particles in comparison to the other experiments. Most likely, the real number is higher. Typical inclusions have a core consisting of $Ce_2O_3$ surrounded by $AlCeO_3$. Approximately 33 % of them are found in the matrix. **Figure 6-27** shows that they can be associated with Mo too, which indicates the formation of $M_2C$ at the particle surface. Compared to the results of the SASS, it is surprising that these inclusions do not lead to grain refinement. The very different alloying system or a kind of nuclei poisoning could be the deciding factor.



| Electron Pic. | O | Al | Ce | Mo |
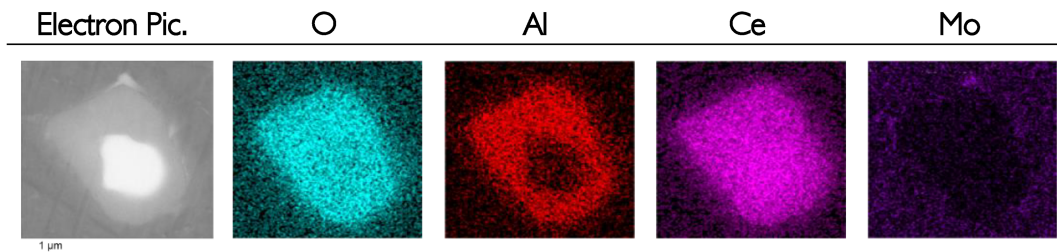
**Figure 6-27:** SEM phase mapping of $Ce_2O_3 + AlCeO_3$ in CeAl test

As discussed in the literature review, a parent nucleus, e.g. $Al_2O_3$, is necessary for the precipitation of TiN. For this reason, the melt is deoxidized with Al before the Ti addition. This leads to the formation of $Al_2O_3$ surrounded by (Ti, V)N, which acts as an active nucleation site for austenite. A typical particle is pictured in **Figure 6-29**. The Mo covering the (Ti,V)N could be the start of $M_2C$ formation. The inclusions are distributed in the interdendritic region as well as in the matrix. **Figure 6-28** pictures a particle in the middle of a dendrite, as well as two in the interdendritic area. It seems that the latter two act as the starting point for the eutectic $M_2C$ carbide.
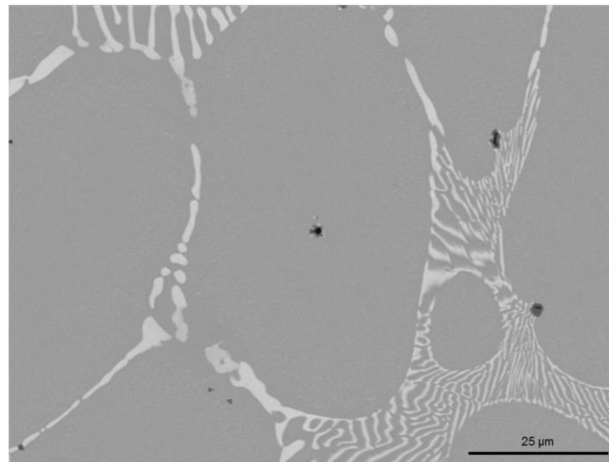


**Figure 6-28:** SEM electron image from the overview of microstructure in titanium treated HSS
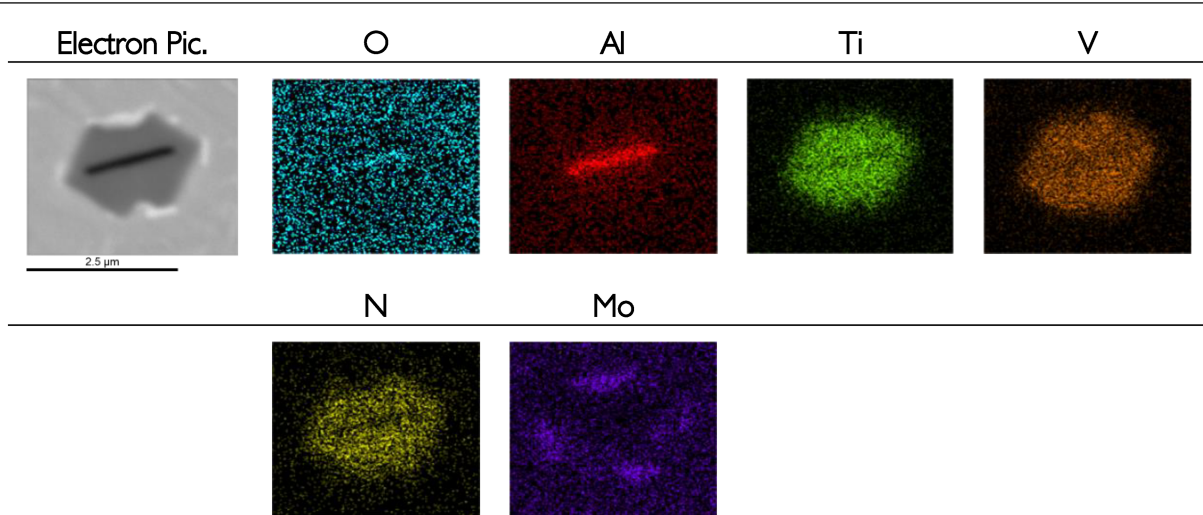
**Figure 6-29:** SEM phase mapping of $Al_2O_3 + (Ti,V)N + M_2C$ in titanium treated HSS

**Figure 6-30** displays the secondary dendrite arm spacings in the ingot center of the inoculation experiments. The Titanium test possesses the largest $\lambda_2$, but as **Figure 6-23** shows, it is nearly impossible to find positions for the correct measurement. So this value should be regarded with caution. The remaining mean values vary around 30 μm, confirming similar cooling conditions within the experiments.
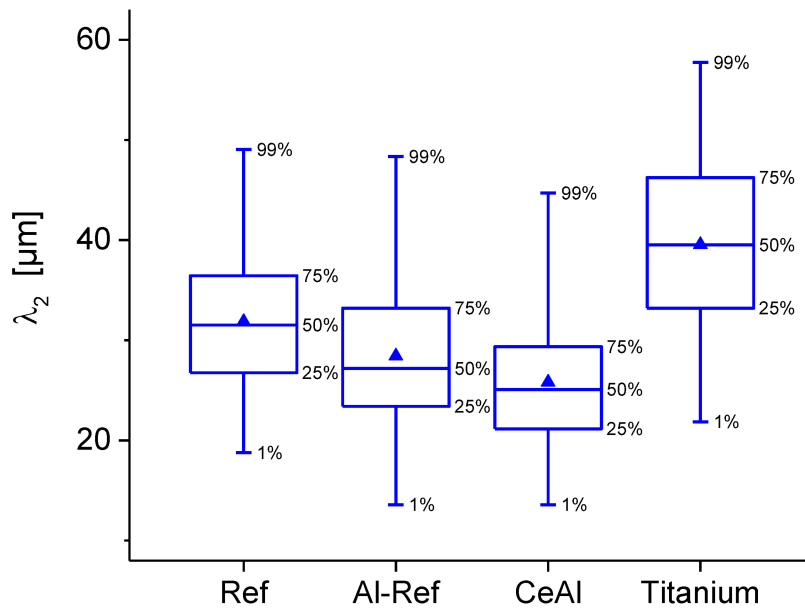


**Figure 6-30:** Secondary dendrite arm spacing with different inoculation treatments

The total carbide content decreases slightly in the treated ingots (**Figure 6-31**). As this is also true for the not grain refined test CeAl, this change cannot be an effect of grain refinement. Possible explanations could lie in the chemical analysis, effects of dissolved Ce or Al or in the case of the Al-Ref and Titanium test the precipitation of M(C,N) may be the cause because it consumes C and V for its formation that are later missing for the $M_2C$ nucleation. The ratio of coarse carbides in relation to the total carbide area is displayed in **Figure 6-32**. Within the range of standard deviation, it shows no changes and stays at a level of 22 %. No effect of smaller primary grain size on the ratio of coarse carbides can be distinguished.
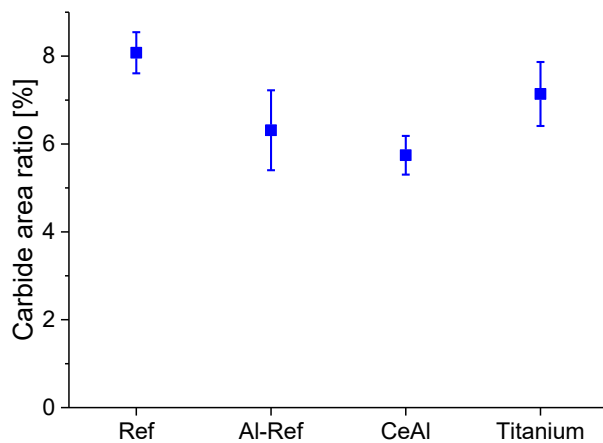
**Figure 6-31:** Total carbide area with different inoculation treatments
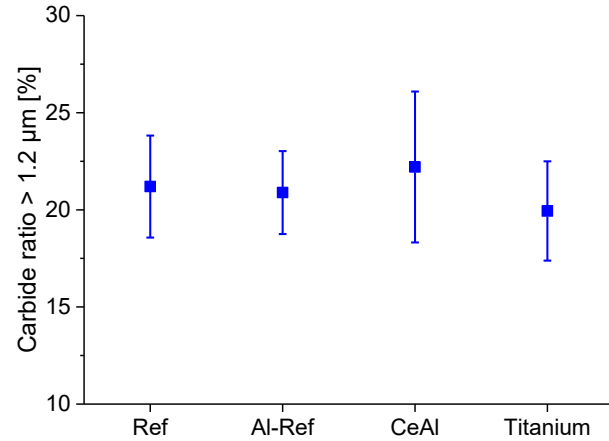


**Figure 6-32:** Ratio of coarse carbides with different inoculation treatments

## 6.5 Summary

High-speed steels are a hypo-eutectic alloy that precipitates a high amount of eutectic carbides. The chemical composition of the specific steel grade and the cooling conditions control the amount and type of the eutectic carbides. The major amount of carbides is either of the stable $M_6C$ and/or the metastable $M_2C$ type depending on the following conditions:

- The $M_2C$ formation is favored by high molybdenum, carbon and vanadium contents and by fast cooling rates. Vanadium controls the morphology of $M_2C$, when it surpasses a critical value of 21 at.-% in the carbide, it changes from a lamellar towards a plate-like structure.

- $M_6C$ precipitation is promoted by tungsten, silicon, nitrogen and niobium, and slow cooling rates.

HS2-9-1-8 belongs to the molybdenum group, which typically forms $M_2C$ carbides of a lamellar type under normal solidification conditions. The coarse regions of this carbide that form at the end of solidification should be decreased by means of inoculation, without changing the chemical composition of the steel grade. To enhance the understanding of the solidification of HS2-9-1-8, the effect of cooling and casting conditions as well as of inoculation on the macrostructure and the carbide morphology are examined.

Varying cooling rates (1, 5, 15 K/min) show a significant influence on the carbide precipitation. At 1 K/min, more than 70 % of the carbides are $M_6C$. This is unbeneficial as better material properties are achieved when the metastable $M_2C$ decomposes completely during heat treatment and hot deformation. A reason for this is that the decomposition into $M_6C$ and MC results in a smaller final carbide size and it releases alloying elements for the formation of secondary carbides. Additionally, the amount of coarse $M_2C$ carbides decreases with faster cooling rates.

The experiment with changing casting temperatures and inoculation thoroughly investigated the influence of primary grains size on the carbide precipitation. While the tests with changing casting temperature could give the impression that the primary grain size influences the ratio of coarse carbides, this is not confirmed in the grain refinement experiments. The primary grain size is

decreased massively with the decreasing casting temperature, as does the amount of carbides thicker than 1.2 µm. But the casting conditions are not the same, meaning that this could be the major influence on the carbide precipitation. Thus tests with inoculation are performed to picture the effect of primary grain size on the carbide morphology with similar casting conditions. On the one hand inoculation with $AlCeO_3$ is chosen, because it is a very effective nucleation site for austenite and additionally cerium is often mentioned for its improvement of carbide morphology. On the other hand, Ti is applied to trigger nucleation via the precipitation of MC carbides.

The latter inoculation method is very successful regarding the primary grain size, but $AlCeO_3$ does not affect the solidification structure. But the refinement of the primary grain size in the inoculation experiments also shows no influence on the ratio of coarse carbides. Even though (Ti,V)N seems to act as a starting point for the $M_2C$ as well as for the austenite (**Figure 6-28**), it does not affect the final eutectic carbide precipitation, which is considered critical for the formation of the more coarse morphologies. All of this indicates either a higher number of inclusions or a new inoculation method has to be applied to alter the $M_2C$ formation. Otherwise, changes to the chemical composition of HS2-9-1-8 could be a possible approach to change the morphology. But it has to be considered, that already with the normal alloying concept $M_6C$ is precipitated with a cooling rate of 1 K/min and further destabilizing the $M_2C$ formation would result in unwanted $M_6C$ formation at even faster cooling rates.

The experimental results can be compared to the samples of the industrial ingot. First is a comparison of the cooling conditions. Equation (25) is used to calculate the respective cooling rates from the measured $\lambda_2$. In the center of the industrial ingot $\dot{T} \approx 5$ K/min, this is much lower than in the experimental ingots. The cooling rates of those ranges from 60 to 100 K/min. **Figure 6-33** illustrates that the solidification parameters in the tests are more similar to the surface of the industrial ingot than to the center, where more of the coarse carbides are situated.



$$\lambda_2 = k \left( \frac{T_L - T_S}{\dot{T}} \right)^n = k\, t_f^n$$

k = 23.44   $T_L$ = 1381 °C
n = 0.359   $T_S$ = 1212 °C
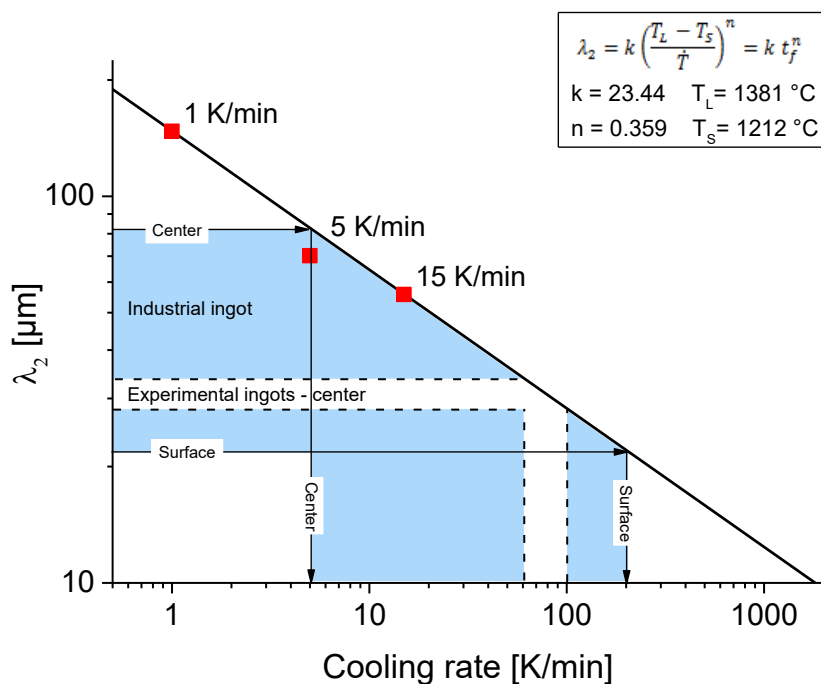
**Figure 6-33:** Comparison of cooling rates in industrial and experimental ingots

Comparing the secondary dendrite arm spacings and the ratio of coarse carbides to the industrial ingot paints a similar picture as for the cooling rates. The amount of coarse carbides in the experimental ingots corresponds to the ratio at the surface of the industrial ingot, as can be seen in **Figure 6-34**. While in the center of the industrial ingot the ratio of coarse carbides is even higher than in the TO experiment with a cooling rate of 5 K/min.
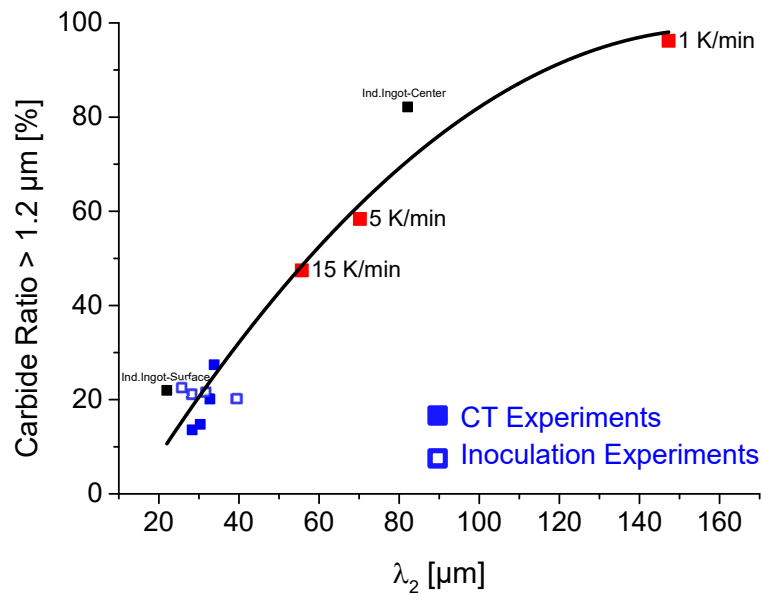


**Figure 6-34:** Ratio of coarse carbides vs. $\lambda_2$ for industrial ingot and experiments with varying cooling rate, casting temperature and inoculation treatments

# 7 Conclusion and Future Prospects

In the course of this thesis, manifold experimental and computational tools are applied to develop an advanced understanding of the requirements to ensure a beneficial solidification structure of two types of special steel grades. To direct the solidification towards an early columnar-to-equiaxed transition and small primary grains, heterogeneous nucleation on endogenous oxide-particles is promoted. Such inclusions have to fulfill certain conditions to be active nucleation sites:

- Thermodynamic stability
- A solid-state above the liquidus temperature of the steel
- Good wettability with the primary solidifying steel phase
- A planar lattice misfit smaller than 6 %

The investigated steel grades are the super-austenitic stainless steel X1CrNiMoCuN20-18-7 and the high-speed steel HS2-9-1-8, for both of them possible inoculation methods are chosen with the help of these four points. They solidify via austenite. Thus the application of $AlCeO_3$ is a reasonable course of action for both of them. Additionally, treatment with titanium is applied for the HSS. The following conclusions and future prospects are reached.

**X1CrNiMoCuN20-18-7:**
- The application of FactSage as a simulation tool of the particle population is reliable. It is possible to forecast the inclusion landscape for different contents of Ce, Al and O. The single-phase $AlCeO_3$ stability region must not be reached exactly, but it is an excellent starting point because there the highest number of $AlCeO_3$ is reached.
- The particle densities to ensure grain refinement can be lower than suggested in the literature. The best results are reached with a number density of 40 $AlCeO_3$/mm². These are 10-20 % of the total inclusion number. In literature a critical value of at least 170 cerium-inclusions/mm² is given, but it is not differentiated into the exact particle type [83].
- The solute effect of cerium is regarded as advantageous for grain refinement in [48]. The opposite is found in this thesis. In the presence of solute Ce tests with an inclusion density of 100-150 $AlCeO_3$/mm² performed worse than those with 40 $AlCeO_3$/mm² without free Ce, even though more nucleation sites are available in them. Additionally, there is also no grain refinement effect in ingots with enough Ce to form $Ce_2O_3$, which also goes along with a high value of dissolved Ce. In the investigated steel grade, no grain refining effect of solute cerium can be found.

- The casting conditions are a limiting factor for grain refinement. When the superheating of the melt increases above a specific limit, the heat flow mainly happens over the mold, and the conditions for equiaxed solidification in the center of the ingot are not reached fast enough. Then solidification is mostly columnar completely independent from the available heterogeneous nucleation sites.

- To enhance the knowledge on the effect of grain refinement after hot deformation and heat treatment, experiments with a Gleeble apparatus are performed. It showed a reduced grain growth of the refined material compared to industrial material that is exposed to the same procedure.

- Future investigations could lead toward grain refinement at even lower oxygen contents. The particle populations of the inclusion formation tests with 50 ppm O suggest that a sufficient number of $AlCeO_3$ is available even at these levels of oxygen.

- The mechanical properties of forged, heat-treated and grain refined material should be further investigated to enlighten the influence of a refined solidification structure on the material characteristics after deformation and recrystallization.

## HS2-9-1-8:

- The solidification path of HS2-9-1-8 typically leads over austenite and metastable, eutectic $M_2C$ carbide. The morphology of the carbide is generally of the finer lamellar type. The coarse plate-like type of $M_2C$, as reported for HS6-5-2 at V contents larger than 21 at.-% inside the carbide, is not found in HS2-9-1-8.

- Carbides exceeding a thickness of 1.2 µm are defined as coarse in this thesis, and the ratio of these regions should be diminished. Towards the end of solidification, the $M_2C$ lamellas become coarser.

- At cooling rates of 1 K/min, a significant amount of eutectic $M_6C$ is found in the samples. This should be avoided in industrial castings. Because $M_6C$ bears the disadvantage that it does not dissolve during heat treatment and hot deformation and therefore it does not release any alloying element for the precipitation of secondary carbides and its final size in the product is also enhanced.

- The cooling and casting conditions have the most substantial influence on the amount of coarse carbides. High cooling rates and low casting temperatures lead to decreasing amounts of $M_2C$ carbides thicker than 1.2 µm.

- For the grain refinement experiments with HSS $AlCeO_3$ and TiN are chosen as inoculants. The latter leads to the disappearance of the columnar zone and refines the primary grain size, while $AlCeO_3$ does not affect the solidification structure. No correlation between the size of the primary grains and the ratio of coarse carbides can be found.

- Grain refinement of the primary phase leads typically towards a better carbide distribution, and the carbide networks are less connected. This thesis does not include deformation steps or investigations of the mechanical properties. Thus it is not able to answer if this results in any improvement.

- The comparison to the industrial ingot showed that the cooling rates of the experiments picture only the ingot surface and not the ingot center. Thus future research should concentrate on carbide refinement at cooling rates of 5 K/min, because this is a reasonable value for the solidification conditions in the ingot center of an industrial ingot.

This thesis illustrates that the application of heterogeneous nucleation sites to induce an early columnar-to-equiaxed transition and small equiaxed primary grains is possible for X1CrNiMoCuN20-18-7 and HS2-9-1-8. This approach could be especially interesting for steel grades, where the cast structure leads to problems regarding hot deformation or other processing steps. An example is riding, which is a surface defect that appears in ferritic stainless steels due to columnar solidification during deformation. Another possible application would be as-cast products that experience no deformation at all.

# 8  References

[1] Ebner, R., Getting to know special steel: Special metallurgy, Sipiel, Milano, 2005.

[2] Engh, T.A., C.J. Simensen and O. Wijk, Principles of metal refining, Oxford University Press, Oxford, New York, 1992.

[3] Dantzig, J.A. and M. Rappaz, Solidification, 1. Auflage, EPFL Press, Lausanne, 2009.

[4] Koloszar, R., Kornfeinung hochlegierter Stähle durch heterogene Keimbildung, Masterthesis, Leoben, 2014.

[5] Andersson, M., L. Holappa, M. Kiviö, P. Naveau, M. Brandt and D. Espinosa et al., Grain size control in steel by means of dispersed non-metallic inclusions- GRAINCONT, RCFS publications, 2011.

[6] Casper van der Eijk, John Walmsley, Øystein Grong, Ole Svein Klevan (Eds.), Grain Refinement of fully Austenitic Stainless Steel using a Fe-Cr-Si-Ce Master Alloy, 2001.

[7] Haakonsen, F., Optimizing of Stromhard austenitic manganese steel, Dissertation, Trondheim, 2009.

[8] Haakonsen, F., J.K. Solberg, O.S. Klevan and C. van der Eijk, Grain Refinement of Austenitic Manganese Steels, Proceedings of AIStech 2011 Indianapolis.

[9] Lichtenegger, G.F., Entstehung und Stabilität des M2C-Eutektikums in Schnellarbeitsstählen, Dissertation, Leoben, 1995.

[10] Fredriksson, H. and M. Nica, The Influence of Vanadium, Silicon and Carbon on the Eutectic Reaction in M2 High-Speed Steels, Scandinavian Journal of Metallurgy 8 (1979), 6, 243–253.

[11] Fischmeister, H.F., R. Riedl and S. Karagoz, Solidification of High-Speed Tool Steels, Metallurgical and Materials Transactions A 20A (1989), 10, 2133–2148.

[12] Fredriksson, H. and S. Brising, Formation of Carbides During Solidification of High-Speed Steels, Scandinavian Journal of Metallurgy 5 (1976), 6, 268–275.

[13] Qu, M.-g., S.-h. Sun, X.-h. Bai, Z.-p. Shi, Y. Gao and W.-t. Fu, Hot Deformation Behavior of As-cast AISI M2 High-speed Steel Containing Mischmetal, Journal of Iron and Steel Research International 21 (2014), 1, 60–68.

[14] Zhou, B., Y. Shen, J. Chen and Z.-s. Cui, Evolving mechanism of eutectic carbide in as-cast AISI M2 high-speed steel at elevated temperature, Journal of Shanghai Jiaotong University (Science) 15 (2010), 4, 463–471.

[15] Kurz, W. and D.J. Fisher, Fundamentals of solidification, 4., rev. ed., reprinted., Trans Tech Publ, Uetikon-Zuerich, 1998.

[16] Gottstein, G., Physikalische Grundlagen der Materialkunde, Springer, 2007.

[17] Stefanescu, D.M., Science and engineering of casting solidification, 2nd ed., Springer Science+Business Media, LLC, New York, 2009.

[18] Durand-Charre, M., Microstructure of Steels and Cast Irons, Springer, Berlin, Heidelberg, 2004.

[19] Hunt, J.D., Steady state columnar and equiaxed growth of dendrites and eutectic, Materials Science and Engineering 65 (1984), 1, 75–83.

[20] Stainless steel world, Stainless steels and its families, http://www.stainless-steel-world.net/basicfacts/stainless-steel-and-its-families.html, Abgerufen am: 23.05.2019.

[21] Lippold, J.C. and D.J. Kotecki, Welding metallurgy and weldability of stainless steels, Wiley-Interscience, Hoboken NJ, 2005.

[22] Marshall, P., Austenitic stainless steels: Microstructure and mechanical properties, Elsevier, London u.a., 1984.

[23] Boccalini, M. and H. Goldenstein, Solidification of high speed steels, International Materials Reviews (UK) 46 (2001), 2, 92–115.

[24] Fredriksson, H. and U. Akerlind, Solidification and Crystallization Processing in Metals and Alloys, 3rd ed., Wiley, Hoboken, 2012.

[25] Baumgartner, K., Bernhard, C., Pfeiffer, A., Wieser, G., Hafok, M., Influence of casting temperature on the microstructure of AISI M42 high speed steel, Proceedings of Ingot casting, rolling and forging conference Stockholm 2018.

[26] Fisher, D.J. and W. Kurz, A theory of branching limited growth of irregular eutectics, Acta Metallurgica 28 (1980), 6, 777–794.

[27] Riedl, R., Erstarrungsverlauf bei Schnellarbeitsstählen, Dissertation, Leoben, 1984.

[28] Alan M. Bayer and Bruce A. Becherer, ASM Handbook, Vol. 16 Machining.

[29] Pöckl, G., Karbidfeinung und nichtmetallische Einschlüsse in ledeburitischen Werkzeugstählen insbesondere Schnellarbeitsstählen, Dissertation, Leoben, 2000.

[30] Luan, Y., N. Song, X. Kang and D. Li, A Study of the Carbides in High-Speed Steel Rolls, Materials Science Forum Vols 638-642 (2010), 3356–3361.

[31] Pirtovšek, T.V., G. Kugler, M. Godec and M. Terčelj, Three Important Points that Relate to Improving the Hot Workability of Ledeburitic Tool Steels, Metallurgical and Materials Transactions A 43 (2012), 10, 3797–3808.

[32] Zhou, X.F., F. Fang, F. Li and J.Q. Jiang, Morphology and microstructure of M2C carbide formed at different cooling rates in AISI M2 high speed steel, Journal of Materials Science & Technology 46 (2011), 5, 1196–1202.

[33] Zhou, X., W. Zhu, H. Jiang, F. Fang, Y. Tu and J. Jiang, A New Approach for Refining Carbide Dimensions in M42 Super Hard High-speed Steel, Journal of Iron and Steel Research, International 23 (2016), 8, 800–807.

[34] world steel association, World steel in numbers 2018, https://www.worldsteel.org/en/dam/jcr:f9359dff-9546-4d6b-bed0-996201185b12/World+Steel+in+Figures+2018.pdf, Abgerufen am: 19.11.2018.

[35] Wu, X.Q., Y.S. Yang, J.S. Zhang, G.L. Jia and Z.Q. Hu, Structure characteristics in industrially centrifugally cast 25Cr20Ni stainless steel tubes solidified under different electromagnetic field intensity, Journal of Materials Engineering and Performance 8 (1999), 5, 525–530.

[36] Li, J., J.-h. Ma, C.-j. Song, Z.-j. Li, Y.-l. Gao and Q.-j. Zhai, Columnar to Equiaxed Transition During Solidification of Small Ingot by Using Electric Current Pulse, Journal of Iron and Steel Research, International 16 (2009), 6, 7–12.

[37] Liao, X., Q. Zhai, J. Luo, W. Chen and Y. Gong, Refining mechanism of the electric current pulse on the solidification structure of pure aluminum, Acta Materialia 55 (2007), 9, 3103–3109.

[38] Patel, B., G.P. Chaudhari and P.P. Bhingole, Microstructural evolution in ultrasonicated AS41 magnesium alloy, Materials Letters 66 (2012), 1, 335–338.

[39] Abbasi-Khazaei, B. and S. Ghaderi, A Novel Process in Semi-Solid Metal Casting, Journal of Materials Science & Technology 28 (2012), 10, 946–950.

[40] Ali, Y., D. Qiu, B. Jiang, F. Pan and M.-X. Zhang, Current research progress in grain refinement of cast magnesium alloys: A review article, Journal of Alloys and Compounds 619 (2015), 639–651.

[41] Bramfitt, B.L., The Effect of Carbide and Nitride Additions on the Heterogeneous Nucleation Behavior of Liquid Iron, Metallurgical Transactions 1 (1970), 1987–1995.

[42] Turnbull, D. and B. Vonnegut, Nucleation Catalysis, Industrial & Engineering Chemistry 44 (1952), 6, 1292–1298.

[43] Kelly, P.M. and M.-X. Zhang, Edge-to-edge matching - a new approach to the morphology and crystallography of precipitates, Materials Forum 23 (1999), 41–62.

[44] Greer, A.L., A.M. Bunn, A. Tronche, P.V. Evans and D.J. Bristow, Modelling of inoculation of metallic melts: application to grain refinement of aluminium by Al–Ti–B, Acta Materialia 48 (2000), 11, 2823–2835.

[45] Easton, M. and D. StJohn, Grain refinement of aluminum alloys: Part I. the nucleant and solute paradigms—a review of the literature, Metallurgical and Materials Transactions A 30 (1999), 6, 1613–1623.

[46] Easton, M. and D. StJohn, Grain refinement of aluminum alloys: Part II. Confirmation of, and a mechanism for, the solute paradigm, Metallurgical and Materials Transactions A 30 (1999), 6, 1625–1633.

[47] Johnsson, M., L. Backerud and G.K. Sigworth, Study of the mechanism of grain refinement of aluminum after additions of Ti- and B-containing master alloys, Metallurgical Transactions A 24 (1993), 2, 481–491.

[48] Ji, Y., M.-X. Zhang and H. Ren, Roles of Lanthanum and Cerium in Grain Refinement of Steels during Solidification, Metals 8 (2018), 11, 884.

[49] H. Trenkler, W. Krieger, L. Gmelin, R. Durrer (Eds.), Metallurgie des Eisens, 4. Auflage, Verl. Chemie (Bd 5 ff Springer), Weinheim, 1978.

[50] Tuttle, R., Effect of Rare Earth Additions on Grain Refinement of Plain Carbon Steels, International Journal of Metalcasting 6 (2012), 2, 51–65.

[51] Grong, Ø., Metallurgical modelling of welding, The Institute of Materials, 1997.

[52] Zhang, M.-X. and P.M. Kelly, Crystallographic features of phase transformations in solids, Progress in Materials Science 54 (2009), 8, 1101–1170.

[53] Zhang, M.-X., P.M. Kelly, M. Qian and J.A. Taylor, Crystallography of grain refinement in Mg–Al based alloys, Acta Materialia 53 (2005), 11, 3261–3270.

[54] Ali, Y., D. Qiu, B. Jiang, F. Pan and M.-X. Zhang, The influence of CaO addition on grain refinement of cast magnesium alloys, Scripta Materialia 114 (2016), 103–107.

[55] Zhang, M.-X. and P.M. Kelly, Edge-to-edge matching model for predicting orientation relationships and habit planes—the improvements, Scripta Materialia 52 (2005), 10, 963–968.

[56] Arvola, D.A., S.N. Lekakh, R.J. O'Malley and L.N. Bartlett, Two Inoculation Methods for Refining As-Cast Grain Structure in Austenitic 316L Steel, International Journal of Metalcasting, 1–15.

[57] Zhu, H.-w., W.-j. Ke, Z.-p. Zhao, S. Qin, F.-r. Xiao and B. LIAO, Refinement effectiveness of self-prepared (NbTi)C nanoparticles on as-cast 1045 steel, Materials & Design 139 (2018), 531–540.

[58] Grong, Ø. and O.S. Klevan, Verfahren zur Kornfeinung von Stahl, Kornfeinungslegierung für Stahl und Herstellungsverfahren für Kornfeinungslegierung, Patent Nr. EP 1 257 673 B1.

[59] Grong, Ø., L. Kolbeinsen, C. van der Eijk and G. Tranell, Microstructure control of steels through dispersoid metallurgy using novel grain refining alloys, ISIJ International 46 (2006), 6, 824–831.

[60] Chaus, A.S., Microstructural and properties evaluation of M2 high speed steel after inoculating addition of powder W and WC, Materials Science and Technology 30 (2014), 9, 1105–1115.

[61] Chaus, A.S. and Y. Porubski, Effect of modifying tungsten additions on formation of primary structure of R6M5-type high-speed steel, Physics of Metals and Metallography 113 (2012), 11, 1068–1078.

[62] Isobe, K., Effect of Mg Addition on Solidification Structure of Low Carbon Steel, ISIJ International 50 (2010), 12, 1972–1980.

[63] Nuri, Y., T. Ohashi, T. Hiromoto and O. Kitamura, Solidification Macrostructure of Ingots and Continuously Cast Slabs Treated with Rare Earth Metal, ISIJ International 22 (1982), 6, 408–416.

[64] Suito, H., H. Ohta and S. Morioka, Refinement of Solidification Microstructure and Austenite Grain by Fine Inclusion Particles, ISIJ International 46 (2006), 6, 840–846.

[65] Guo, M. and H. Suito, Influence of Dissolved Cerium and Primary Inclusion Particles of Ce2O3 and CeS on Solidification Behavior of Fe-0.20mass%C-0.02mass%P Alloy, ISIJ International 39 (1999), 7, 722–729.

[66] Bandyopadhyay, T.R., P.K. Rao and N. Prabhu, Development of ultrahigh strength steel through electroslag remelting with inoculation, Ironmaking & Steelmaking 33 (2006), 4, 337–343.

[67] Bandyopadhyay, T.R., P.K. Rao and N. Prabhu, Effect of inoculation during electroslag refining on grain size of 15CDV6 and modified 15CDV6 steels, Ironmaking & Steelmaking 33 (2013), 4, 331–336.

[68] Gennesson, M., D. Daloz, J. Zollinger, B. Rouat, J. Demurger, D. Poirier and H. Combeau, Inoculation Experiments in Lab Scale Castings of Low Alloyed Steel, Proceedings of the 6th Decennial International Conference on Solidification Processing 2017 Old Windsor, 486–489.

[69] Gennesson, M., D. Daloz, J. Zollinger, B. Rouat, D. Joelle and D. Poirier et al., Inoculation in Lab Scale Low Alloyed Steel Castings, 2018.

[70] Niu, Y., H. Tang, Y. Wang, X. Chen, Z. Wang, K. Chen, Y. Wu and X. Liu, Effect of In Situ Nano-Particles on the Microstructure and Mechanical Properties of Ferritic Steel, Steel research international 87 (2016), 11, 1389–1394.

[71] Tuttle, R., Understanding the Mechanism of Grain Refinement in Plain Carbon Steels, International Journal of Metalcasting 7 (2013), 4, 7–16.

[72] Morioka, S. and H. Suito, Effect of Oxide Particles on δ/γ Transformation and Austenite Grain Growth in Fe–0.05~0.30%C–1.0%Mn–1.0%Ni Alloy, ISIJ International 48 (2008), 3, 286–293.

[73] Ruizhen, G., H. Hanqi and Z. Xueyou, Effects of rare earth elements on solidification of steels, in: X. Guangxian, X. Jimei (Eds.), New frontiers in rare earth science and applications: Proceedings of the International conference on rare earth development and applications; Beijing, September 10-14, 1985 (also: ICRE 1985), Elsevier, Beijing, 1985, pp. 1277–1282.

[74] Adabavazeh, Z., W.S. Hwang and Y.H. Su, Effect of Adding Cerium on Microstructure and Morphology of Ce-Based Inclusions Formed in Low-Carbon Steel, Scientific reports 7 (2017), 46503.

[75] Lekakh, S.N., J. Ge, V. Richards, R. O'Malley and J.R. TerBush, Optimization of Melt Treatment for Austenitic Steel Grain Refinement, Metallurgical and Materials Transactions B 48 (2017), 1, 406–419.

[76] Sakata, K. and H. Suito, Dispersion of fine primary inclusions of MgO and ZrO2 in Fe-10 mass pct Ni alloy and the solidification structure, Metallurgical and Materials Transactions B 30 (1999), 6, 1053–1063.

[77] Mizumoto, M., S. Sasaki, T. Ohgai and A. Kagawa, Development of new additive for grain refinement of austenitic stainless steel, International Journal of Cast Metals Research 21 (2008), 1, 49–55.

[78] Janis, J., K. Nakajima, A. Karasev, S. Jonsson, R. Inoue and P.G. Jönsson, Effects of Primary Oxide and Oxide-Nitride Particles on the Solidification Structure in a Fe-20 mass%Cr Alloy Deoxidised with Ti and M (M = Zr or Ce), ISIJ International 53 (2013), 2, 221–229.

[79] Kimura, K., S. Fukumoto, G. Shigesato and A. Takahashi, Effect of Mg Addition on Equiaxed Grain Formation in Ferritic Stainless Steel, Tetsu-to-Hagane 98 (2012), 11, 601–609.

[80] Shi, C., G. Cheng, Z. Li and P. Zhao., Solidification Structure Refining of 430 Ferrite Stainless Steel With TiN Nucleation, Journal of Iron and Steel Research, International 15 (2008), 3, 57–60.

[81] Poole, W.J., A. Mitchell and F. Weinberg, Inoculating stainless steel with titanium nitride, High Temperature Materials and Processes (UK) 16 (1997), 3, 173–182.

[82] Park, J.H., Effect of inclusions on the solidification structures of ferritic stainless steel: Computational and experimental study of inclusion evolution, Calphad 35 (2011), 4, 455–462.

[83] Dahle, E.S., Grain Refinement of High Alloyed Steel With Cerium Addition, Diplomarbeit/Masterthesis, Trondheim, 2011.

[84] Kim, K.-H. and C.-M. Bae, Reduction of segregation during casting of 100Cr6 bearing steel by cerium inoculation, Metals and Materials International 19 (2013), 3, 371–375.

[85] Chaus, A.S., Modifying Cast Tungsten-Molybdenum High-Speed Steels with Niobium, Zirconium, and Titanium, Metal Science and Heat Treatment 47 (2005), 1-2, 53–61.

[86] Fischmeister, H. F., Karagöz, S., Larsson, S., Liem, I., Sotokovszki, P., Nucleation of primary MC carbides in a high speed steel: A study by ion micorprobe and STEM-EDS, in: Fortschritte in der Metallographie, Riederer-Verl, 1987, pp. 467–478.

[87] Fu, H., Q. Xiao and Y. Li, A study of the microstructures and properties of Fe–V–W–Mo alloy modified by rare earth, Materials Science and Engineering A 395 (2005), 1-2, 281–287.

[88] Hamidzadeh, M.A., M. Meratian and M. Mohammadi Zahrani, A study on the microstructure and mechanical properties of AISI D2 tool steel modified by niobium, Materials Science and Engineering A 556 (2012), 758–766.

[89] Hufenbach, J., A. Helth, M.-H. Lee, H. Wendrock, L. Giebeler, C.-Y. Choe, K.-H. Kim, U. Kühn, T.-S. Kim and J. Eckert, Effect of cerium addition on microstructure and mechanical properties of high-strength Fe85Cr4Mo8V2C1 cast steel, Materials Science and Engineering A 674 (2016), 366–374.

[90] Jiangtao, D., J. Zhiqiang and F. Hanguang, Effect of RE-Mg complex modifier on structure and performance of high speed steel roll, Journal of Rare Earths 25 (2007), 259–263.

[91] Kastanek, O., Effect of titanium and tantalum on the structure and mechanical properties of cast tools in a 9% tungsten high-speed steel, Archiev Eisenhuttenwesen 39 (1968), 10, 763.

[92] Kheirandish, S. and Mirdamadi, Effect of Ti and Nb on the microstructure and mechanical properties of cast high speed steel, Metall (Berlin) 53 (1999), 6, 339.

[93] Kheirandish, S., Y.H.K. Kharrazi and S. Mirdamadi, Cast M7 high speed steel modified with titanium, Materials Science and Technology 14 (1998), 7, 683–688.

[94] Kheirandish, S., S. Mirdamadi and Y.H.K. Kharrazi, Effect of titanium on cast structure of high speed steel, Materials Science and Technology 14 (1998), 4, 312–316.

[95] Kheirandish, S. and A. Noorian, Effect of Niobium on Microstructure of Cast AISI H13 Hot Work Tool Steel, Journal of Iron and Steel Research, International 15 (2008), 4, 61–66.

[96] Yang, J., D.-n. Zou, X.-m. Li and Z.-z. Du, Effect of Rare Earth on Microstructures and Properties of High Speed Steel With High Carbon Content, Journal of Iron and Steel Research, International 14 (2007), 1, 47–59.

[97] Wang, M., L. Cchen, Z. Wang and E. Bao, Influence of rare earth elements on solidification behavior of a high speed steel for roll using differential scanning calorimetry, Journal of Rare Earths 29 (2011), 11, 1089–1094.

[98] Qihong, C., J. Zhiqiang and F. Hanguang, Effect of Ti addition on the microstructure and properties of a high speed steel roll, Materialprüfung 55 (2013), 11-12, 871–876.

[99] Löcker, K.-D., Untersuchungen zur Weiterentwicklung nioblegierter Schnellarbeitsstähle, insbesondere zur Verbesserung von Gefügeaufbau und Eigenschaften, Dissertation, Leoben, 1988.

[100] Zhou, X., X. Yin., F. Fang, J. Jiang. and W. Zhu, Influence of rare earths on eutectic carbides in AISI M2 high speed steel, Journal of Rare Earths 30 (2012), 10, 1075–1078.

[101] Bartlett, L.N. and B.R. Avila, Grain Refinement in Lightweight Advanced High-Strength Steel Castings, International Journal of Metalcasting 10 (2016), 4, 401–420.

[102] Hamidzadeh, M.A., M. Meratian and A. Saatchi, Effect of cerium and lanthanum on the microstructure and mechanical properties of AISI D2 tool steel, Materials Science and Engineering A 571 (2013), 193–198.

[103] Tehovnik, F., M. Doberšek, B. Arh, B. Koroušič, D. Kmetič and V. Dunat, Der Einfluss seltener Erden auf die Entstehung nichtmetallischer Einschlüsse und die Mikrostruktur von hochlegiertem Chromstahlguss, Metalurgija (2005), 44, 163–168.

[104] Park, J.S. and J.H. Park, Effect of Mg–Ti Deoxidation on the Formation Behavior of Equiaxed Crystals During Rapid Solidification of Iron Alloys, Steel research international 85 (2014).

[105] Wang, M.-l., G.-g. Cheng, S.-t. Qiu, P. Zhao and Y. Gan, Roles of titanium-rich precipitates as inoculants during solidification in low carbon steel, International Journal of Minerals, Metallurgy, and Materials 17 (2010), 3, 276–281.

[106] Kojola, N., S. Ekerot, M. Andersson and Jönsson, P. G., Pilot plant study of nozzle clogging mechanisms during casting of REM treated stainless steels, Ironmaking & Steelmaking 38 (2011), 1, 1–11.

[107] Li, Y., C. Liu, C. Li and M. Jiang, A Coupled Thermodynamic Model for Prediction of Inclusions Precipitation during Solidification of Heat-resistant Steel Containing Cerium, Journal of Iron and Steel Research, International 22 (2015), 6, 457–463.

[108] Schmid, F., Charakterisierung von nichtmetallischen Einschlüssen im System Fe-Ce-Al-O, Masterthesis, Leoben, 2017.

[109] Dorrer, P., S.K. Michelic, C. Bernhard, A. Penz and R. Rössler, Study on the Influence of FeTi-Addition on the Inclusion Population in Ti-Stabilized ULC Steels and its Consequences for SEN-Clogging, Steel research international 2019, 7.

[110] Giumelli, A.K., M. Militzer and E.B. Hawbolt, Analysis of the Austenite Grain Size Distribution in Plain Carbon Steels, ISIJ International 39 (1999), 3, 271–280.

[111] ASTM, Standard Methode zur Bestimmung der mittleren Korngröße bei Metallen(ASTM E 112), 2004, ftp://info.metallurgy.ac.at/M2CC%20NEU/ASTME_112.pdf.

[112] Fukumoto, S., High speed tool steel, material for blade edge, cutting tool, and manufacturing method of material for blade edge, Hitachi, Google Patents, 2014, http://www.google.com/patents/US20140079585.

[113] Clemex Intelligent microskopy, User Guide - Vision PE & Vision Lite 7.0.

[114] Michelic, S.K., G. Wieser and C. Bernhard, On the Representativeness of Automated SEM/EDS Analyses for Inclusion Characterisation with Special Regard to the Measured Sample Area, ISIJ International 51 (2011), 5, 769–775.

[115] Smirnov, L.A., V.A. Rovnushkin, A.S. Oryshchenko, G.Y. Kalinin and V.G. Milyuts, Modification of Steel and Alloys with Rare-Earth Elements. Part 1, Metallurgist 59 (2016), 11-12, 1053–1061.

[116] Kheirandish, S., Effect of Ti and Nb on the Formation of Carbides and the Mechanical Properties in As-cast AISI-M7 High-speed Steel, ISIJ International 41 (2001), 12, 1502–1509.

[117] Yang, Q.X., X.J. Ren, B. Liao, M. Yao and X. Wan, Discussion of RE inclusions as heterogeneous nuclei of primary austenite in hardfacing metals of medium-high carbon steels, Journal of Rare Earths 17 (1999), 4, 293–297.

# 9 Appendix

## 9.1 Planar Misfit Parameters

Table 9-1: Misfits at 20 °C for austenite [5,69,115–117]

| Compound | Lattice structure | Lattice parameter [nm] | Misfit @ 20 °C [%] | Density [gcm$^{-3}$] |
|---|---|---|---|---|
| $\gamma$-Fe | kfz | 0.3573 | | 7.3-7.4 (liq) |
| $AlCeO_3$ | tetragonal | 0.3767 | 5.00 | 6.62 |
| | | 0.3797 | 5.90 | |
| $CeO_2$ | kubisch F | 0.5411 | 6.70 | 7.20 |
| $Ce_2O_3$ | hexagonal $a_0$ | 0.3891 | 11.00 | 6.87 |
| $Ce_2O_2S$ | hexagonal $a_0$ | 0.4000 | 10.40 | 6.00 |
| CeS | kubisch F | 0.5778 | 6.60 | 5.98 |
| $Ce_2S_3$ | kubisch I | 0.8636 | 9.90 | 5.20 |
| BN | kubisch F | 0.3616 | 1.20 | 2.18 |
| NbC | kubisch F | 0.4467 | 4.10 | 7.82 |
| $ZrO_2$ | kubisch F (tetragonal) | | 0.96 | 6.00 |
| TiC | kubisch F | 0.4327 | 1.10 | 4.93 |
| TiN | kubisch F | 0.4242 | 3.10 | 5.21 |
| $TiO_2$, rutile | tetragonal | 0.4593 | 5.40 | 4.24 |
| | | 0.2592 | 2.50 | |
| $Ti_2O_3$ | hexagonal $a_0$ | 0.5139 | 1.70 | 4.49 |
| $Ti_3O_5$ | monoklin | 0.9970 | 1.30 | 4.24 |
| | | 0.5075 | 0.40 | |
| | | 0.7181 | 0.50 | |
| $TiMnO_3$ | trigonal | 0.5137 | 1.70 | 4.55 |
| | | 1.4283 | 0.10 | |
| MnS, **α**: T < 727 °C | kubisch F | 0.5224 | 3.40 | 4.00 |
| MnS, **β**: T > 727 °C | kubisch F | 0.5615 | 10.80 | 3.30 |
| MnO | kubisch | 0.4445 | 18.30 | 5.37 |
| MgS | kubisch F | 0.5200 | 2.90 | 2.68 |
| MgO | kubisch F | 0.4219 | 8.80 | 3.65 |
| $Al_2O_3$ | hexagonal $a_0$ | 0.4758 | 5.40 | 3.97 |
| $SiO_2$ | hexagonal $a_0$ | 0.4913 | 13.30 | 2.33 - 2.65 |
| MC | kfz | 0.4173 - 0.4433 | | 4.93 - 7.82 |

Table 9-2: Misfits at 20 °C for ferrite [5,69,115–117]

| Compound | Lattice structure | Lattice parameter [nm] | Misfit @ 20 °C [%] | Density [gcm$^{-3}$] |
|---|---|---|---|---|
| α-Fe | krz | 0.2867 | | 7.3-7.4 (liq) |
| AlCeO$_3$ | tetragonal | 0.3767 | 5.20 | 6.62 |
| | | 0.3797 | 5.50 | |
| CeO$_2$ | kubisch F | 0.5411 | 5.60 | 7.20 |
| Ce$_2$O$_3$ | hexagonal a$_0$ | 0.3891 | 4.00 | 6.87 |
| Ce$_2$O$_2$S | hexagonal a$_0$ | 0.4000 | 1.40 | 6.00 |
| CeS | kubisch F | 0.5778 | 0.80 | 5.98 |
| Ce$_2$S$_3$ | kubisch I | 0.8636 | 0.40 | 5.20 |
| BN | kubisch F | 0.3616 | 6.80 | 2.18 |
| NbC | kubisch F | 0.4467 | 8.70 | 7.82 |
| ZrO$_2$ | kubisch F (tetragonal) | | 7.00 | 6.00 |
| TiC | kubisch F | 0.4327 | 6.30 | 4.93 |
| TiN | kubisch F | 0.4242 | 4.60 | 5.21 |
| TiO$_2$, rutile | tetragonal | 0.4593 | 8.50 | 4.24 |
| | | 0.2592 | 9.60 | |
| Ti$_2$O$_3$ | hexagonal a$_0$ | 0.5139 | 3.90 | 4.49 |
| Ti$_3$O$_5$ | monoklin | 0.9970 | 5.00 | 4.24 |
| | | 0.5075 | 3.80 | |
| | | 0.7181 | 2.20 | |
| TiMnO$_3$ | trigonal | 0.5137 | 4.30 | 4.55 |
| | | 1.4283 | 0.40 | |
| MnS, α: T < 727 °C | kubisch F | 0.5224 | 4.90 | 4.00 |
| MnS, β: T > 727 °C | kubisch F | 0.5615 | 2.10 | 3.30 |
| MgS | kubisch F | 0.5200 | 4.80 | 2.68 |
| MgO | kubisch F | 0.4219 | 4.10 | 3.65 |
| Al$_2$O$_3$ | hexagonal a$_0$ | 0.4758 | 7.30 | 3.97 |
| β-SiO$_2$ | kfz | | 12.10 | 2.33 |
| MC | kfz | 0.4173 - 0.4433 | | 4.93 - 7.82 |

## 9.2  Classifications for Automated SEM Feature Measurements
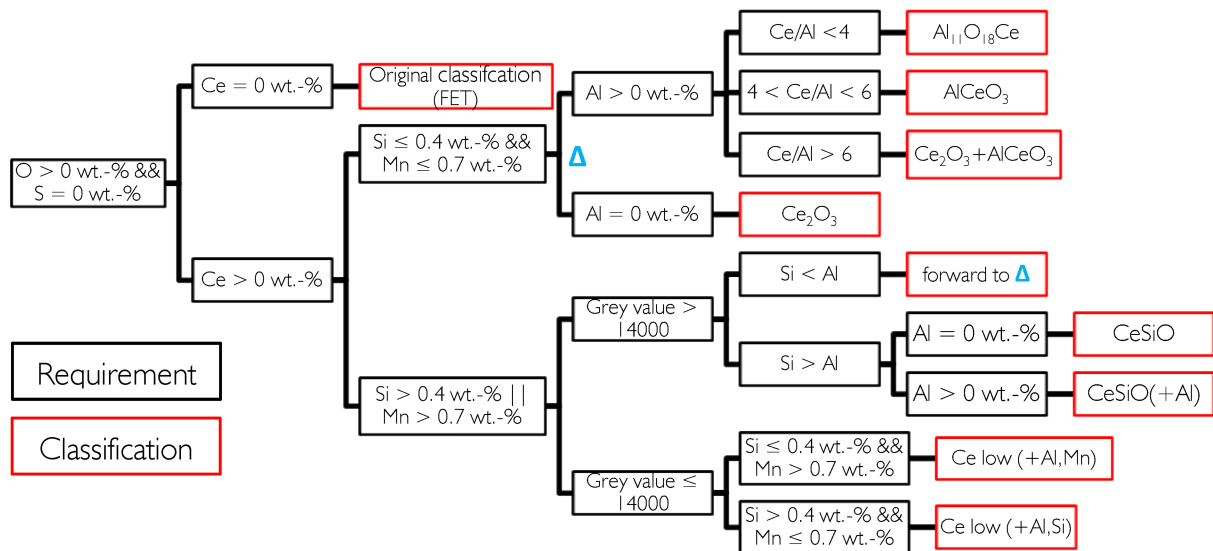


**Figure 9-1:** Particle classification of oxides for grain refinement experiments with SASS
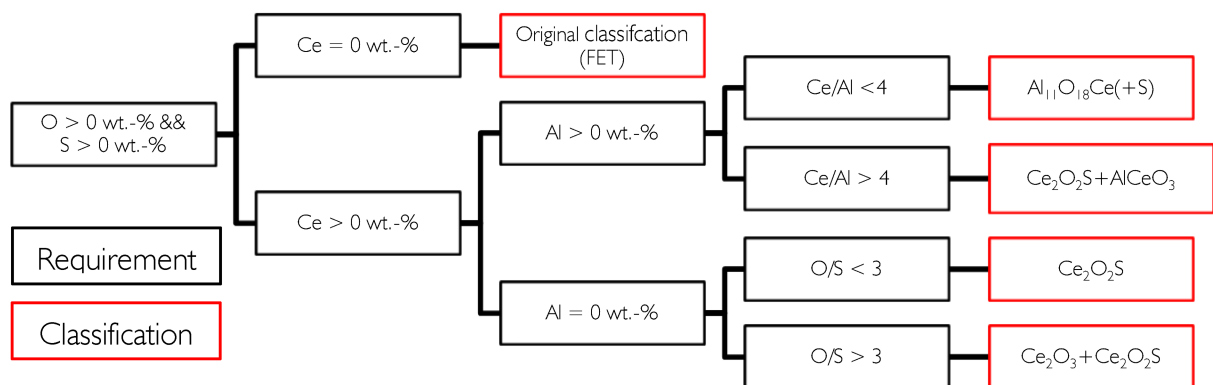


**Figure 9-2:** Particle classification of oxisulfides for inclusion formation and grain refinement experiments with SASS
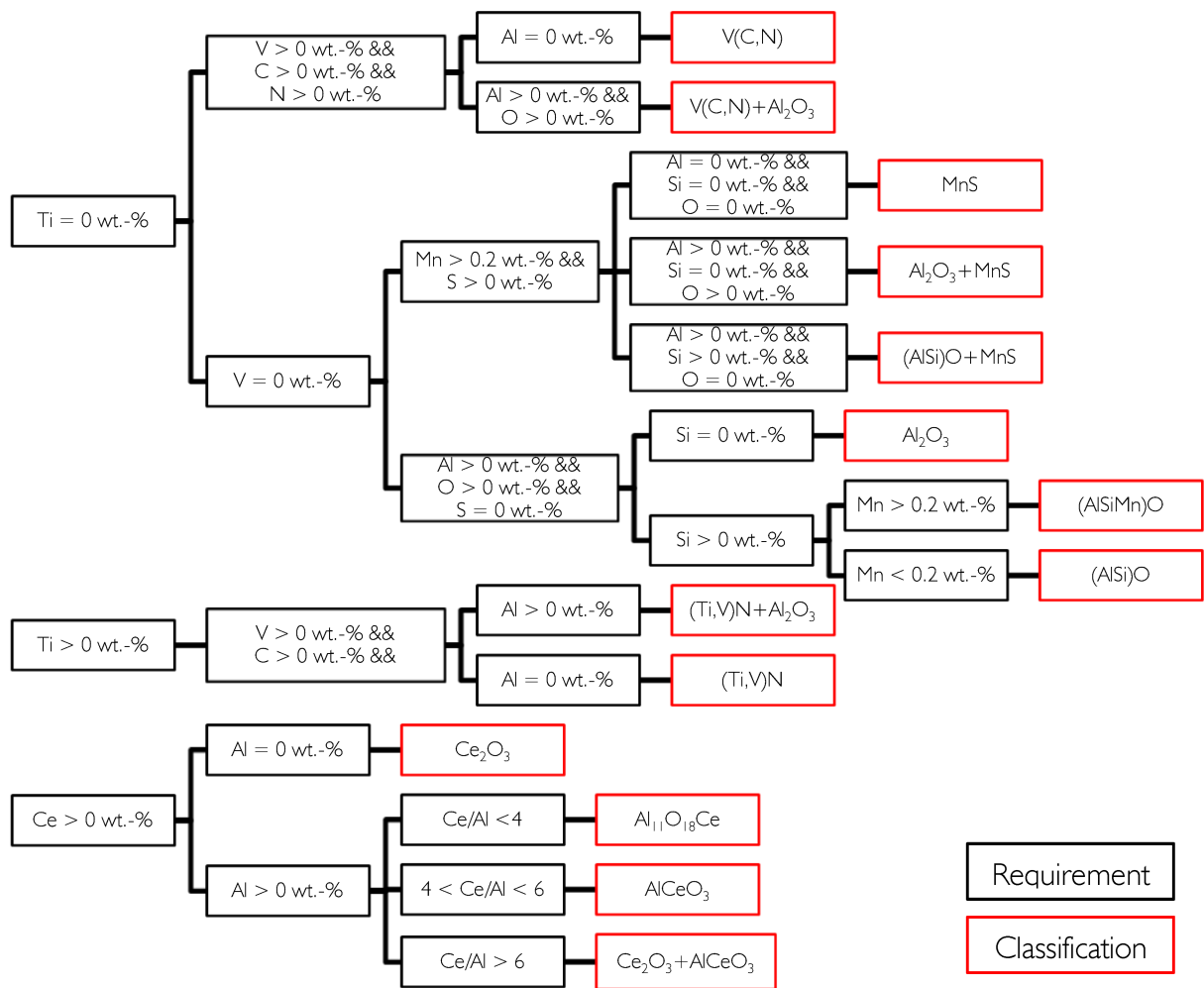
**Figure 9-3:** Particle classification for inoculation experiments with HSS

## 9.3 Chemical Analysis

Table 9-3: A965 Inoculation – Series A

|      | Ref     | A-E-1   | A-E-3   | A-E-4   | A-E-6   | A-Ce-2    | A-Ce-5  | A-Ce-7    |
|------|---------|---------|---------|---------|---------|-----------|---------|-----------|
| C    | 0.013   | 0.016   | 0.018   | 0.015   | 0.016   | 0.030     | 0.014   | 0.013     |
| Si   | 0.22    | 0.47    | 0.43    | 0.66    | 0.51    | 0.20      | 0.19    | 0.21      |
| Mn   | 0.49    | 0.53    | 0.56    | 0.55    | 0.54    | 0.66      | 0.49    | 0.53      |
| P    | 0.025   | 0.026   | 0.026   | 0.025   | 0.026   | 0.028     | 0.027   | 0.025     |
| S    | 0.0005  | 0.0005  | 0.0003  | 0.0004  | 0.0005  | <0.0003   | 0.0004  | < 0.0003  |
| Cr   | 19.27   | 19.98   | 19.56   | 20.1    | 20.01   | 19.84     | 19.68   | 19.72     |
| Mo   | 6.33    | 6.27    | 6.41    | 6.22    | 6.26    | 6.37      | 6.51    | 6.39      |
| Ni   | 18.14   | 17.66   | 17.96   | 17.52   | 17.65   | 18.07     | 18.09   | 18.20     |
| V    | 0.06    | 0.06    | 0.07    | 0.07    | 0.07    | 0.07      | 0.07    | 0.07      |
| W    | 0.08    | 0.08    | 0.08    | 0.08    | 0.08    | 0.08      | 0.08    | 0.08      |
| Cu   | 0.64    | 0.62    | 0.63    | 0.62    | 0.62    | 0.64      | 0.64    | 0.64      |
| Co   | 0.07    | 0.07    | 0.07    | 0.07    | 0.07    | 0.07      | 0.07    | 0.07      |
| Ti   | < 0.005 | < 0.005 | < 0.005 | <0.005  | < 0.005 | <0.005    | <0.005  | < 0.005   |
| Al   | < 0.005 | 0.006   | 0.007   | 0.009   | 0.006   | 0.013     | 0.014   | 0.024     |
| Nb   | 0.009   | 0.009   | 0.009   | 0.009   | 0.009   | 0.009     | 0.009   | 0.009     |
| B    | 0.0021  | 0.0022  | 0.0019  | 0.0022  | 0.0022  | 0.0021    | 0.0022  | 0.0020    |
| N    | 0.226   | 0.228   | 0.235   | 0.202   | 0.213   | 0.240     | 0.236   | 0.212     |
| O    | 0.016   | 0.014   | 0.013   | 0.011   | 0.014   | 0.0072    | 0.0078  | 0.0086    |
| As   | 0.006   | 0.007   | 0.007   | 0.006   | 0.006   | 0.006     | 0.006   | 0.006     |
| Sn   | < 0.005 | < 0.005 | < 0.005 | < 0.005 | < 0.005 | < 0.005   | < 0.005 | < 0.005   |
| Sb   | < 0.005 | < 0.005 | < 0.005 | < 0.005 | < 0.005 | < 0.005   | < 0.005 | < 0.005   |
| Zr   | < 0.005 | < 0.005 | < 0.005 | < 0.005 | < 0.005 | < 0.005   | < 0.005 | < 0.005   |
| Ce   |         | 0.032   | 0.021   | 0.073   | 0.019   | 0.031     | 0.0310  | 0.122     |

Table 9-4: A965 Inoculation – Series B

|      | Ref | B-E-3 | B-Ce-1 | B-Ce-2 | B-Ce-4 | B-Ce-5 |
|------|-----|-------|--------|--------|--------|--------|
| C    | 0.013 | 0.017 | 0.013 | 0.014 | 0.017 | 0.026 |
| Si   | 0.22 | 0.46 | 0.22 | 0.20 | 0.19 | 0.20 |
| Mn   | 0.49 | 0.58 | 0.61 | 0.54 | 0.63 | 0.69 |
| P    | 0.025 | 0.023 | 0.026 | 0.025 | 0.025 | 0.025 |
| S    | 0.0005 | 0.0003 | 0.0003 | 0.0004 | 0.0004 | 0.0003 |
| Cr   | 19.27 | 19.62 | 19.43 | 19.63 | 19.61 | 19.69 |
| Mo   | 6.33 | 6.39 | 6.52 | 6.53 | 6.42 | 6.42 |
| Ni   | 18.14 | 17.93 | 18.00 | 18.11 | 18.15 | 18.06 |
| V    | 0.06 | 0.07 | 0.07 | 0.07 | 0.07 | 0.07 |
| W    | 0.08 | 0.08 | 0.08 | 0.08 | 0.08 | 0.08 |
| Cu   | 0.64 | 0.63 | 0.64 | 0.64 | 0.64 | 0.63 |
| Co   | 0.07 | 0.06 | 0.07 | 0.07 | 0.07 | 0.07 |
| Ti   | < 0.005 | < 0.005 | < 0.005 | < 0.005 | < 0.005 | < 0.005 |
| Al   | < 0.005 | 0.019 | 0.013 | 0.018 | 0.022 | 0.012 |
| Nb   | 0.009 | 0.008 | 0.011 | 0.009 | 0.009 | 0.009 |
| B    | 0.0021 | 0.0019 | 0.0019 | 0.0019 | 0.0019 | 0.0019 |
| N    | 0.226 | 0.219 | 0.200 | 0.206 | 0.211 | 0.214 |
| O    | 0.016 | 0.012 | 0.013 | 0.013 | 0.017 | 0.015 |
| As   | 0.006 | 0.006 | 0.006 | 0.006 | 0.006 | 0.007 |
| Sn   | < 0.005 | < 0.005 | < 0.005 | < 0.005 | < 0.005 | < 0.005 |
| Sb   | < 0.005 | < 0.005 | < 0.005 | < 0.005 | < 0.005 | < 0.005 |
| Zr   | < 0.005 | < 0.005 | < 0.005 | < 0.005 | < 0.005 | < 0.005 |
| Ce   |      | 0.009 | 0.018 | 0.020 | 0.108 | 0.035 |

Table 9-5: S500 TO

| | 1 Kmin-1 | 5Kmin-1 | 15Kmin-1 |
|---|---|---|---|
| C | 1.05 | 1.09 | 1.12 |
| Si | 0.52 | 0.5 | 0.5 |
| Mn | 0.18 | 0.17 | 0.17 |
| P | 0.023 | 0.032 | 0.028 |
| S | 0.0006 | 0.0006 | 0.0006 |
| Cr | 3.69 | 3.71 | 3.69 |
| Mo | 8.57 | 9 | 8.94 |
| Ni | 0.38 | 0.38 | 0.38 |
| V | 0.82 | 0.86 | 0.86 |
| W | 1.43 | 1.51 | 1.47 |
| Cu | 0.09 | 0.09 | 0.09 |
| Co | 7.57 | 7.55 | 7.56 |
| Ti | < 0.005 | < 0.005 | < 0.005 |
| Al | 0.01 | 0.009 | 0.009 |
| Nb | 0.009 | 0.01 | 0.01 |
| B | < 0.0005 | < 0.0005 | < 0.0005 |
| N | | 0.015 | |
| O | | 0.0016 | |
| As | < 0.005 | < 0.005 | < 0.005 |
| Sn | < 0.005 | < 0.005 | < 0.005 |
| Sb | < 0.005 | < 0.005 | < 0.005 |
| Ce | | | |

Table 9-6: S500 Casting Temperature + Inoculation

| | CT 1500 | CT 1550 | CT 1600 | CT 1650 | Ref | Al-Ref | CeAl | Titanium |
|---|---|---|---|---|---|---|---|---|
| C | 1.02 | 1.06 | 1.06 | 1.04 | 1.03 | 0.95 | 1.04 | 1.00 |
| Si | 0.43 | 0.46 | 0.46 | 0.43 | 0.41 | 0.49 | 0.49 | 0.48 |
| Mn | 0.21 | 0.2 | 0.2 | 0.19 | 0.26 | 0.25 | 0.20 | 0.22 |
| P | 0.026 | 0.027 | 0.03 | 0.022 | 0.022 | 0.027 | 0.030 | 0.026 |
| S | 0.0005 | 0.0005 | 0.0004 | 0.0007 | 0.0005 | 0.0018 | 0.0009 | 0.0012 |
| Cr | 3.67 | 3.69 | 3.69 | 3.71 | 3.83 | 3.79 | 3.68 | 3.66 |
| Mo | 9.35 | 9.39 | 9.39 | 9.02 | 9.08 | 9.04 | 9.30 | 8.98 |
| Ni | 0.34 | 0.35 | 0.34 | 0.37 | 0.35 | 0.41 | 0.35 | 0.38 |
| V | 1.03 | 1.01 | 1.02 | 0.88 | 0.99 | 1.18 | 1.01 | 1.01 |
| W | 1.28 | 1.32 | 1.32 | 1.43 | 1.36 | 1.38 | 1.31 | 1.37 |
| Cu | 0.19 | 0.18 | 0.18 | 0.09 | 0.1 | 0.12 | 0.18 | 0.13 |
| Co | 7.81 | 7.78 | 7.81 | 7.61 | 7.62 | 7.50 | 7.73 | 7.80 |
| Ti | 0.005 | < 0.005 | < 0.005 | < 0.005 | <0.005 | <0.005 | <0.005 | 0.015 |
| Al | 0.005 | < 0.005 | 0.038 | 0.035 | 0.008 | 0.017 | 0.020 | 0.018 |
| Nb | 0.005 | 0.006 | 0.005 | 0.011 | <0.005 | 0.008 | <0.005 | 0.008 |
| B | 0.0005 | <0.0005 | <0.0005 | <0.0005 | <0.0005 | <0.0005 | <0.0005 | <0.0005 |
| N | 0.018 | 0.027 | 0.025 | 0.035 | 0.035 | 0.042 | 0.040 | 0.040 |
| O | 0.003 | 0.0034 | 0.0052 | 0.0054 | 0.0072 | 0.0067 | 0.0084 | 0.0051 |
| As | 0.006 | 0.006 | 0.006 | < 0.005 | 0.008 | <0.005 | 0.005 | 0.005 |
| Sn | 0.005 | < 0.005 | < 0.005 | < 0.005 | < 0.005 | <0.005 | <0.005 | <0.005 |
| Sb | 0.005 | < 0.005 | < 0.005 | < 0.005 | < 0.005 | <0.005 | <0.005 | <0.005 |
| Ce | | | | | | - | 0.025 | - |

## 9.4 Particle populations in inclusion formation experiments with SASS
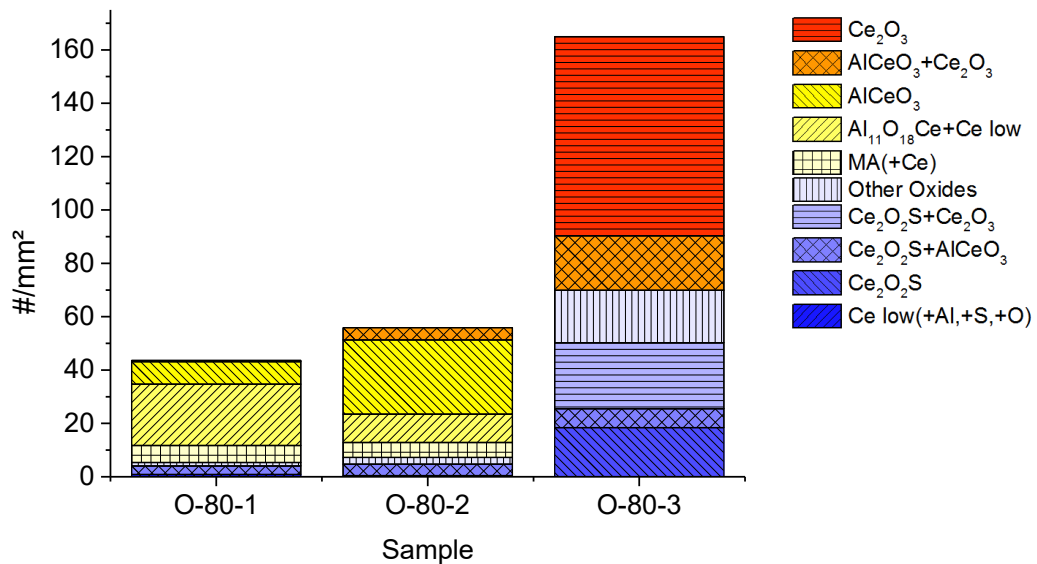


**Figure 9-4:** Inclusion population with a total oxygen content of 80 ppm
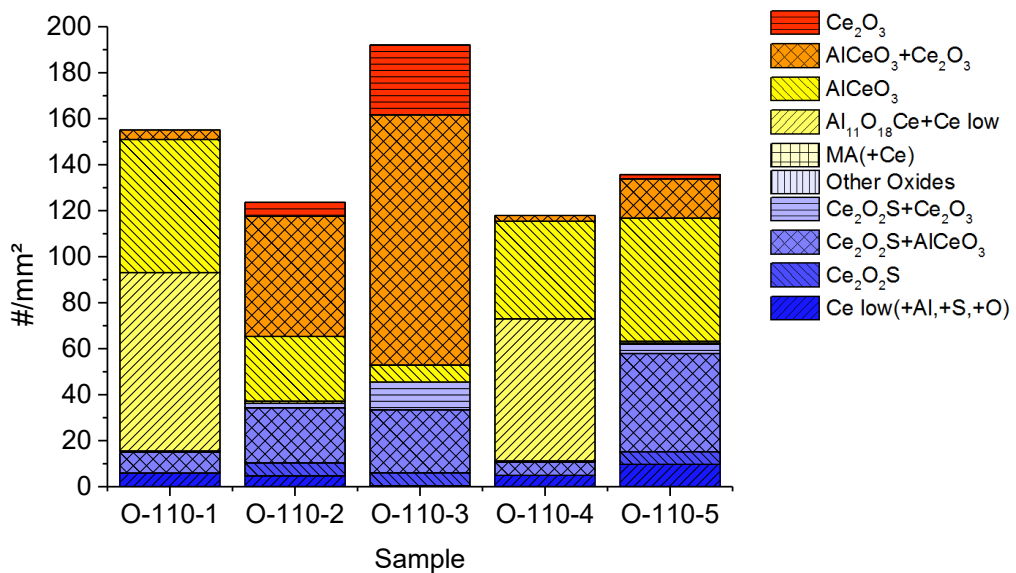


**Figure 9-5:** Inclusion population with a total oxygen content of 110 ppm

## 9.5  Documentation – Grain Refinement Experiments with SASS

### 9.5.1  Reference ingot

Table 9-7: Structural parameters and inclusion population of Ref

| | Unit | Ref |
|---|---|---|
| Grain size $d_A$ | [mm] | 8.60 |
| Area fraction equiaxed | [1] | 0.226 |
| Nbr. Grains | [1/cm²] | 1.66 |
| Nbr. Inclusions | [1/mm²] | 147 |
| Nbr. AlCeO$_3$ | [1/mm²] | |
| Cer$_{sol.}$ | [ppm] | |
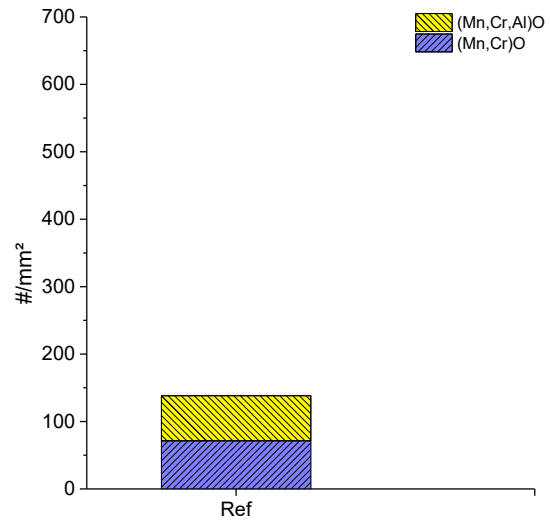
## 9.5.2 Test Series A – Casting Temperature 1470 °C

Table 9-8: Structural parameters and inclusion population of A-E-1

| | Unit | A-E-1 |
|---|---|---|
| Grain size $d_A$ | [mm] | 1.71 |
| Area fraction equiaxed | [1] | 0.640 |
| Nbr. Grains | [1/cm²] | 41.25 |
| Nbr. Inclusions | [1/mm²] | 320 |
| Nbr. AlCeO$_3$ | [1/mm²] | 35.92 |
| Cer$_{sol.}$ | [ppm] | 0.552 |
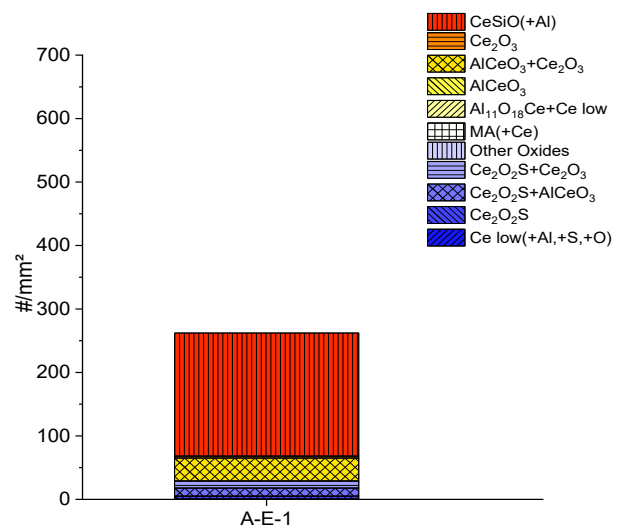
Table 9-9: Structural parameters and inclusion population of A-Ce-2

| | Unit | A-Ce-2 |
|---|---|---|
| Grain size $d_A$ | [mm] | 2.39 |
| Area fraction equiaxed | [1] | 0.742 |
| Nbr. Grains | [1/cm²] | 25.23 |
| Nbr. Inclusions | [1/mm²] | 257 |
| Nbr. AlCeO$_3$ | [1/mm²] | 108.57 |
| Cer$_{sol.}$ | [ppm] | 31 |



Legend:
- CeSiO(+Al)
- Ce$_2$O$_3$
- AlCeO$_3$+Ce$_2$O$_3$
- AlCeO$_3$
- Al$_{11}$O$_{18}$Ce+Ce low
- MA(+Ce)
- Other Oxides
- Ce$_2$O$_2$S+Ce$_2$O$_3$
- Ce$_2$O$_2$S+AlCeO$_3$
- Ce$_2$O$_2$S
- Ce low(+Al,+S,+O)
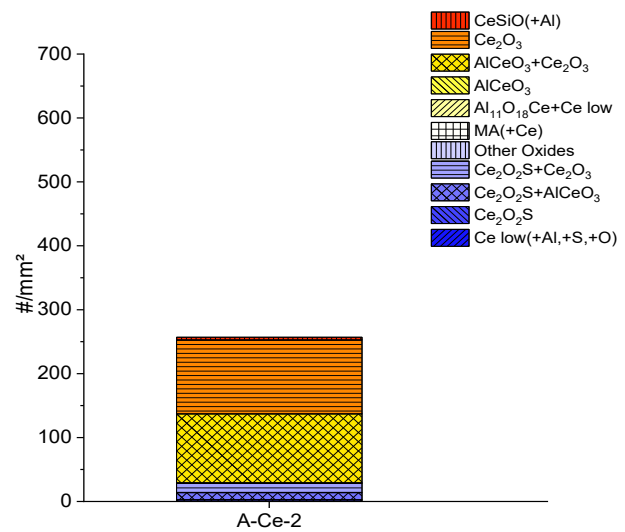
Table 9-10: Structural parameters and inclusion population of A-E-3

| | Unit | A-E-3 |
|---|---|---|
| Grain size $d_A$ | [mm] | 2.21 |
| Area fraction equiaxed | [1] | 0.574 |
| Nbr. Grains | [1/cm²] | 21.12 |
| Nbr. Inclusions | [1/mm²] | 207 |
| Nbr. AlCeO$_3$ | [1/mm²] | 44.42 |
| Cer$_{sol.}$ | [ppm] | 0.0282 |
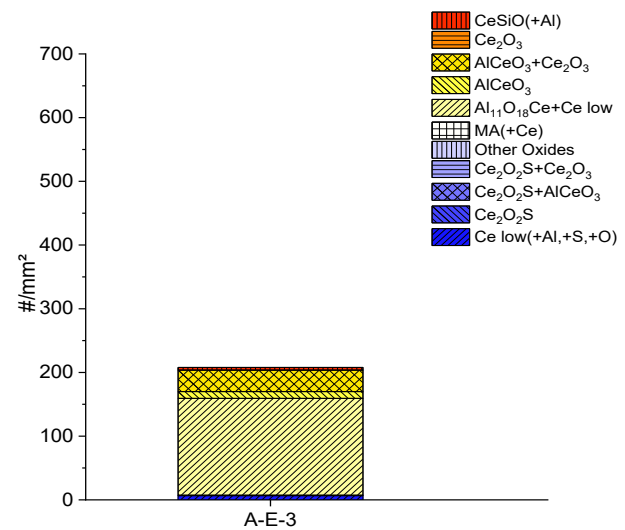
Table 9-11: Structural parameters and inclusion population of A-E-4

| | Unit | A-E-4 |
|---|---|---|
| Grain size $d_A$ | [mm] | 3.86 |
| Area fraction equiaxed | [1] | 0.539 |
| Nbr. Grains | [1/cm²] | 8.25 |
| Nbr. Inclusions | [1/mm²] | 188 |
| Nbr. AlCeO$_3$ | [1/mm²] | 126.2 |
| Cer$_{sol.}$ | [ppm] | 93.8 |

Legend:
- CeSiO(+Al)
- Ce$_2$O$_3$
- AlCeO$_3$+Ce$_2$O$_3$
- AlCeO$_3$
- Al$_{11}$O$_{18}$Ce+Ce low
- MA(+Ce)
- Other Oxides
- Ce$_2$O$_2$S+Ce$_2$O$_3$
- Ce$_2$O$_2$S+AlCeO$_3$
- Ce$_2$O$_2$S
- Ce low(+Al,+S,+O)
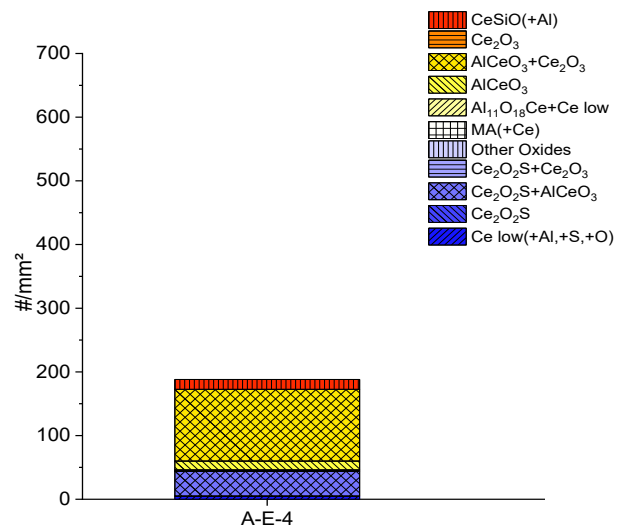
**Table 9-12:** Structural parameters and inclusion population of A-Ce-5

| | Unit | A-Ce-5 |
|---|---|---|
| Grain size $d_A$ | [mm] | 4.48 |
| Area fraction equiaxed | [1] | 0.572 |
| Nbr. Grains | [1/cm²] | 6.12 |
| Nbr. Inclusions | [1/mm²] | 334 |
| Nbr. AlCeO$_3$ | [1/mm²] | 151.54 |
| Cer$_{sol.}$ | [ppm] | 33 |
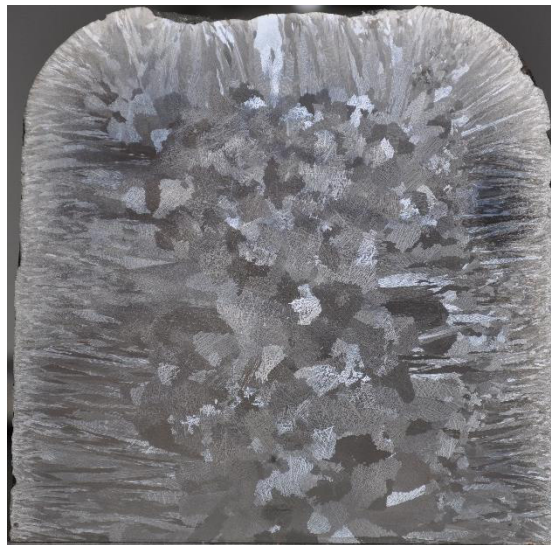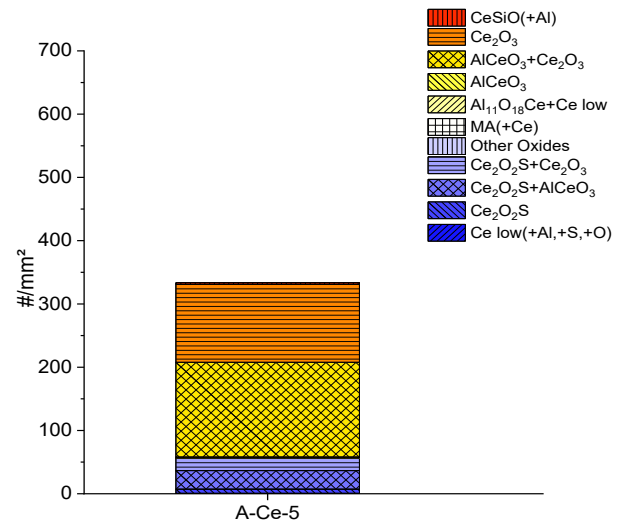
Table 9-13: Structural parameters and inclusion population of A-E-6

|  | Unit | A-E-6 |
|---|---|---|
| Grain size $d_A$ | [mm] | 6.39 |
| Area fraction equiaxed | [1] | 0.399 |
| Nbr. Grains | [1/cm²] | 3.01 |
| Nbr. Inclusions | [1/mm²] | 340 |
| Nbr. AlCeO$_3$ | [1/mm²] | 5.60 |
| Cer$_{sol.}$ | [ppm] | 0.028 |
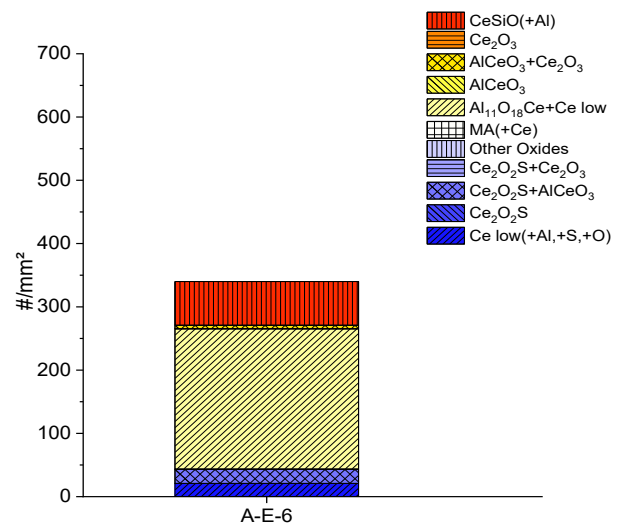
Table 9-14: Structural parameters and inclusion population of A-Ce-7

| | Unit | A-Ce-7 |
|---|---|---|
| Grain size $d_A$ | [mm] | 9.83 |
| Area fraction equiaxed | [1] | 0.197 |
| Nbr. Grains | [1/cm²] | 1.27 |
| Nbr. Inclusions | [1/mm²] | 670 |
| Nbr. AlCeO₃ | [1/mm²] | 0 |
| $Cer_{sol.}$ | [ppm] | 729 |
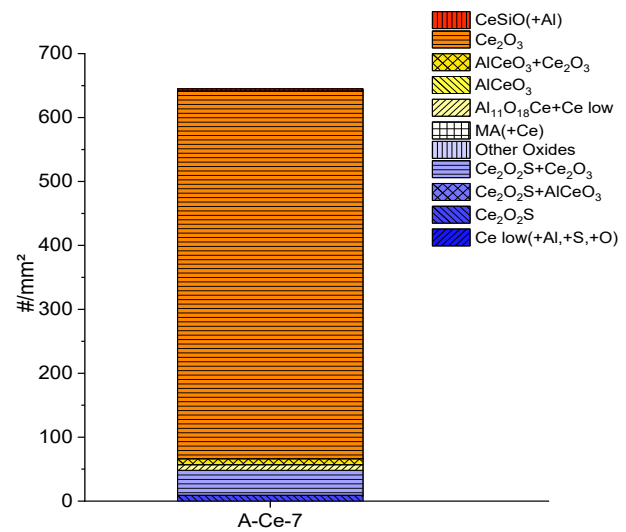
## 9.5.3 Test Series B – Casting Temperature 1540 °C

Table 9-15: Structural parameters and inclusion population of B-Ce-1

| | Unit | B-Ce-1 |
|---|---|---|
| Grain size $d_A$ | [mm] | 6.20 |
| Area fraction equiaxed | [1] | 0.462 |
| Nbr. Grains | [1/cm²] | 3.19 |
| Nbr. Inclusions | [1/mm²] | 185 |
| Nbr. AlCeO$_3$ | [1/mm²] | 8.64 |
| Cer$_{sol.}$ | [ppm] | 0.076 |
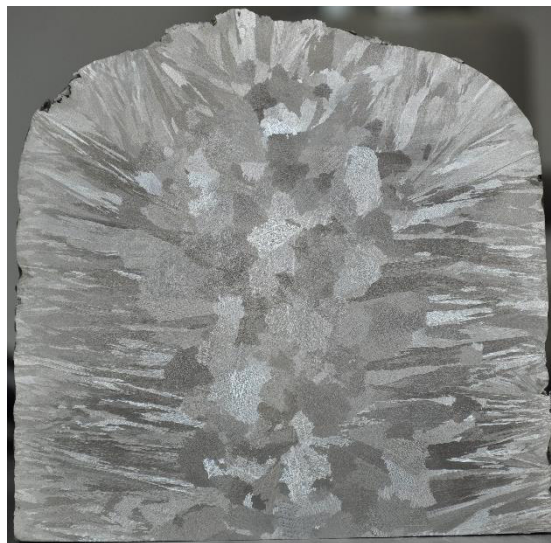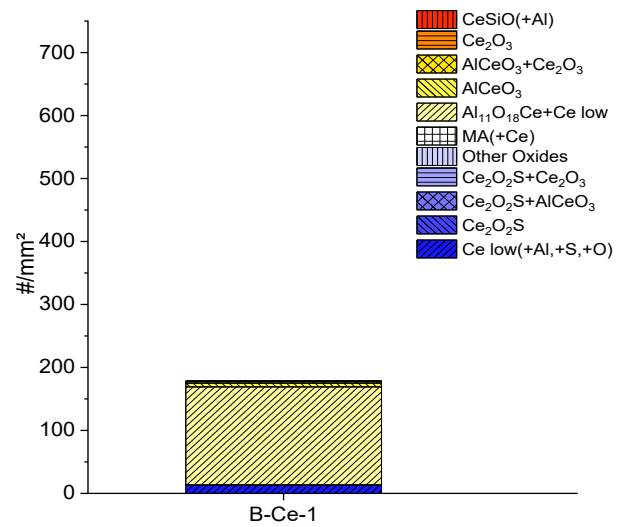
Table 9-16: Structural parameters and inclusion population of B-Ce-2

| | Unit | B-Ce-2 |
|---|---|---|
| Grain size $d_A$ | [mm] | 7.02 |
| Area fraction equiaxed | [1] | 0.341 |
| Nbr. Grains | [1/cm²] | 2.49 |
| Nbr. Inclusions | [1/mm²] | 198 |
| Nbr. AlCeO$_3$ | [1/mm²] | 13.35 |
| Cer$_{sol.}$ | [ppm] | 0.134 |
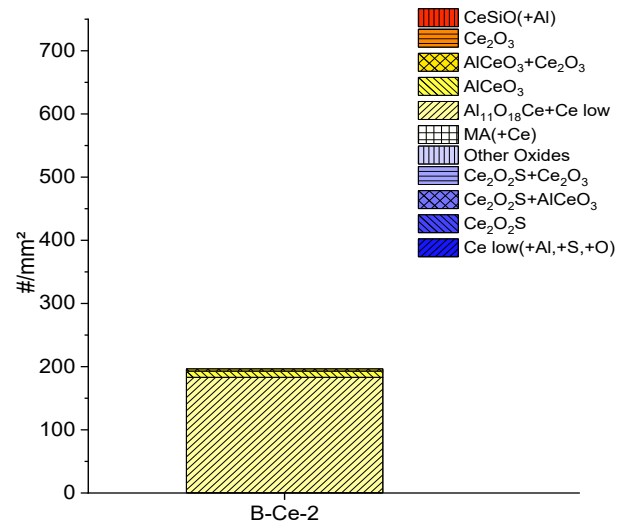
Table 9-17: Structural parameters and inclusion population of B-E-3

| | Unit | B-E-3 |
|---|---|---|
| Grain size $d_A$ | [mm] | 8.46 |
| Area fraction equiaxed | [1] | 0.306 |
| Nbr. Grains | [1/cm²] | 1.72 |
| Nbr. Inclusions | [1/mm²] | 165 |
| Nbr. AlCeO$_3$ | [1/mm²] | 6.09 |
| Cer$_{sol.}$ | [ppm] | 0.138 |
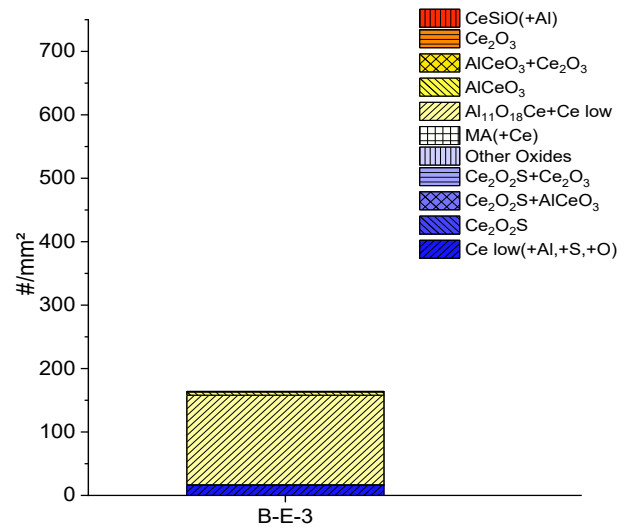
Table 9-18: Structural parameters and inclusion population of B-Ce-4

| | Unit | B-Ce-4 |
|---|---|---|
| Grain size $d_A$ | [mm] | 7.71 |
| Area fraction equiaxed | [1] | 0.218 |
| Nbr. Grains | [1/cm²] | 2.06 |
| Nbr. Inclusions | [1/mm²] | 172 |
| Nbr. AlCeO$_3$ | [1/mm²] | 87.80 |
| Cer$_{sol.}$ | [ppm] | 0.075 |
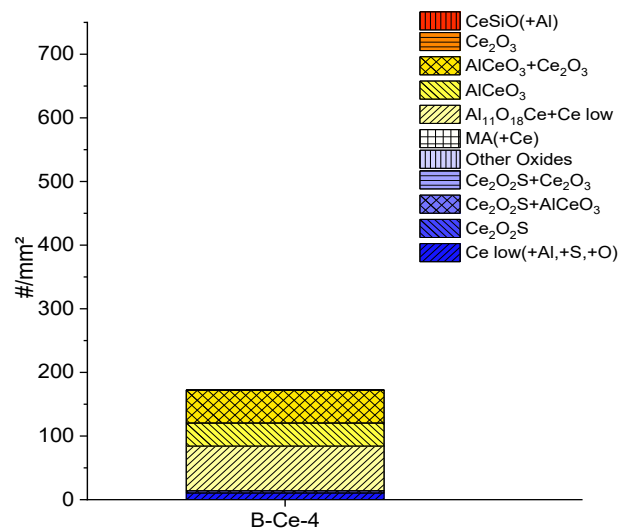
Table 9-19: Structural parameters and inclusion population of B-Ce-5

|  | Unit | B-Ce-5 |
|---|---|---|
| Grain size $d_A$ | [mm] | 6.24 |
| Area fraction equiaxed | [1] | 0.159 |
| Nbr. Grains | [1/cm²] | 3.15 |
| Nbr. Inclusions | [1/mm²] | 700 |
| Nbr. AlCeO$_3$ | [1/mm²] | 0 |
| Cer$_{sol.}$ | [ppm] | 94 |

# List of Figures

# List of Tables